2002

Magnetic modelling and sensorless control of the synchronous reluctance machine

Philip Paul Ciufo
University of Wollongong

Magnetic Modelling and Sensorless Control of the Synchronous Reluctance Machine

A thesis submitted in fulfilment of the requirements for the award of the degree of

Doctor of Philosophy

from

University of Wollongong

by

Philip Paul Ciufo

Bachelor of Engineering (*Hons.*)

Master of Engineering (*Hons.*)

School of Electrical, Computer and Telecommunications Engineering

April 2002

Statement of Originality

I, Philip Paul Ciufo, declare that this thesis, submitted in fulfilment of the requirements for the award of Doctor of Philosophy, in the School of Electrical, Computer and Telecommunications Engineering, University of Wollongong, is wholly my own work unless otherwise referenced or acknowledged. The document has not been submitted for qualifications at any other academic institution.

Signed

Philip Paul Ciufo

Acknowledgments

There are many people who have helped me along the road to the completion of this PhD and I would like to thank them. Above all, I'd like to thank my wife Marilyn and my two girls, Emma and Sophie. Their patience with the many hours I have spent working on this thesis and its experimental work has been outstanding. Without their support and encouragement, I would not have been able to achieve what I have.

I would like to thank my supervisor, Dr. Don Platt. A more patient person, I have yet to meet. We have spent many hours discussing the work presented in this thesis and his technical guidance and abilities have been invaluable. Associate Professor Vic Gosbell has always been available to answer my questions whenever Don was unavailable. My gratitude goes to Vic also.

I would also like to mention the workshop staff of the School of Electrical, Computer and Telecommunications Engineering who have made the experimental work possible. Their assistance in assembling a great variety of small circuit boards was a pivotal task in being able to customise the commercial hardware used in the project. Providing help in the mechanical design and fabrication of some of the hardware must also be noted.

Finally, I'd like to thank my parents who have always encouraged me to complete this PhD, even though it seemed that it would never end.

Contents

List of Figures

List of Tables

Abstract

This thesis is essentially divided into three major sections. The first section involves the development of a model of the Synchronous Reluctance Machine (SyncRM) that enables the estimation of fluxes and flux densities in various parts of the motor. The technique develops a model that recognises the zigzag nature of the rotor flux. The results obtained from the analytical modelling are compared to those obtained from a finite element analysis of the same machine.

The second section develops a new sensorless position estimation algorithm. It is based on a parameter independent statistical method. The technique makes use of the observation that the current changes are statistically more likely to be higher in the q-axis rather than the d-axis of the SyncRM. The parameter independence is demonstrated by a detailed simulation which uses a design that has a very low saliency and is still able to produce quality results. The principle is proven using the detailed simulation. The algorithm is extended to produce a speed estimation signal by the use of a modified zero crossing algorithm.

The third section of the thesis involves verification of the sensorless algorithms developed. A 22-kW, 6 pole, axially laminated SyncRM and an inverter system is used to verify the new sensorless techniques. Extensive experimental results are presented that confirm the excellent performance of the algorithms.

Chapter 1

Introduction

This thesis is concerned with two aspects of the Synchronous Reluctance Motor; the q-axis magnetic circuit modelling and the sensorless rotor position estimation. The modelling aspect of the research looks at the effect that the axially laminated rotor has on the distribution of flux. It seeks to find analytical equations that can predict reluctance and flux in various parts of the motor. The sensorless algorithm has the aim of recognising the rotor position based on line measurements of machine current.

The Synchronous Reluctance Motor (SyncRM) has been with us for many years. It has been the subject of many papers in a variety of learned publications since the early 1920's (Kostko, 1923). In recent times, there has been a renewed interest in the use of the motor for industrial applications (Lipo, 1991), (Fratta et al., 1992). Reasons for this include the development of power electronics and the relatively new designs of the axially laminated rotor (Cruickshank et al., 1966), (Platt, 1992) and (Staton et al., 1993).

The SyncRM is an excellent machine for both constant and variable speed applications. However, before the SyncRM can make inroads into the application share that the Induction Motor currently has, much more work needs to be done.

In essence, the stator of the SyncRM is identical with that of an induction machine. A rotating magnetic field is produced by a multi-phase set of stator currents in the windings and is generally sinusoidally distributed. The rotor is shaped such that a small airgap exists in the direct (d) axis and a large gap in the quadrature (q) axis. During synchronous operation, the peak of the stator flux wave is aligned with the d-axis of the machine (if the q-axis flux is 0).

As technology has progressed and power electronics become cheaper, the desire for variable speed AC drive systems has increased. The SyncRM has not escaped this requirement and there is much renewed interest in the SyncRM. The main reasons for this new research are:

1. New design methodologies mean higher saliency ratios are possible for the SyncRM. This makes the motor more competitive with the ubiquitous induction machine, particularly in terms of power factor and kVA requirement.

2. The available torque for a given frame size appears to be higher for a SyncRM than for an induction machine (Miller et al., 1991).

3. The inherent saliency of the SyncRM means that it is possible to develop a robust sensorless rotor position detection scheme.

4. The SyncRM's rotor does not require copper or aluminium windings. It generally has a simple design and runs at lower temperatures at full load and low speed.

5. An inexpensive rotor structure that makes the SyncRM economically viable.

6. It is easier to control than the induction machine as there is no slip.

7. The field-weakening performance is comparable to that of the induction machine (Fratta et al., 1992).

The issue of q-axis modelling and sensorless rotor position estimation will be addressed in later chapters. This chapter provides a basic outline of the history of the SyncRM. Several different types of SyncRM's are presented with a short discussion of the relative advantages and disadvantages of the particular design. This information is provided in the first section.

The second section presents the motivation behind the research. The reasoning behind understanding the q-axis flux distribution and how it may affect machine design is presented. Included is a discussion on the desire to have sensorless rotor position estimation.

Finally, the third section of this chapter delivers a summary of the contributions of this thesis and an outline of its structure.

1.1 Machine History

The stator of the Synchronous Reluctance Motor has is similar to that of the induction motor. The rotor design, however, is considerably different. In the case of the SyncRM, the rotor is designed to have inductances that are different along its d- and q-axis. Much of the research performed over the years has been associated with this design process. Figure 1.1 illustrates the rotors of several machine types (Staton et al., 1993).

The electromagnetic torque is developed because the rotor will always attempt to find a position that offers the stator flux the path of minimum reluctance. This occurs when the rotor's low reluctance rotor axis, the d-axis, becomes aligned with the stator field axis.

The key design parameter of the SyncRM is the Saliency or Synchronous Inductance Ratio. This is defined by the ratio of the d-axis inductance to the q-axis inductance, L_d/L_q. Consequently, the idea behind most rotor designs is to maximise the value of this ratio. A high value of L_d is achieved by providing guides for the d-axis flux and a low value of L_q can be achieved by inserting

barriers to the q-axis flux.

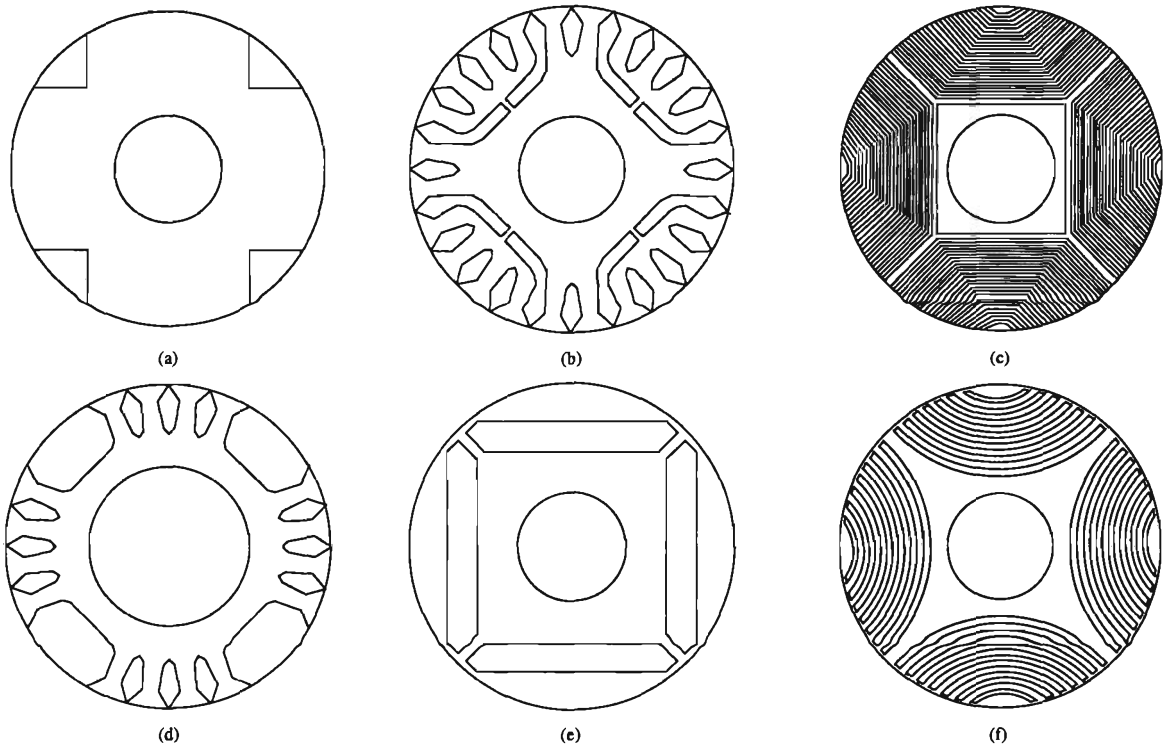

Figure 1.1: Various 4 Pole Rotor Designs: (a) & (d) Salient Pole Rotors (b) & (e) Single Barrier Rotors (c) Multiple Barrier Rotor (f) Axially Laminated Rotors (Staton et al., 1993)

The simplest rotor is that of the salient pole construction, illustrated in Figure 1.1(a) & (d). They are made either of axially stacked laminations or solid steel. This type of design suffers from a low saliency ratio and poor relative performance. However, the simplicity and low cost seem to outweigh some of these limitations.

The development of the more specialised styles of rotor has perhaps take on two distinct flavours; the segmented rotor (Figure 1.1(b) & (e)) and the multiple barrier rotor (Figure 1.1(c) & (f)). Of all the rotor types, the salient pole design is one of the oldest, however, a segmented q-axis flux barrier design was being investigated by Kostko (Kostko, 1923) in 1923. He proposed a q-axis flux barrier based rotor design that had a potentially higher saliency ratio by reducing L_q while keeping L_d unchanged. It is pointed out that the essential limitation of the salient pole design was that increasing the size of the inter-

polar cutout to reduce L_q narrowed the pole arc and consequently produced an unwanted reduction in L_d. He quotes unsaturated saliency ratios of 25.6 could be achieved for a rotor with "four segments".

The other flavour of rotor type was intensively developed by Lawrenson and Agu (Lawrenson and Agu, 1964b), (Lawrenson and Agu, 1964a). The performance of these machines were shown to be better than equivalent conventional designs because of a larger saliency ratio. However, the rotor construction was expensive due to its complicated nature. Double barrier designs such as that illustrated by Figure 1.1(b) surfaced in the 1970's largely due to the work by Honsinger (Honsinger, 1971a), (Honsinger, 1971b). The designs had two barriers per pole and were fitted with a starting cage. The motors were driven by inverters with V/f controllers.

The axially laminated designs were all an attempt to reduce L_q without reducing L_d. Kostko (Kostko, 1923) recognised that the effects of slot leakage could be decreased by having a large number of thin barriers. In more recent work by the author, this design methodology is not entirely appropriate since by having a large number of such laminations can in fact lead to an increase in q-axis inductance (Ciufo et al., 1994). Kostko also implied the the anisotropy of the magnetic material was important because of the possible improvement of L_d.

The axially laminated rotor was made from grain oriented steel laminations and it implements this idea. The first rotor of this type with a squirrel cage stator was built by Cruickshank and Menzies in 1966 (Cruickshank et al., 1966). The machine was further developed but the machine's potential could not be realised in terms of the possible saliency ratio due to the presence of the starting cage. Consequently, interested waned in this style of rotor until the late 1980's when the modern cageless machine was developed (Staton et al., 1993), (Matsuo and Lipo, 1994a), (Boldea and Nasar, 1991), (Platt, 1992) and (Soong et al., 1995).

The axially laminated structure achieves the highest values of saliency of all the reluctance machines. The large number of flux barriers perpendicular to the q-axis flux and the anisotropic flux guides in the d-axis lead to increased reductions in the value of L_q and an increase in the value of L_d. This is contrary to other designs, where reductions in q-axis inductance also affected the value of the d-axis inductance in a detrimental fashion.

When compared to the induction machine with the same frame, the vector controlled axially laminated machine has comparable or better performance. The parameters torque, output power and efficiency are available with a better power factor and lower kVA rating for the supply inverter.

1.2 Research Motivation

The thrust of the work performed for this thesis is twofold; a better understanding of the nature of the q-axis magnetic circuit and a new method for the sensorless rotor position detection.

1.2.1 Magnetic Circuit Modelling

There has always been interest in the magnetic circuit modelling of the SyncRM. Much of this modelling involves determination of torque and motor fluxes using the physical parameters of the motor such as slot width and depth (Marongiu and Vagati, 1991; Boldea et al., 1994; Luo et al., 1994; Fratta et al., 1993; Ciufo et al., 1994). Other modelling attempts have been made utilising motor parameters such as d-axis inductance and q-axis inductance, but without referring to the process of determining such quantities (Staton et al., 1995; Uezato et al., 1994). A third level of modelling has been the optimisation of rotor design to produce better or more predictable torque characteristics (Staton et al., 1993; Matsuo and Lipo, 1994a; Platt, 1992; Fletcher et al., 1994). Perhaps the last level of activity is in the design of the stator windings to improve motor per-

formance or control (Law et al., 1994). These levels of modelling are important since they provide an insight into the dependencies of the motor characteristics on the physical design of the motor.

For any particular motor with a given rotor position, it is possible to construct a magnetic circuit which describes it with a reasonable degree of accuracy. We would simply assume that all the sections of iron were magnetic short circuits (nodes) and that the airgaps separating these pieces of iron could be represented by linear reluctances which can be calculated by well known formulae. This circuit would then behave like a linear resistive electrical network and its solution would be straightforward. The resistive network would be a combination of series and parallel circuits, each representing a particular reluctance or permeance (Luo et al., 1994). Such an approach should produce results which are very similar to those obtained by finite element methods but significantly faster in terms of computation time. This approach should also produce an analytical model with similar accuracy, but easier to manipulate, which gives deeper insight into the nature of the motor.

The process of identifying the correct relationships between the iron and the airgaps is one that needs careful consideration. The analysis of the SyncRM in this thesis introduces the concept of zigzag flux paths. It is proposed that there exists a path for the q-axis flux that allows multiple crossings of the airgap into the stator. The notion of zigzag flux is not new in the area of induction motors (Draper, 1967), however, rather than the zigzag flux wind its way between the stator and the rotor around the airgap, the flux path proposed here crosses the entire rotor body.

This flux path and the non-zigzag path can be characterised by an equivalent q-channel reluctance. The q-channel reluctance is defined as the average reluctance associated with the q-axis flux path where the rotor body is present. The expression for this value can be determined using the idea of modelling the circuit as a network of parallel and series circuits. The approach used in this thesis produces a model that allows the prediction of total flux, for example, of

the motor.

1.2.2 Sensorless Rotor Position Estimation

The SyncRM has received much attention as a suitable candidate for variable speed drive (VSD) applications The available performance makes it competitive with induction motors in terms of the torque available from any given frame size. However, such a drive must be operated using field oriented control since a constant V/f drive has been found to be unstable (Cruickshank et al., 1971).

The induction motor would have the advantage here if it were not possible to determine the rotor position without a shaft mounted position sensor. Traditionally, the position information is provided by a transducer such as an optical encoder or some form of magnetic resolver. In order to make the SyncRM drive more robust and cheaper, it is desirable to design a system that has no need for such devices.

The SyncRM has features which make the sensorless position estimation process more reliable than for the conventional squirrel cage induction motor. The SyncRM possesses saliency which allows the rotor position to be sensed, since the inductances of the stator windings are dependent upon the rotor position. This feature allows rotor position estimation down to zero speed. The variation of inductance is greater with larger inductance ratios and it can be detected as ripples on the current waveform.

1.3 Thesis Contributions

The main contributions of this thesis are:

1. Comprehensive modelling is made of the q-axis magnetic circuit. Models are produced that allow the prediction of machine fluxes based on the physical design of the SyncRM. The models are based on a simple set of

parameters and are confirmed by comparing the results of the analysis with a more complex Finite Element Model (FEM).

2. A new method of sensorless rotor position estimation is developed. The technique uses only the measurement of current available at the stator terminals. The technique requires no detailed knowledge of the machine's magnetic parameters.

3. A method of rotor speed estimation based on a modified zero crossing algorithm is developed. The technique uses consecutive rotor position estimations to provide a speed estimation. The algorithm is robust over a wide speed range.

4. A computer simulation program is developed that explores the algorithms developed for sensorless rotor position and speed estimation. The simulation is written in such a way that the control system can use both the estimated rotor speed as feedback, or the actual rotor speed calculated from machine dynamics.

5. The simulation was adapted for real time software implementation. The system is implemented on a 6-pole, 22kW axially laminated SyncRM. The position and speed estimation is shown to be capable of producing high quality speed control.

The most significant contribution of this thesis is the new, statistical sensorless rotor position estimation. The methodology eliminates the need for knowledge of the machine magnetic parameters. The second major contribution is the identification of the zigzag flux path for the q-axis of the machine.

1.4 Publications

Publications that have resulted from this research include can be placed in two categories.

1. Sensorless Rotor Position Detection

   i. Ciufo, P. P. and Platt, D. "Sensorless Rotor Position Estimation in a Synchronous Reluctance Motor", *Proceedings of the Australian Universities Power Engineering Conference*, volume 1, pages 37–42, 1996.

   ii. Ciufo, P. P. and Platt, D., "Sensorless Rotor Position Estimation of a Synchronous Reluctance Motor", *Proceedings of the 7th International Power Electronics and Motion Control Conference*, volume 3, pages 198–202, 1996.

   iii. Ciufo, P. P. and Platt, D., "Sensorless Rotor Position Estimation for a Synchronous Reluctance Motor", currently under review for submission in the *IEE Proceedings - Electric Power Applications.*

2. Magnetic Circuit Modelling

   i. Ciufo, P. P., Platt, D., and Perera, B. S. P., "Magnetic Circuit of a Synchronous Reluctance Motor", *Electric Machines and Power Systems*, volume 27, number 3, pages 253–270, 1999

   ii. P. P. Ciufo, D. Platt and B. S. P. Perera, "Magnetic Circuit Modelling of a Synchronous Reluctance Motor", *Proceedings of the Australian Universities Power Engineering Conference*, volume 1, pages 37–42, 1994.

1.5 Thesis Outline

The remainder of this thesis is arranged as follows:

- **Chapter 2** is a review of the key papers published in the field of SyncRM research. The Chapter is divided essentially into two sections; one associated with the magnetic circuit modelling and the second the sensorless rotor position estimation.

- **Chapter 3** presents the details of the q-axis magnetic circuit model. The key mathematical expressions are given. The reluctance model is

developed along with expressions for flux and flux density in various parts of the machine structure. Results of this modelling for a typical machine are given.

- **Chapter 4** describes the results of a detailed Finite Element Analysis of the same typical machine used in chapter 3. Evidence to support the zigzag flux path is presented. A comparison is made between the total flux predicted by the analytical model with those obtained from the FEM analysis.

- **Chapter 5** introduces the new sensorless rotor position estimation algorithm. The modified zero crossing algorithm that is used to estimate speed from discrete position information is established. The results of a detailed simulation using the sensorless algorithms developed are presented. The simulation is an extensive test for the algorithm.

- **Chapter 6** gives the results of the implementation of the sensorless estimation schemes on a 6-pole, 22kW Synchronous Reluctance Motor drive system. A set of experimental results generated with and without an encoder is produced.

- **Chapter 7** is a summary of the relevant conclusions from the work presented in this thesis.

- **Appendix A** is a glossary of the terms used throughout this thesis.

- **Appendix B** is the details of the "typical" 2-pole reluctance machine used in the analytical and finite element analyses.

- **Appendix C** presents the detailed mathematics associated with the magnetic circuit modelling presented in chapter 3.

- **Appendix D** explains the notion of vector control and how it relates to this Thesis.

- **Appendix E** shows a schematic of the rotor used in the 6-pole experimental axially laminated machine. Pictures of the finished product are also given.

Chapter 2

Literature Review

2.1 Introduction

The Synchronous Reluctance Motor continues to be the focus of interest for a large number of researchers. It is a motor that has many interesting features worthy of further understanding, development and optimisation. Since the machine is a contender as a replacement for the Squirrel-Cage Induction Motor in certain applications, there is ultimately a very large market for the machine.

There are many areas of research that have been and are still part of the development of the SyncRM. They can be broadly categorised into several main areas, including;

1. Magnetic circuit modelling and design.
2. Control.
3. Sensorless rotor position detection.
4. Performance analysis.

The modelling and design areas are closely inter-related. The whole idea of designing the motor to meet a specific criterion is linked closely to the mod-

elling process since it is from the latter that the design performance can be predicted. Each of these research categories can be broken down into smaller, more fundamental areas of interest. Such a break-down might look like;

1. Magnetic circuit modelling and design:
    i. design of the rotor,
    ii. design of the stator,
    iii. analysis of the d-axis circuit, and
    iv. analysis of the q-axis circuit.
2. Control:
    i. open-loop volts/hertz, or open-loop control,
    ii. field oriented or vector control.
3. Sensorless rotor position detection:
    i. model based techniques,
    ii. statistical techniques, and
    iii. flux estimation methods.
    iv. hybrid techniques.

Each different topical area has a different goal, however there is one underlying central theme for all of this work; a better understanding of the SyncRM. The modelling work provides a great deal of knowledge about the workings of the motor; what sort of parameters should be optimised to highlight certain operational characteristics, prediction of the motor characteristics for a given configuration are but two important goals. The sensorless rotor position detection is required to allow the SyncRM to be used with a modern, high-performance controller without the need for a sensor.

Within the context of the work performed for this thesis, the two main areas of interest are the magnetic circuit modelling of the q-axis and the sensorless

rotor position research. This Chapter is designed to critically review recently published work. The first section discusses research relating to magnetic circuit modelling, with particular relevance to the q-axis magnetic circuit. The second section looks at the various techniques used to estimate rotor position and speed. A third, brief section addresses the general problem of rotor speed estimation from discrete position information. Finally, a conclusion provides a summary of the key features of this Chapter.

2.2 Magnetic Circuit Modelling

The principle aim of this topic of research is the attempt to explain the operational characteristics of the SyncRM as a function of the machine's physical parameters. This may include prediction of the torque ripple as well as the machine fluxes. Of particular interest is the modelling work associated with axially laminated rotors because of its relevancy to this thesis.

In his pioneering paper of 1923, Kostko (Kostko, 1923) introduced the idea of axially laminated anisotropic rotor structures. However, the first prototype of this style of rotor is reported in 1966 by Cruickshank *et. al.* (Cruickshank et al., 1966). One of the key statements of this paper was;

> "The single factor which most influences performance is the design of the rotor magnetic circuit ..."

This statement is still very relevant and in essence has been the driving force of much of the research. Reactance ratios of around 5 were claimed for these early designs. The detailed magnetic circuit analysis was not presented, primarily because this paper was an interim report of work that was being carried out at the time. In a later publication (Cruickshank et al., 1971) a more detailed set of results is presented.

The paper goes on to describe flux distribution and reactance calculations

for both the ideal and practical cases. In the ideal case, the authors assume that the magnetic reluctance across the laminar gaps is infinitely large. The motor being investigated was of a 4 pole construction. The authors identified the effect referred to as "flux whorls", first described by Honsinger (Honsinger, 1971a). These whorls refer to what is essentially a slot leakage effect.

In (Draper, 1967) the claim is made that "zigzag leakage is exclusive to induction motors". Figure 2.1 is offered as an illustration of the effect.

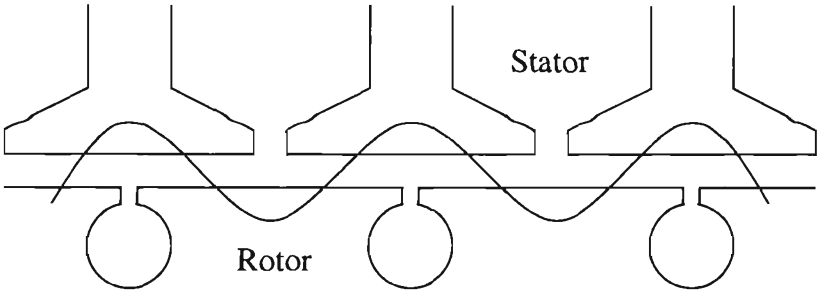

Figure 2.1: Induction Motor Zigzag Flux Path (Draper, 1967)

An analysis is presented that determines expressions for zigzag permeance based on relative positions of the rotor with respect to the stator. The construction of the squirrel-cage rotor is considerably different to that of the axially laminated SyncRM and so the methodology cannot be directly be applied to the modelling in this thesis. However, the notion of this zigzag flux path is similar and can be extended to match the geometry of the SyncRM rotor.

Like many other papers, Marongiu (Marongiu and Vagati, 1991) extols the virtues of high L_d, low L_q and minimising rotor iron loss. The paper looks at a distributed anisotropy rotor, more commonly referred to as an axially laminated rotor. The mathematical model is developed and expressions for the d- and q- axes flux density and flux flowing across the rotor laminations are given. Overall, the modelling utilises the effects of slotting, which as in (Fratta et al., 1993) alludes to the zigzag effect, but fails to directly identify it. Rotor iron loss expressions are also developed.

Miller (Miller et al., 1991), gives an expression for the approximate value of the saliency for an axially laminated rotor as;

$$\frac{X_q}{X_d} = \frac{(tR+g)}{g} = \frac{tR}{g} + 1 \tag{2.1}$$

In this expression, t is the ratio of the flux barrier thickness to the combined thickness of the barrier and lamination, R is the rotor radius and g is the airgap length. X_q and X_q are the equivalent reactances of the q- and d-axes respectively. This produces ratios of the order of 25 which are not tenable.

Spindle drives generally require high torque density and a wide constant-power speed range. High dynamic performance with respect to load disturbances is usually desirable as is a short time overload factor. Fratta (Fratta et al., 1992) looked at the suitability of the synchronous motor compared to the induction motor, taking into account the whole drive system. The two synchronous machines considered are the reluctance motor and the interior permanent magnetic motor. A comparison of the torque capabilities is performed. It is concluded that the SyncRM has a higher torque density. The question of iron losses is raised and there is a discussion relating to the machine that would have the higher value of iron loss. The authors conclude that a correctly designed axially laminated SyncRM exhibits iron losses comparable to the induction machine.

The authors of (Boldea and Nasar, 1991) claim to demonstrate that the "ALA sinusoidal current synchronous motor is superior in all respects to the induction motor and almost equals the performance (torque density, efficiency, power factor) of the PM synchronous motor"; a claim which is well backed up with theory. This paper is one of the few that make a hint of a reference to the zigzag flux issue. The authors refer to an eddy current effect in the rotor. The cause of the eddy currents is unclear. However, they do state the effect can be reduced by breaking the paths of the eddy currents to increase the electrical resistance of the laminations with respect to these currents.

Expressions are developed for torque and airgap flux densities. The effect of stator and rotor slotting is taken into account by the use of the Carter coefficient. They suggest a ratio of 0.33 to 0.4 for the ratio of the insulation lamination thickness to the summed thickness of the insulation plus iron lamination thickness. Other conclusions about the design of an SyncRM are:

1. There is no advantage to increasing the pole-arc to pole-pitch ratio beyond 0.66.
2. The saliency ratio increases with pole-pitch to airgap ratio.
3. The d-axis is low in harmonics whereas the q-axis is rich. Thus, torque pulsations are expected to be small.
4. Even for machines with small pole-pitches, if the airgap is small, the saliency ratio is quite high. Thus moderately high torque densities are possible in small machines.

In 1992, Platt (Platt, 1992) proposed an axially laminated rotor, but with a design that makes full use of the airgap surface. The multi-pole design (more than 2 poles) uses curved section with small radii. This way, the ratio of magnetic to non-magnetic material is maximized in the available pole area. The proposed design allows low reluctance paths to flux from any point in the airgap parallel to the d-axis and high reluctance paths to flux parallel to the q-axis. Since the air/iron ratio in the rotor is similar to the slot/tooth ratio, similar fluxes occur in both regions. The design forces q-axis flux to the pole centres and tends to saturate the iron in this area. Skewing is avoided since there are no teeth or any other salient structures in the rotor. Leakage is accordingly reduced. The zigzag flux mentioned in the paper refers to the flux winding its way along the airgap weaving from the stator to the rotor and back into the stator across the slot openings.

In the paper by Fratta *et. al.* (Fratta et al., 1993), an analytical model based on magnetic interaction between the d- and q-axes due to the stator teeth is

presented. The effect of skewing is discussed and an expression for torque (and torque ripple as a function of design parameters) is developed. It asserts that L_d and L_q are functions of rotor angle. L_d variation is due to a modulation of the Carter's coefficient as the rotor rotates. L_q variations with the rotor angle are caused primarily by variations in the airgap flux which is modulated by mutual positioning of teeth and segments. The paper alludes to the zigzag phenomenon by the mention of circulation flux paths, but fails to isolate this path for rotor positions other than a single relative case between the stator and rotor.

In one of the early finite element (FE) analyses, Soong (Soong et al., 1993) looked at several different mechanisms for calculating the saturation curves of the axially laminated SyncRM. He investigated the accuracy of the parameters obtained using finite element and lumped circuit techniques. Five techniques are suggested of which these latter two are selected as contenders. Comment is made about the time consuming aspects of the FE method and the general practicability of the lumped circuit techniques.

The analytical calculations describe methods for determining the d- and q-axes inductances. The equations use the physical parameters of the machine. They claim;

> "Now if a large number of thin laminations separated by thin layers of insulation are placed in the rotor in such a way that the layers are always perpendicular to the (d-axis) flux lines, then the field distributions would be unchanged. This would cause the (d-axis) inductances to increase."

The mathematics of this claim roughly translates into an increase in d-axis inductance by a factor of $\frac{1}{a}$, where a is the ratio of insulation thickness to the sum of the insulation thickness and lamination thickness. The finite element analysis is performed on a 4 pole, 120W motor with a 24 slot, single layer equi-turn consequent pole, concentric winding. Due to symmetry only $\frac{1}{8}$ of the motor was modelled. A consequence of this was that the effect of the zigzag flux is

not observed.

In (Staton et al., 1993), the authors calculate saliencies for a variety of Syn-cRM configurations. The combinations of ideal rotors and stators with practical rotors and stators are utilised in these calculations. Finite Element Analysis (FEA) is performed on these "designs" in order to calculate the saliencies. One notable observation made by the authors is the significant effect that a slotted stator has on the value of the calculated saliency. The reduction is caused by the saturation of the teeth and yoke.

The paper concludes that there is little value in designing an axially laminated rotor in which the lamination number, N_L, exceeds 10, other than for the purpose of reducing torque ripple. The paper recommends a value of $N_L = 24$ to be a reasonable design. The lamination to barrier thickness ratio, $R_{L/B}$, is best left at unity. There is no consideration for the zigzag effect when calculating the value of N_L. The unity $R_{L/B}$ ratio is derived from the maximisation of the ratio of d-axis permeance to q-axis reluctance in the rotor body.

A recent variation in the design of the axially laminated rotor was performed by Soong (Soong et al., 1995). In this design, flexible rubber-bonded magnetic sheets are interleaved with the magnetic laminations of the rotor. The authors state that the ideal constant-power speed range is approximately equal to half the saliency ratio. There is also a variation on the formula given in equation (2.1) for the maximum possible saliency ratio, based on the inductance of a motor with no rotor and with a solid iron rotor. It is given by;

$$\xi_{mi} = \frac{ar_1}{pg} \tag{2.2}$$

where a is the rotor insulation ratio, r_1 is the airgap radius, p is the number of pole pairs and g is the radial airgap. For the motor under investigation, $a = 0.5$ and $\xi_{mi} = 32$. The actual saliency is considered much lower due to practical factors such as Carter's coefficient, finite pole arc and stator leakage inductance. In general, the measured unsaturated saliency ratio, ξ, is given to

be in the order of $0.2\xi_{mi} < \xi < 0.4\xi_{mi}$.

The practical constant-power speed range is also much lower than that predicted by the saliency ratio, mainly due to saturation. Iron losses and stator resistance have little effect on this speed range. Saturation is said to limit the constant-power speed range to less than 3:1.

The major design considerations for an axially-laminated SyncRM are given as: pole number, pole-piece material, airgap size and rotor insulation ratio. The implication of Equation (2.2) is that 6 pole designs have a poorer intrinsic saliency ratio than 4 pole designs. However, comment is made that the incremental performance improvement with increasing saliency diminishes rapidly once $\xi > 10$ (Betz, 1991). Thus in large motors, 6 or 8 pole designs may yield better performance because of short flux paths and a reduction in saturation due to thinner back iron values. A discussion on the optimal value for the rotor insulation value is also presented. The authors claim that $a = 0.4$ will give the maximum constant-power speed range. They also recommend the use of magnetic pole-pieces in their 4 pole design to give a sinusoidal airgap flux distribution to minimise iron losses at high speed. They conclude that their design with the rubber-bonded magnetic sheets built in to the rotor as the insulation material produces a motor with a extremely wide constant-power speed range.

The aim, according to Boldea (Boldea et al., 1994), of the SyncRM design is to obtain a rugged and simple construction with high torque density, efficiency and power factor. This can be achieved by maximising the $\frac{L_d}{L_q}$ ratio. This ratio is, however, finite. This paper proposes a 2 pole ALA rotor with 66% magnetic and 33% non-magnetic laminations. The ratio of the pole arc to the pole pitch is $\frac{2}{3}$. This machine has reduced cogging torque and an $\frac{L_d}{L_q}$ ratio of 16. Expressions are developed for airgap flux densities along the d- and q-axes. The paper advocates the use of analytical modelling, although with caution. It asserts that the cause of the harmonics in the q-axis field is due to the magnetic/non-magnetic layers of the rotor. The harmonic pattern is also dependent on the number of stator teeth per phase per pole. This the requires a large number of

slots per phase per pole to obtain a high saliency ratio.

A different style of modelling is introduced in (Luo et al., 1994). The authors present a "multiple coupled circuit model". Such a model recognizes that the inductances of an A.C. machine are time varying. The modelling utilizes precalculated inductance versus rotor position curves. Resistance and leakage inductance are considered constant. A 2 pole axially laminated rotor is used. The key issue of this paper is the calculation of the machine inductances. A "developed" model is produced. Parameters of the model are evaluated using basic magnetic circuit principles. Permeance expressions between different magnetic sections are calculated. This produces a simple, network like magnetic circuit model. Mutual and winding inductances are then calculated from machine parameters. This approach is similar to that adopted in this thesis for the calculation of the q-channel reluctance.

In (Coates et al., 1997), Coates recognises the "square airgap flux distribution" effect produced by the axially laminated rotor. He states that "if a square current distribution interacts with this flux, the SyncRM generates its optimal torque". His paper extends the work performed by the author of this thesis and presented in (Ciufo et al., 1994). This modelling work was also extended by the authors and presented in (Ciufo et al., 1999).

2.3 Sensorless Rotor Position Estimation

The title of this section loosely describes the process used to estimate the rotor position and speed without the use of a shaft sensor. The ability to perform this estimation is one of the desirable features of the SyncRM. Despite the suitability of the SyncRM design for the sensorless estimation task, the process of obtain an accurate estimate in real-time is not easy.

The techniques described in the literature fall broadly into two categories; the parameter dependent and parameter independent method. The parameter

dependent technique relies on knowledge of the SyncRM parameters for estimating rotor position or speed. Properties such as L_d, L_q, R_s (stator winding resistance) would be required for such an algorithm. This group suffers from limitations since the parameter-dependence means that the method requires intimate knowledge of the machine and it introduces sensitivity to parameter variations. The alternate approach does not suffer from such drawbacks. Whichever technique is chosen, the variation of inductance with rotor position forms the basis of the estimation approach.

One of the early papers published in the field is one by Bowman (Bowman and Platt, 1993). In this paper, a theory for rotor position and angular speed estimation using an ideal linear d-q model is proposed. A 2 pole machine was constructed using magnetic and non-magnetic sheets instead of thin laminations for the rotor. This introduced some slotting effects into the variation in inductance. The full set of six voltage vectors was applied to this particular machine for a short duration and the change in current, di was noted. The results obtained compared favourably to those predicted by the linear modelling. In this way, the authors suggested that their theoretical method could be used to predict rotor position and speed without a sensor. The work in this paper was preliminary and further investigation was required to incorporate the estimation process into control algorithms.

Kreindler (Kreindler et al., 1993) proposed a control methodology based on the determination of the spatial position of the airgap flux from the third harmonic component of the stator phase voltages. The authors suggest that when the machine is wye-connected without a neutral connection, the sum of the three phase voltages results in a signal that is dominated by the third harmonic component. The technique devised provides coarse position estimates, updated at $\frac{\pi}{3}$ increments. Other methods are required to estimate rotor position in between these position updates. The scheme is converted to an absolute encoder by keeping track of the number of zero crossings of the third harmonic voltage. This methodology also suffers from a limited number of rotor position

samples. Combined with the parameter-dependence, this technique also suffers at low speeds. Perhaps the greatest drawback of the method is that it fails to predict absolute position. Although the authors are able to used their method to start the machine, that starting position is unknown.

In a series of papers published by Arefeen (Arefeen et al., 1994a), (Arefeen et al., 1994b), a method that uses a modified inverter switching technique is proposed. A current regulated pulse width modulated converter is used. The idea turns off both the switches of a particular phase when the current of that phase crosses zero. The remaining two phases are switched to be in series with each other and the current in these two phases is then controlled at a constant value. The current in the open circuit phase is zero, but the current in the series phases induces a voltage in the first phase. Knowing the mutual inductances of the phases, an expression can be found for the rotor speed. The rotor position between the zero crossings is determined by extrapolation. This method requires knowledge of the machine parameters. There is a limit, also, to the number of rotor position estimations per revolution. Consequently, this technique is more suited to drive systems with larger time constants.

In (Lagerquist et al., 1994), the authors use the flux-linkage to estimate rotor speed. A closed loop torque vector controller based on the work by Boldea (Boldea et al., 1991) is implemented. There are problems associated with this technique that the authors compensate for in their control system. The resultant speed estimate suffered from a high frequency jitter which they remove using a first order low pass filter. The resultant delay of 2-5 ms is regarded as acceptable. This ripple caused further problems with the stability of the control system at high speeds. An increase of the PI gain and the bandwidth of the control system improved the response. However, the effects of the ripple in the speed estimate was not resolved and it continued to plague the proposed scheme.

The authors of (Schroedl and Weinmeier, 1994) combine two methods of position sensing and use them along with Kalman filtering to obtain optimal estimates. For low speeds, the indirect flux detection by on-line reactance mea-

surement (INFORM) method is used. In this method, the idea is to measure the behaviour of the current space phasor when a test vector is applied in real time. This is a lengthy procedure in terms of computational load. This is not seen as an issue since the technique is only used at low speeds. At higher speeds, the authors introduce an EMF Model based scheme. Under this scheme, the idea is to examine the SyncRM's behaviour during short circuit of the terminals. This corresponds to two particular switching states of the inverter. The output from the INFORM method and the EMF model are presented to a Kalman filter based on a state model of the mechanical part of the reluctance motor. The two techniques employed do not rely on knowledge of the machine parameters.

In (Matsuo and Lipo, 1994b), the rate of change of current in the current ripples resulting from the inverter switchings, combined with knowledge of the motor reactances is used in the estimation algorithms. The dependence of the self and mutual inductances on rotor position is exploited. The authors note that the performance of their algorithm is better at low speed. The algorithms presented are not suitable for the full speed range of the SyncRM. For an effective sensorless system, the method needs to be combined with some other technique whose performance is acceptable over the full range of the SyncRM's operating range.

A paper by Lin *et. al.*, (Lin and Liu, 2000), utilises the zero vector switching positions to assist in the estimation of rotor position from line currents. This is essentially an extension of the work presented in (Matsuo and Lipo, 1994b), but with a greater degree of success. The authors introduce the use of additional zero vector selections at high speeds to successfully extend the range of valid speeds for this method.

The approach proposed by Bowman (Bowman and Platt, 1993) was extended by Xiang (Xiang and Nasar, 1995). He derives an expression for on-line estimation of rotor position and speed. A digital simulation study demonstrated to high accuracy of the method in both the transient and steady-state operation. Some low pass filtering was required to smooth the speed estimation, but

this had limited impact in the quality of the estimate. A startup algorithm is proposed that produces good results. Even though this is one of the early papers published in the area of sensorless position estimation, the results obtained were of high quality. Their methodology produces separate estimates of rotor absolute position and rotor speed. Perhaps the greatest drawback is that the modelling is dependent on the motor parameters, as are all model-dependent schemes.

Another paper to note (Jovanovic et al., 1995) presents a simulation of a sensorless system that utilises currents and voltages sampled at consecutive intervals to solve two simultaneous equations to give the instantaneous position and angular speed of the rotor. The authors state that "the fundamental principle of the estimation technique is the detection of stator winding inductance variations with rotor position, by examination of the switching ripple on the current waveforms". This paper also, in a sense, extends the work in (Bowman and Platt, 1993). It does so since it takes a simple dq model of the reluctance machine and extends the model to produce expressions for rotor position in terms of machine inductances. The key advantage of this technique is the high rate of calculation since the sampling takes place at the inverter switching frequency. Their follow up paper, (Jovanovic et al., 1998), uses the technique in a control system and practical results are presented. The estimate of rotor position is fed into a closed-loop observer to predict new values of rotor position and speed. The technique has a wide speed range of applicability and good accuracy, although an accuracy analysis is not presented. The one drawback of this method is, once again, the required knowledge of machine parameters to make the system work properly.

Several methods utilising a high frequency stator current injection scheme have been proposed by various authors. Consoli *et. al.* (Consoli et al., 1998), (Consoli et al., 1999) employ such a scheme that requires no knowledge of the machine parameters. The technique works for a wide speed range, including start-up and can be implemented in discrete hardware. Kang, Jung *et. al* (Kang

et al., 1998), (Ha et al., 1999) propose a technique that utilises a high-frequency current injection methods in the low-speed region and a flux estimation method based on stator voltages in the high-speed region. The scheme provides good, robust results. There is a low dependence on the machine parameters. The key disadvantage of these schemes is the modification of the inverter switching scheme to inject the required current. This adds another level of complexity to the control scheme on top of the additional signal processing required to obtain rotor position estimation. Jansen and Lorenz (Jansen and Lorenz, 1995) adopt a more generic approach, suggesting a scheme which is suitable for PWM inverter driven induction, synchronous and reluctance machines. This work was extended in (Degner and Lorenz, 1998) to include machines with multiple spatial harmonic saliencies.

The sensorless position estimation scheme presented in this thesis has been published in (Ciufo and Platt, 1996) and a further publication is currently under review for by the *IEE Proceedings - Electric Power Applications.*

2.4 Generic Estimation Methods

The importance of sensorless rotor position and velocity estimation is not restricted to its application to the Synchronous Reluctance Motor. Generally, it has relevance in all areas of motor drive systems. Not only is the sensorless schema of importance, but so is the idea of speed estimation from discrete position data. To this end, there have been several papers published over the years that have tried to present a generic approach to the idea of rotor position and speed estimation.

In many of the techniques discussed in Section 2.3, the resulting output is a value of rotor position. In much the same way that an encoder provides position information at consecutive sampling instants, some estimation schemes provide a position estimate at consecutive sampling instants. If the desired control variable is speed, then these consecutive position values need to be converted

to a speed estimate so that the control loop can be closed.

Saito *et. al* (Saito et al., 1988) recognised this problem and attempted to formulate a scheme to estimate speed from discrete position data provided by an encoder. They present a simple scheme that takes into account the overall computational requirement. Since the paper was published in 1988, the processing power at the time required simple schemes. The paper proposes a method in which the instantaneous speed at the time point of control can be estimated from the detected average speed. The authors recognised the main shortfall in their technique; poor accuracy when short speed response time is required. Their method assumes the drive speed to vary in between sampling points as either a first-order of second-order function. The claim by the authors that their system improves the responsiveness of a control scheme for mechanical systems that suffer from torsional oscillations is really only highlighting the problem of their speed estimation algorithm; poor performance for short time estimation.

Lorenz and Van Patten, (Lorenz and Patten, 1991), also recognised the desire to use the position feedback transducer as the sole sensor for full closed-loop speed and position control. They present a detailed analysis of the approaches that have been used and propose their own technique for overcoming some of the limitation of current schemes. They also demonstrate better performance than that of a system that utilises a dc tachometer for speed feedback. They introduce the idea of using a closed-loop observer to estimate unmeasured variables such as speed. A consequence of the validity of their work is that other researchers such as Jovanovic *et. al* (Jovanovic et al., 1998), (Jovanovic et al., 1995) and Kreindler *et. al* (Kreindler et al., 1993) have applied their methodology to control schemes for the Synchronous Reluctance Motor using estimated position information.

Another paper that investigates algorithms for estimating speed from discrete position data is one by Brown *et. al.* (Brown et al., 1992). They give examples of speed estimators based on "lines per period, reciprocal-time, Taylor

series expansions, backward difference expansions and least-square curve fits". Whilst a broad range of techniques are presented, in conclusion there does not appear to be any one method suited to a drive system that has a broad dynamic response and speed range requirement.

2.5 Conclusions

The modelling of the magnetic circuit for the SyncRM has been actively pursued for a long period of time. From the early work by Kostko, right up to the recent publications, interest has continued in the optimisation of the rotor design to obtain the best performance from the reluctance motor. One of the key design parameters of the SyncRM is the ratio of the d- and q-axes inductances. In the research work that has been published, the magnetic circuit of the q-axis has not been subject to a thorough analysis.

One area that has been overlooked is the relationship between the alignment of the stator and rotor q-axis. In general, the research performed has assumed a perfect alignment between the two. In the FE approach, only part of the machine is modelled since an exact symmetry is assumed. However, because of stator slotting, this is not entirely true. Indeed, as will be shown in this thesis, a combination of slotting effects with thin rotor laminations can lead to an effect whose result is an overall reduction in the saliency ratio of the Synchronous Reluctance Motor.

The literature review indicates a recent trend of sensorless position techniques based on high frequency stator current injection. There have been many other methods suggested over the years, all attempting to exploit the saliency feature of the SyncRM. Implementation of sensorless control in real-time has not been easy and it is only in recent times that true progress toward successful schemes have been published.

Much of the work presented contributed to the overall knowledge base re-

quired for research into sensorless estimation strategies. There are limitations to the published sensorless estimation schemes, including:-

- Limitations on the degree of accuracy: many papers have investigated new techniques without a proper accuracy analysis.
- Modification of the inverter switching scheme: forcing the inverter into a specific state in order to make specific measurements for model based methods increase the order of control complexity.
- Estimation rate can be slow because of the complexity of the technique: this leads to an overall reduction in performance.
- Dependence on knowledge of machine parameters: this is a limitation since the control scheme requires accurate modelling of the motor in order to perform the estimations. Variation in the motor parameters would lead to further inaccuracies in the estimation process. For a fully fluxed machine, L_d varies due to iron saturation.
- Injection of a special high frequency signal and subsequent signal processing.

The sensorless position estimation algorithm presented in this thesis overcomes some of these limitations.

Chapter 3

Magnetic Circuit Modelling

3.1 Introduction

For any particular motor with a given rotor position, it is possible to construct a magnetic circuit which describes it with a reasonable degree of accuracy. We would simply assume that all the sections of iron were magnetic short circuits (nodes) and that the airgaps separating these pieces of iron could be represented by linear reluctances which can be calculated by well known formulae. This circuit would then behave like a linear resistive electrical network and its solution would be straightforward. The resistive network would be a combination of series and parallel circuits, each representing a particular reluctance or permeance (Luo et al., 1994). Such an approach should produce results which are very similar to those obtained by finite element methods but significantly faster in terms of computation time. This approach should also produce an analytical model with similar accuracy, but easier to manipulate, which gives deeper insight into the nature of the motor.

There is a very important advantage to a designer in having a (good) analytical model of the machine. The magnetic design can be specified with very few parameters. The effect of changing them can be seen quickly, or a design could be optimised over this parameter space for some performance measure.

This is in distinction to a finite element model which is much more complex to devise and whose parameters are difficult to change.

The process of identifying the correct relationships between the iron and the airgaps is one that needs careful consideration. The analysis of the SyncRM in this dissertation includes the concept of zigzag flux paths. It is proposed that there exists a flux path for the q-axis flux that allows multiple crossings of the airgap into the stator. This is an extension of the zigzag leakage flux path presented in (Draper, 1967).

This flux path and the non-zigzag path can be characterised by an equivalent q-channel reluctance. The q-axis channel reluctance is defined as the average reluctance associated with the q-axis flux path where the rotor body is present. The expression for this value can be determined using the idea of modelling the circuit as a network of parallel and series circuits. The approach used in this analysis produces a model that allows the prediction of total flux, for example, of the motor.

This Chapter presents a new model for the q-axis magnetic circuit of the SyncRM. It includes the zigzag flux path and shows how this additional flux path leads to an increase in the inductance of the q-axis. The first section presents the model for the q-axis reluctance channel magnetic circuit. A description of the circuit is given and the network of reluctances that represent this circuit. The next section develops formulae for describing this model. Following this work, an expression for the general solution of the q-axis flux is presented. This work is extended into an expression for the general solution of yoke flux by the addition of a model for leakage reluctance. A short description of the pole side reluctance is presented and its relevance to the model described. The next two sections present actual solutions for the q-axis flux, airgap flux densities and tooth and yoke flux densities for two distributions of stator current. The final section is a brief summary of the results presented as well as some visualisations of the results obtained for a sample motor.

3.2 The Q-Axis Reluctance Channel Magnetic Circuit

In modelling the SyncRM, problems are encountered when attempting to find a value for the q-axis reluctance. The q-axis flux paths are complex and are not well understood. There are essentially 2 main paths by which the flux flows in the q-axis;

1. through the rotor body across the laminations, and
2. following a zigzag path across the airgap.

The zigzag flux path is a path that "winds" its way through the laminations of the rotor. The direct path, for the q-axis, through the rotor is a high reluctance path because of the alternate magnetic and non-magnetic laminations. The formation of the alternate flux path, the zigzag path, occurs because of the alignment between the rotor laminations and the stator teeth. The formation of the alternate flux path occurs when the thickness of the laminations used in the rotor is in the order of 10% to 25% of the stator tooth width.

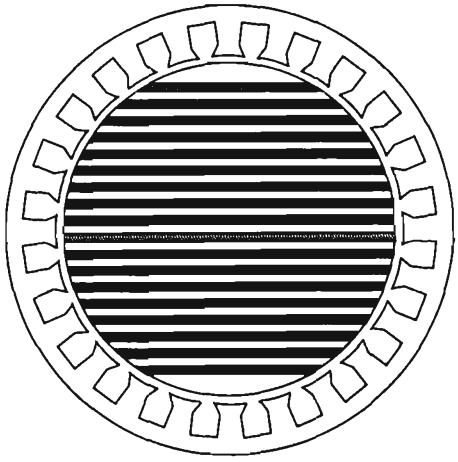

Figure 3.1: Aligned Rotor Position

Identifying the alternate "zigzag" flux path is important. In Figure 3.1 the rotor is positioned in the "Slots Exactly Aligned" position. This means that

the rotor laminations form a path from a stator slot on one side to the same relatively positioned slot on the other side. Visualising how this stator-slot-to-rotor-lamination changes as the rotor position changes can be simplified by developing the above Figure.

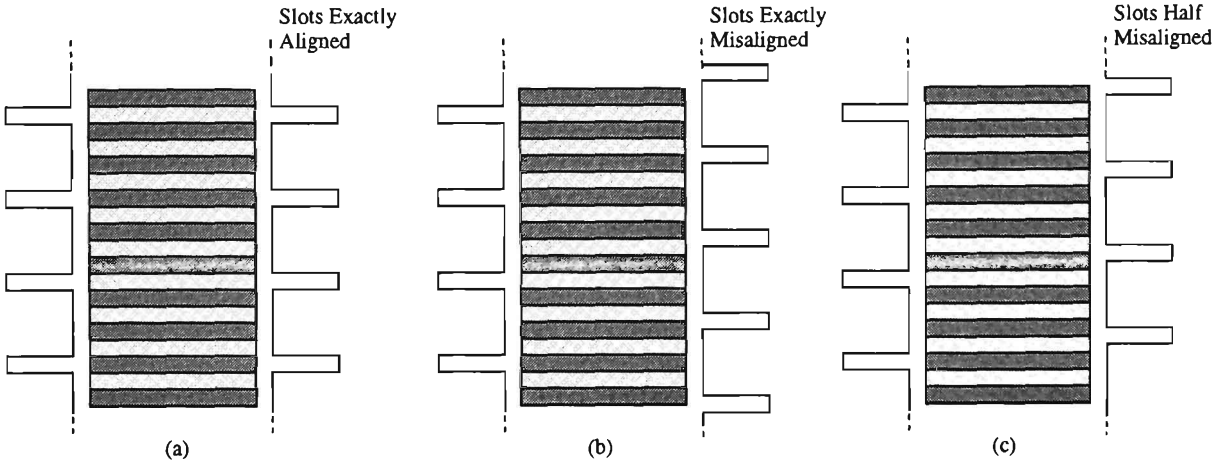

Figure 3.2: Rotor Alignment

In Figure 3.2, the rotor and the stator have been converted to a flattened version and the role of the two reversed; the rotor is now considered stationary and the stator is the moving part. For the sake of clarity, the laminations of the rotor are shown to be thick, a design that would not normally be used. Ordinarily, the spacing between magnetic and non-magnetic laminations would be a function of angular position. The laminations are shown as equidistant for illustrative purposes only. The purpose of this model is to try to establish a simple, reasonable, expression for the reluctance of the q-axis. Ultimately, this value can be used to predict values of airgap flux in the SyncRM.

Figure 3.2(a) represents the rotor in the same position as that in Figure 3.1. Figure 3.2(b) illustrates the rotor-stator relativity if the rotor was to be misaligned by the value of one stator slot pitch relative to the rotor position in Figure 3.2(a). Figure 3.2(c) is the rotor misaligned by half of one slot pitch.

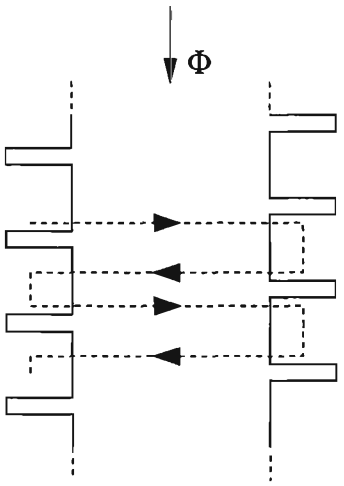

Figure 3.3: Zigzag Flux Path

If the representation is taken one step further, then using Figure 3.3, the zigzag flux path is illustrated. With the rotor positioned in the "half misaligned" position, the q-axis flux has a path that winds its way through the rotor and stator.

The expression developed for the q-axis reluctance is based on the "half misaligned" case. This is the "average" reluctance of the q-axis. The variations in reluctance as a function of rotor position are well known (Fratta et al., 1993), (Staton et al., 1993). This model does not seek to derive expressions that can be used to calculate the variations in reluctance with rotor position.

The zigzag flux is q-axis flux that winds its way through the rotor body. It does so because if we take a "snapshot" of the rotor at any instant in time, sections of the rotor laminations can be identified which pass flux from a stator tooth on one side of the rotor to a stator tooth on the other side. This is true for a variety of positions of the rotor. These sections of rotor lamination will represent negligible reluctance between these teeth, through the rotor body, but there will still be the reluctance of the airgaps. The adjacent section of laminations in the rotor align between a stator tooth on one side and a slot opening on the other. Accordingly, these laminations are unable to pass zigzag flux between teeth on opposite sides of the stator. However, it is still capable of passing flux across the body of the rotor and is therefore represented by a

simple reluctance.

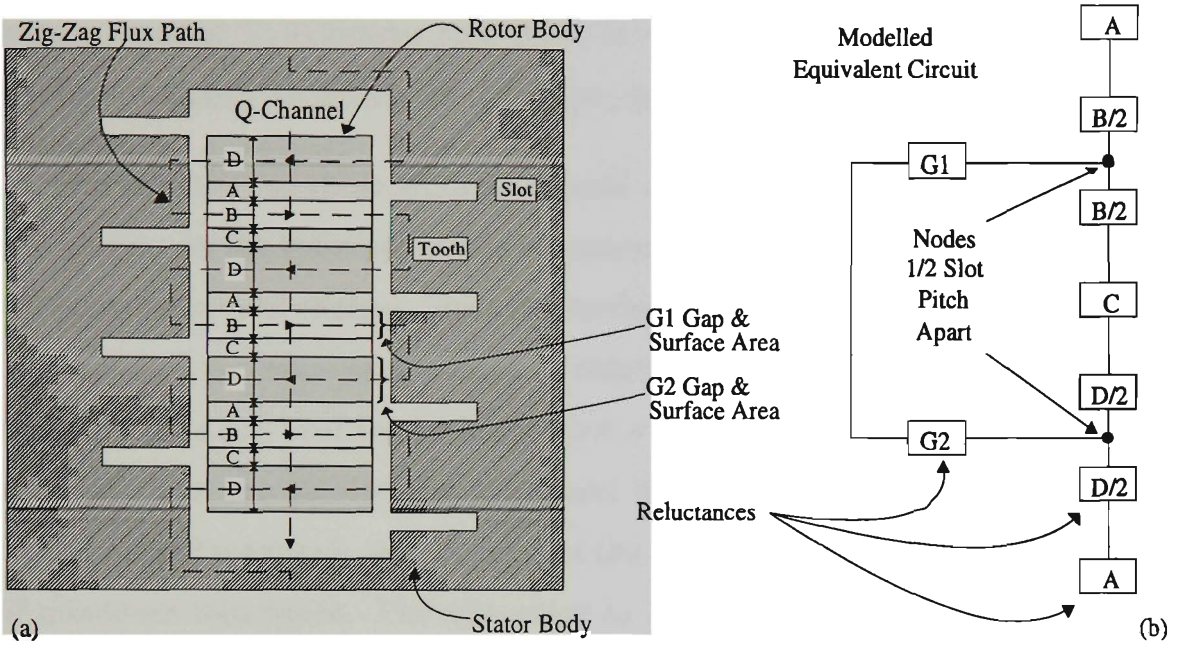

Figure 3.4: (a)Q-Axis Reluctance Model, (b)Equivalent Circuit

Figure 3.4 is an extension of the illustration presented in Figure 3.2. In the previous Figure, the rotor was illustrated in three relative positions. In Figure 3.4, only one position is represented and the path of the zigzag flux is drawn. The diagram of Figure 3.4 is best described as that of a developed section from a reluctance motor. The diagonally striped area represents the stator body. The zigzag flux will find its way through the rotor and stator body in the manner indicated. The rotor body of Figure 3.4(a) is classified into sections labelled A to D. These sections do not represent the alternate magnetic and non-magnetic laminations found in an axially laminated rotor. Instead, they represent sections through the rotor body that facilitates the passing of zigzag flux from one side of the stator to the other. If there is a slot opening at one of the airgaps, zigzag flux will not pass.

Section D is located between a tooth on one side of the stator and a tooth on the other side. The zigzag flux is expected to traverse this path since it represents a path of low reluctance from one side of the stator to the other. Section A is different to section D since it represents the area opposite a slot

opening. The zigzag flux is assumed not to go across this section (from left to right or vice versa) as the slot opening is a high reluctance path. The next section, section B, is similar to section D, except the thickness of this area is smaller compared to section D. Likewise, section C is similar to section A.

The thickness of these sections depend on the alignment between the rotor and stator. As the rotor spins, the alignment of the slot openings on either side of Figure 3.4(a) will change. Since the modelling technique that is proposed here does not seek to define exact values of reluctance but rather quantities that are useful for an analytical model of the motor, average reluctance is the quantity required. The two extremes of alignment have the stator slots exactly aligned for the case of maximum reluctance and the slots exactly misaligned for the case of minimum reluctance. The alignment in Figure 3.4(a) should be interpreted as that alignment which models the average reluctance of the q-channel. This case represents an alignment half way between the two extremes.

The whole rotor body is made up of sections which may be represented in one of these four ways (A, B, C or D). Thus, we may draw a magnetic circuit which represents the path of the q-axis flux through the rotor. Such a circuit is illustrated in Figure 3.4(b). The three series reluctances, located between the $\frac{1}{2}$ slot pitch nodes of Figure 3.4(b), represent reluctances through the body of rotor. The reluctance of the air gap is represented by G1 and G2. The reluctance that represents the airgap at either end of the q-axis main flux path is not represented in this Figure. This is generally a significant reluctance that can be complicated by the shape of the rotor surface.

3.3 The Q-Channel Reluctance

In the previous section, a simple physical model was presented that consisted essentially of a network of reluctances. Expressions for these reluctances need to be determined. In addition to the reluctances of the airgaps, the effect of the slotting of the stator and of the rotor is taken into account. This is done

so using Carter's Coefficient. With a slotted surface, the effective area of the flux path is reduced and the simple expression for reluctance can no longer be utilised. Both the rotor and the stator are slotted, so the equivalent airgap needs to be considered from two frames of reference; a slotted stator and a solid rotor, followed by the slotted rotor and solid stator.

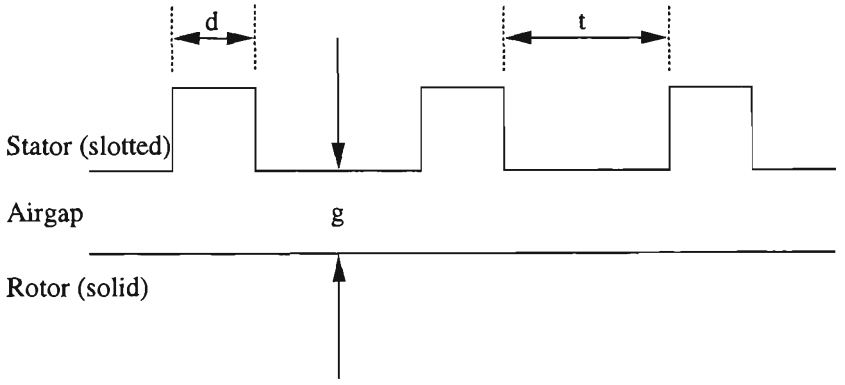

Figure 3.5: Carter Coefficient - Slotted Stator

Figure 3.5 represents the case of the slotted stator and the solid rotor. The equivalent airgap is found using the geometry of the slots and is given by the expression (Slemon and Straughen, 1980);

$$g_{e1} = \frac{g(t+d)}{t+kd}, \qquad k = \frac{1}{1+\frac{d}{5g}}. \tag{3.1}$$

In (3.1), t represents the stator tooth width, d the stator slot width and g the nominal airgap value. Equation (3.1) can be simplified to

$$g_{e1} = K_{c1}g \tag{3.2}$$

where K_{c1} is the Carter coefficient for the case of a slotted stator with a solid rotor. In the other case, the solid stator is combined with a slotted rotor as illustrated in Figure 3.6.

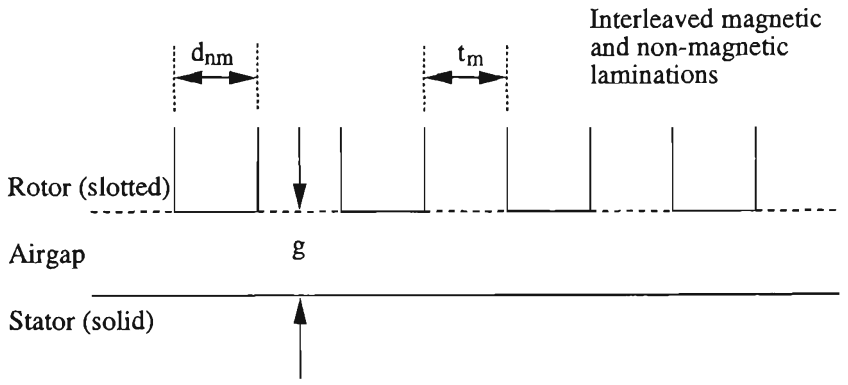

Figure 3.6: Carter Coefficient - Slotted Rotor

The expression for the equivalent airgap in this case is given by (Slemon and Straughen, 1980);

$$g_{e2} = \frac{g(t_m + d_{nm})}{t_m + k d_{nm}}, \qquad k = \frac{1}{1 + \frac{d_{nm}}{5g}}. \tag{3.3}$$

In (3.3), d_{mn} represents the thickness of the non-magnetic lamination in the rotor, t_m the 0 lamination and g the nominal airgap.

This can be simplified to

$$g_{e2} = K_{c2} g. \tag{3.4}$$

Finally, in endeavouring to take into account the effects of slotting of both the rotor and the stator, both expressions can be combined to form a single expression for the equivalent airgap.

$$g_e = K_{c1} K_{c2} g \tag{3.5}$$

One more section of the physical model needs to be considered before a practical expression for the q-axis reluctance channel can be derived; the $\frac{1}{2}$ slot pitch equivalent circuit. This is represented by the drawing of Figure 3.4(b). The circuit consists of three series reluctances, connected in parallel with two other series reluctances. The three reluctances represent reluctances through the rotor body. A general expression for the reluctance of an airgap is given by

$$\Re = \frac{l}{\mu_o A}. \tag{3.6}$$

In equation (3.6), l represents length, A the surface area and μ_o the permeability constant, $4\pi \times 10^{-7}$A/m. This general expression is used as the basis for all reluctance calculations in the modelling. The area term, A of the above expression, is determined from the surface area of the tooth face A_s. This area is calculated by the expression

$$A_s = L_s \frac{2\pi R_s}{pN_s} 0.5 \tag{3.7}$$

where A_s is the $\frac{1}{2}$ slot pitch surface area, L_s is the length of the stator, R_s the stator radius, p is the number of pole pairs and N_s is the number of slots per pole pair. In the case of airgap $G1$, the surface area used to calculate the reluctance is $0.25A_s$ and in the case of airgap $G2$ it is $0.75A_s$ since we are considering an average rotor position. The airgap length for both $G1$ and $G2$ are the same. Therefore the expressions for these two airgap reluctances is

$$\Re_{G1} = \frac{g_e}{0.25\mu_o A_s}, \qquad \Re_{G2} = \frac{g_e}{0.75\mu_o A_s}. \tag{3.8}$$

To calculate the length of the slot pitch, including one tooth and one slot opening, the expression

$$l_{sp} = \frac{2\pi R_s}{pN_s} \tag{3.9}$$

is used.

Finally, the expression for the reluctance through the rotor body itself is to be determined. These are the reluctances represented by the terms $\frac{B}{2}$, C and $\frac{D}{2}$ in Figure 3.4(b). There is a small complication in finding the expression for these values; the rotor is cylindrical. A consequence of this is that the value of A, the cross-sectional area, changes as the rotor body is traversed. In this analysis, we use an average value. The cross sectional area of the rotor is given

by

$$A_{rl} = L_R W_R. \tag{3.10}$$

The rotor stack length, L_R, is fixed, but the rotor lamination width can be complicated by the design of the rotor, in particular, multi-pole (greater than 2 pole) designs. The expression for this reluctance is given by

$$\Re_R = \frac{0.5 l_{sp}}{\mu_o A_{rl}} K_a, \tag{3.11}$$

where l_{sp} is the length of the slot pitch (one tooth plus one slot), A_{rl} is the average surface area of the cross section of the rotor and K_a is a constant expressing the ratio between magnetic and non-magnetic material in the rotor. In general, K_a is 0.5, indicating equal thickness laminations.

With all these expressions in hand, it is now possible to find a value for the q-channel reluctance. The procedure would be as follows;

1. calculate the parameter l_{sp} using equation (3.9),
2. calculate the parameter A_s using equation (3.7),
3. calculate the parameter A_{rl} using equation (3.11) using an average value for the rotor lamination width,
4. calculate the effective airgap, g_e, taking into account the slotting of the stator and of the rotor,
5. calculate the reluctances $\Re_{G1}$, $\Re_{G2}$ and $\Re_R$,
6. lastly, calculate $\Re_{eq}$, the q-channel reluctance from the series/parallel combination of $\Re_{G1}$, $\Re_{G2}$ and $\Re_R$.

The final value will have the units of A/Wb. In the analysis of this dissertation, this value is normalised to A/Wb/m by multiplying the result by $1000/l_{sp}$ (l_{sp} is

given in millimetres). This should lead to an expression for the q-axis reluctance per metre of distance through the rotor in the q-direction.

Now that an expression has been developed for the q-channel reluctance, it is possible to move on with the modelling and find a general expression for the q-axis flux. In the next section, such an expression is derived.

3.4 General Solution for Q-Axis Flux

The process of developing an expression for the q-axis flux requires the extension of the physical model already described by Figure 3.4. This representation of the SyncRM is taken one step further by Figure 3.7.

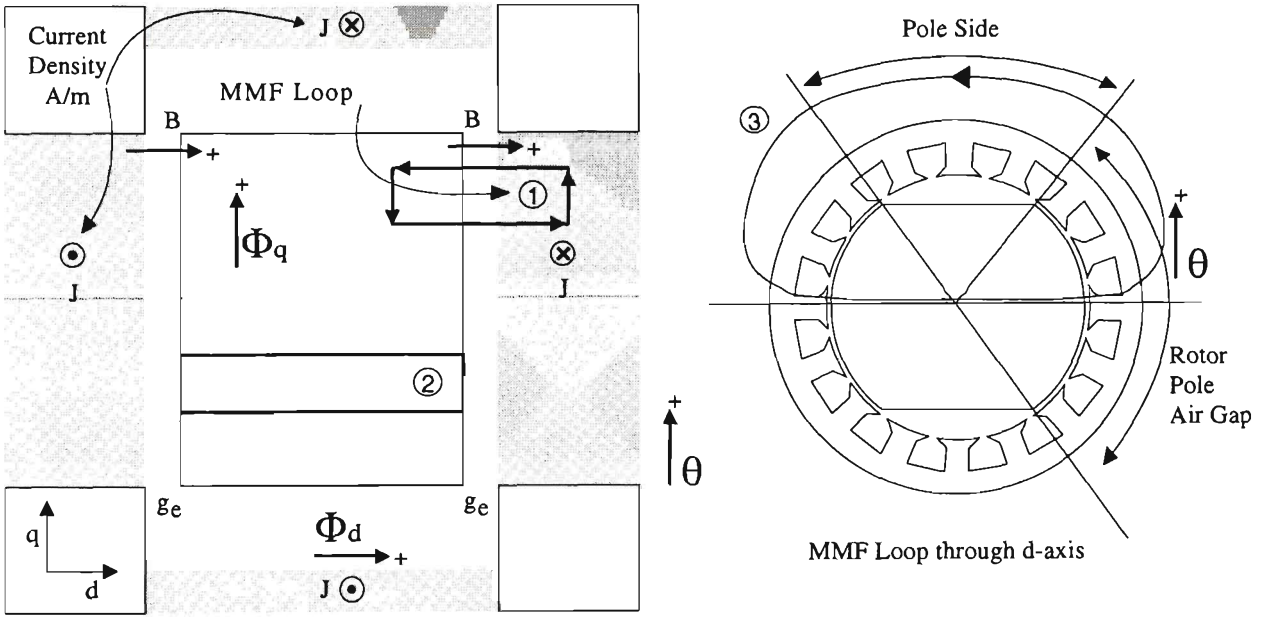

Figure 3.7: Machine Model

The rotor is represented by a channel which conducts flux in the q-axis with a known reluctance per metre. In the d-axis, it is a magnetic short circuit. Several assumptions are made at this point in order to complete the modelling;

1. The teeth and slots of the stator are "smeared" into a single entity. The

result of this assumption is that the stator slot effects on the flux distributions can be represented by differential equations.

2. The permeability of the iron is infinite and eddy current effects are neglected.

3. In the case of sinusoidal stator excitation, a sinusoidally distributed winding is assumed.

The method of analysis chosen requires that an expression be found for the q-axis flux in the first instance. In Figure 3.7 this is represented by the quantity Φ_q. The expression for Φ_q is found by considering three closed loops, as indicated by the symbols ①, ② and ③.

The circuits indicated by ① and ③ represent paths over which the MMF is computed, whilst ② encloses a volume in which flux continuity must be maintained. The circuit ① and volume ② are intended to include only an incremental angle $d\theta$. From these fundamental circuits, an expression for the general solution of $\Phi_q(\theta)$ can be determined.

In Figure 3.7, following the path around loop ① in the direction shown, leads to the expression

$$J(\theta)Rd\theta_m = \frac{g_e}{\mu_o}\left[B_g(\theta) - B_g(\theta + d\theta)\right] + \Re_q\Phi_q(\theta)Rd\theta_m \tag{3.12}$$

The term θ_m relates to the *mechanical* radians, not electrical radians. In order to convert to electrical radians, a term for the number of pole pairs needs to be introduced. Unless explicitly stated, all angles are expressed in electrical radians. Simplifying equation (3.12) and converting to electrical radians leads to

$$J(\theta)Rd\theta\frac{1}{p} = \frac{-g_e}{\mu_o}dB_g(\theta) + \Re_q\Phi_q(\theta)Rd\theta\frac{1}{p}. \tag{3.13}$$

Equation (3.13) simplifies to

$$J(\theta)R = \Re_q\Phi_q(\theta)R - \frac{g_e}{\mu_o}\frac{dB_g(\theta)}{d\theta}p. \tag{3.14}$$

Formulating the equations for continuity of flux in region ② leads to the initial expression

$$\Phi_q(\theta) - \Phi_q(\theta + d\theta) + RL_R B_g(\pi - \theta)d\theta_m - RL_R B_g(\theta)d\theta_m = 0. \tag{3.15}$$

Converting this expression to electrical radians using the relationship $\theta = p\theta_m$, and simplifying reveals

$$\frac{d\Phi_q}{d\theta}p - RL_R[B_g(\pi - \theta) - B_g(\theta)] = 0. \tag{3.16}$$

Note that positive B_g flows from rotor to stator on the right hand side, but stator to rotor on the left hand side of Figure 3.7. The final equation required to find an expression for the q-axis flux is found by analysing the d-axis MMF loop. In Figure 3.7 this is illustrated as loop ③.

$$\int_{\theta}^{\pi-\theta} J(\theta)Rd\theta\frac{1}{p} = \frac{g_e}{\mu_o}[B_g(\theta) + B_g(\pi - \theta)] \tag{3.17}$$

Using equations (3.14), (3.16) and (3.17) an expression for the general solution of the q-axis flux can be determined. The working for this solution is given in Appendix C, Section C.2. It is a linear, non-homogeneous differential equation.

$$\frac{d^2\Phi_q(\theta)}{d\theta^2} - \frac{2\mu_o R^2 L_R}{p^2 g_e}\Phi_q(\theta) + \frac{\mu_o R^2 L_R}{p^2 g_e}[J(\theta) - J(\pi - \theta)] = 0 \tag{3.18}$$

In this equation, the angle θ is the pole arc angle which ranges from $\frac{-\theta_p}{2}$ to $\frac{\theta_p}{2}$, where θ_p is the pole pitch. Equation (3.18) is a general solution only. Specific solutions are found by using this equation along with a known distribution of current, $J(\theta)$ (MMF), in the stator. Several simple constants are defined;

$$b = \frac{2\mu_o R^2 L_R \Re_q}{p^2 g_e}, \quad c = \frac{\mu_o R^2 L_R}{p^2 g_e} = \frac{b}{2\Re_q}. \tag{3.19}$$

Now, equation (3.18) can be re-written as

$$\frac{d^2\Phi_q(\theta)}{d\theta^2} - b\Phi_q(\theta) + c[J(\theta) - J(\pi - \theta)] = 0 \tag{3.20}$$

The solution to Equation (3.20) is an expression that represents the equation for the q-axis flux.

3.5 Slot Leakage Reluctance

With the establishment of the model for the q-axis flux, a means of testing this model and expanding the model to include other parts of the machine is required. This section provides an analysis of stator slot leakage.

In order to extend the model, one needs to consider the effect of leakage and airgap flux. The following Figure is a close up view of a small section, $d\theta$, of the airgap of the machine.

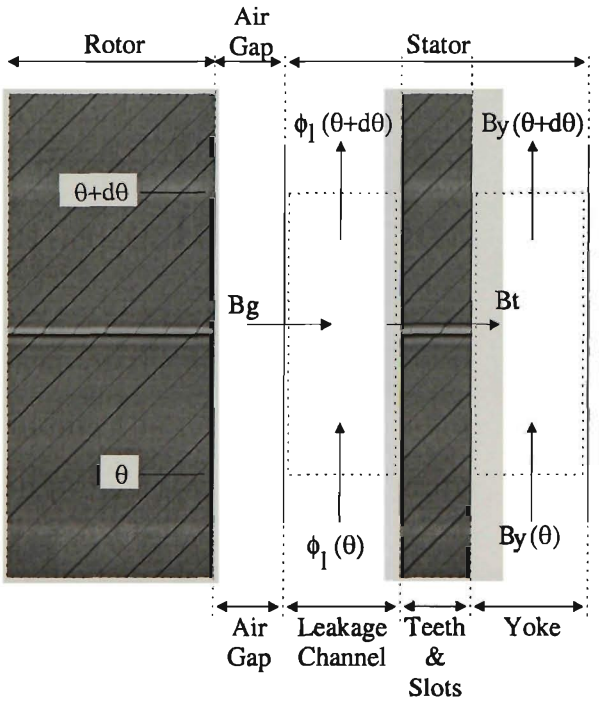

Figure 3.8: Stator Fluxes

As the flux in Figure 3.8 traverses from left to right, passage is made from

the rotor through the airgap, through the stator teeth and into the stator yoke. The airgap takes flux directly across it from the rotor with no MMF drop in the rotor. In between the airgap and the stator teeth we have defined a slot leakage channel which passes leakage flux in the direction shown. This channel runs around the circumference of the motor and the return path for leakage is through the stator yoke. An MMF drop is experienced by the leakage channel flux as it traverses the circumference of the motor. The teeth allow flux to pass from the leakage channel into the yoke with no MMF drop. Once the flux reaches the yoke it completes the closed loop path for the leakage flux. The leakage channel has a reluctance defined as $\Re_l$ A/Wb/m of airgap.

The value for $\Re_l$ can be found by utilising the known slot geometries. Finding an expression for the slot leakage reluctance first requires definition of the physical system that is being modelled. Figure 3.9 illustrates the basis of the modelling for this parameter.

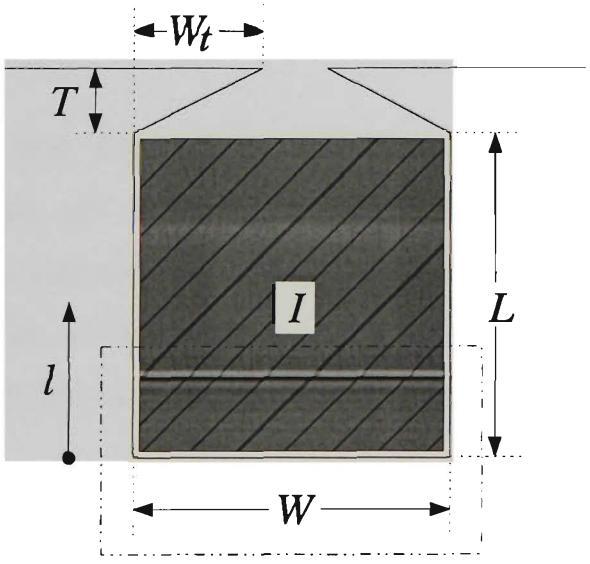

Figure 3.9: Slot Leakage Reluctance Model

The physical quantities are self explanatory, being the dimensions of the tooth slot. The variable l is used to express the incremental distance traversed from the base of the slot towards the top of the slot, but less than the height L. The block marked I represents the current density in the slot of the motor. The

expression for leakage reluctance is found by first determining an expression for the reluctance of the area enclosed in the section bounded by W and L. This quantity is referred to as $\Re_{l1}$. The detailed mathematics for the derivation of these expressions is given in Appendix C, Section C.3.

$$\Re_{l1} = \frac{2W}{\mu_o L_s L}. \tag{3.21}$$

A similar expression is required for the upper area of the slot; the trapezoidal shaped section. This quantity is referred to as $\Re_{l2}$.

$$\Re_{l2} = \frac{-2W_t}{\mu_o L_s T \left[\ln\left(1 - \frac{2W_T}{W}\right)\right]}. \tag{3.22}$$

Equation (3.22) is an expression for the reluctance of one slot/tooth pair in the stator. When combined with equation (3.21) as a parallel circuit, the complete expression for slot leakage reluctance as used in this analysis is found.

$$\Re_l = \left(\frac{1}{\Re_{l1}} + \frac{1}{\Re_{l2}}\right)^{-1} \tag{3.23}$$

It should be noted that Figure 3.8 is a microscopic model; it only looks at the incremental angle, $d\theta$. This enables the model to be defined by a set of simple differential equations. The compromise made for this simplification is that prediction of the slotting effects cannot be made, except in as much as they have been taken into account in calculating the q-axis reluctance by using Carter's coefficient.

3.6 General Solution for Yoke Flux

Considerable interest is placed on the formulation of an expression for the flux densities in the yoke. The yoke is the return path for all machine fluxes. If there is going to be an increase in the q-axis flux as a result of the zigzag effect, then this increase can be quantified by calculating the change in the value of the yoke

flux. If it is possible to find this value using a simple expression then comparison of the same value obtained from finite element analysis is more meaningful.

Finite element analysis produces a very complex series of results. If the model being used is complex, then the amount of information produced is potentially very high. In order to make sense of such a complex amount of information, the task is made easier if it is possible to concentrate on a section of the model. In this case, the region of interest is the yoke.

Working with the equations for flux and reluctance that have already been developed, an expression for the general solution of the yoke flux can be found. Consider a loop covering angle $d\theta$, enclosing the stator current, as shown in Figure 3.8.

$$JRd\theta\frac{1}{p} = \Re_l Rd\theta\frac{1}{p}\Phi_l \tag{3.24}$$

Where Φ_l is the flux in the slot leakage channel.

This simplifies to the expression

$$\Phi_l = \frac{J(\theta)}{\Re_l}. \tag{3.25}$$

Continuity of flux in the leakage channel leads to

$$B_g Rd\theta L_s\frac{1}{p} - B_t Rd\theta L_s\frac{1}{p} + \Phi_l(\theta) - \Phi_l(\theta + d\theta) = 0. \tag{3.26}$$

Expansion and simplification produces

$$\frac{d\Phi_l}{d\theta} = \frac{RL_s}{p}(B_g - B_t) \tag{3.27}$$

Now, consider the continuity of flux in the yoke of the machine.

$$B_t(\theta)Rd\theta L_s\frac{1}{p} + B_y(\theta)YL_s - B_y(\theta + d\theta)YL_s = 0 \tag{3.28}$$

Expansion and simplification leads to

$$\frac{dB_y}{d\theta} = \frac{R}{Yp} B_t(\theta) \tag{3.29}$$

Now it only remains to determine the pole side reluctance and incorporate it into the model. The all fluxes can be determined if the current distribution is known.

3.7 Pole Side Reluctance

The pole side reluctance represents the largest airgap in the q-axis flux path. Its effect is more prevalent in 2 pole motors, but essentially it has the effect of conducting q-axis flux past the pole sides of the motor. The effect is due to physical constraints in the manufacture of axially laminated rotors. The width of the rotor laminations toward the end of the pole face cannot be made too small because their mechanical strength is lost. As a consequence, there is usually a larger airgap where the rotor meets the stator in the q-axis path. Figure 3.10 illustrates this effect.

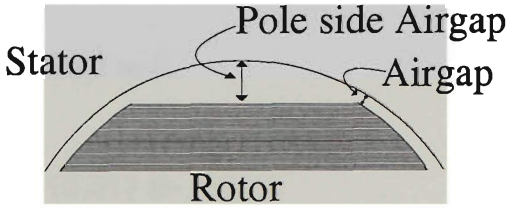

Figure 3.10: Pole Side Reluctance

The pole side airgap referred to in Figure 3.10 is not of constant length. In the analysis used here, the airgap value used was an average value. That is, the expression for the pole side reluctance is based on equation (3.6), with the gap value set to the average value for the pole side airgap. This reluctance is referred to as $\Re_{side}$ in the equations of this thesis.

3.8 Sinusoidal Current Distribution

Now that the basic equations for the flux distributions of the SyncRM have been established, alongside a variety of expressions for machine reluctances, it is possible to finalize these equations using a particular distribution of current in the stator.

3.8.1 The Q-Axis Flux

The first expression sought is that for the q-axis flux distribution. A standard motor will have a three phase distributed winding which can be approximated by a sinusoidal distribution of current. This distribution can then be reduced into d- and q-axis components. Sinusoidal current distribution is described by

$$J(\theta) = J_q \cos\theta - J_d \sin\theta. \tag{3.30}$$

Using this equation, a specific solution to equation (3.20) can be found. The mathematical details can be found in Appendix C, Section C.4.1.

For the given current distribution, equation (3.20) is written as

$$\frac{d^2\Phi_q}{d\theta^2} - b\Phi_q + 2cJ_q \cos\theta = 0. \tag{3.31}$$

The solution to equation (3.31) is

$$\Phi_q(\theta) = Ae^{\gamma\theta} + Be^{-\gamma\theta} + \frac{2cJ_q}{b+1}\cos\theta \tag{3.32}$$

The next step in the solution is determining values for the coefficients, A and B in equation (3.32). These values are determined in Appendix C, Section C.4.1. It turns out that only one of them appears in the final equation. Once this is obtained, the solution, equation (3.32), becomes

$$\Phi_q(\theta) = A(e^{\gamma\theta} + e^{-\gamma\theta}) + \frac{2cJ_q\cos\theta}{b+1} \tag{3.33}$$

At this stage, the next requirement is to find an expression for the constant A. There are two methods of approaching this problem. In the first instance the assumption that at $\theta = \frac{\theta_p}{2}$ $\Phi_q = 0$. This is the extremity of the pole. Ideally, the entire pole flux is contained wholly within the pole face. However, practically, this is not the case. Within the analysis provided here, the two cases are differentiated by the expressions, "Including Pole Side Flux" and "Neglecting Pole Side Flux".

Neglecting Pole Side Flux

In the case where $\Phi_q = 0$ at $\theta = \frac{\theta_p}{2}$, the value of A in Equation (3.33) is given by

$$A = \frac{-2cJ_q \cos\frac{\theta_p}{2}}{(b+1)(e^{\gamma\frac{\theta_p}{2}} + e^{-\gamma\frac{\theta_p}{2}})} \tag{3.34}$$

Including Pole Side Flux

In the case that flux is not wholly contained within the pole-face, a different set of equations are used. Firstly, consider an MMF equation of the q-axis as described in Figure 3.11.

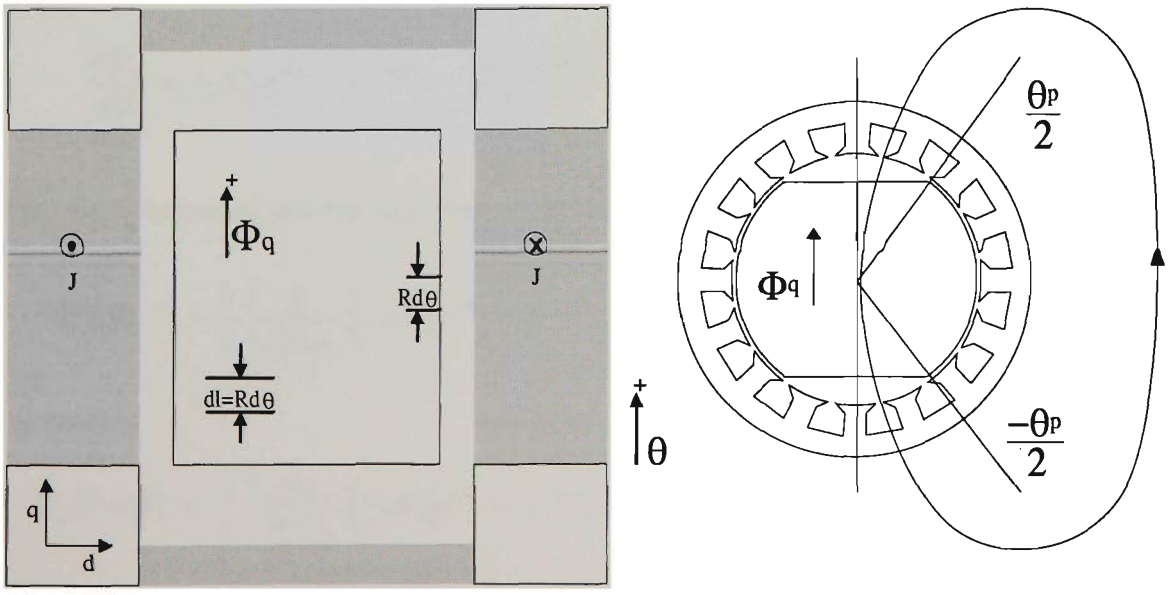

Figure 3.11: Alternate Machine Model

The total MMF enclosed by the loop which passes all the way along the q-axis and returns via the yoke, is given by the expression

$$MMF = \int_{\frac{-\theta_p}{2}}^{\frac{\theta_p}{2}} H_q R \frac{d\theta}{p} + 2\Phi_q \left(\frac{\theta_p}{2}\right) \Re_{side} \tag{3.35}$$

Further analysis leads to the final result. This analysis is presented in Appendix C, Section C.4.1.

$$A = \frac{\gamma}{b+1} \frac{RJ_q(b+1) - 2cJ_q \left[\Re_q R \sin\frac{\theta_p}{2} + p\Re_{side} \cos\frac{\theta_p}{2}\right]}{\Re_q R(e^{\gamma\frac{\theta_p}{2}} - e^{-\gamma\frac{\theta_p}{2}}) + p\gamma\Re_{side}(e^{\gamma\frac{\theta_p}{2}} + e^{-\gamma\frac{\theta_p}{2}})} \tag{3.36}$$

If in equation (3.36), $\Re_{side} \to \infty$, then the expression for A becomes the same as that previously derived and given by equation (3.34).

3.8.2 The Airgap Flux Density

In the process of finding expressions for the q-axis flux, several other relationships were determined which are useful results. They include expressions for the airgap flux densities. These were presented as equations C.34 and C.35 in Appendix C. Given that the result for $\frac{d\Phi_q}{d\theta}$ is now known, these expressions can be further developed. Recall the equation for $\Phi_q(\theta)$ given by equation (3.33). Thus,

$$\frac{d\Phi_q}{d\theta} = \gamma A \left(e^{\gamma\theta} - e^{-\gamma\theta}\right) - \frac{2cJ_q \sin\theta}{b+1} \tag{3.37}$$

The final expressions for the airgap flux density now become;

$$B_g(\theta) = -\frac{1}{2}\left[\frac{p}{RL_R}\left(\gamma A \left(e^{\gamma\theta} - e^{-\gamma\theta}\right) - \frac{2cJ_q \sin\theta}{\Re_q(b+1)}\right) + \frac{2\mu_o RJ_d \cos\theta}{pg_e}\right] \tag{3.38}$$

$$B_g(\pi-\theta) = \frac{1}{2}\left[\frac{p}{RL_R}\left(\gamma A \left(e^{\gamma\theta} - e^{-\gamma\theta}\right) - \frac{2cJ_q \sin\theta}{\Re_q(b+1)}\right) + \frac{2\mu_o RJ_d \cos\theta}{pg_e}\right] \tag{3.39}$$

3.8.3 Tooth and Yoke Flux Density

Two more important expressions are those for tooth and yoke flux densities. In particular, the yoke flux density is of interest since it can be used to compare the results of the analytical work with that of finite element analysis.

Section 3.6 presented the general expressions required to determine yoke flux relationships. The main results to note are equations (3.25), (3.27) and (3.29). Along with the equations of airgap flux densities just presented, solutions to the section 3.6 results can be found.

If the expression for current distribution, equation (3.30), is substituted into equation (3.25), and equations (3.27) and (3.38) used, the complete expression for $B_t(\theta)$ can be written. The full working for this process is given in Appendix C, Section C.4.2.

$$B_t(\theta) = -\frac{1}{2}\left[\frac{p}{RL_R}\left(\gamma A\left(e^{\gamma\theta} - e^{-\gamma\theta}\right) - \frac{2cJ_q\sin\theta}{b+1}\right) + \frac{2\mu_o R J_d \cos\theta}{pg_e}\right] + \frac{p(J_q\sin\theta - J_d\cos\theta)}{\Re_l RL_s} \tag{3.40}$$

Using the relationship (derived from equation (3.29))

$$B_y(\theta) = \frac{R}{pY}\int B_t(\theta)d\theta \tag{3.41}$$

an expression for yoke flux density can be obtained. However, the solution to the integral yields a constant of integration. Since the d- and q-axes have different boundary conditions, the two cases are considered separately.

$$B_{tq}(\theta) = -\frac{1}{2}\left[\frac{p}{RL_R}\left(\gamma A\left(e^{\gamma\theta} - e^{-\gamma\theta}\right) - \frac{2cJ_q\sin\theta}{b+1}\right)\right] + \frac{pJ_q\sin\theta}{\Re_l RL_s} \tag{3.42}$$

If it is assumed L_s and L_R are the same and equation (3.42) is substituted into equation (3.41) and the integral solved, the following results;

$$B_{yq}(\theta) = -\frac{1}{2YL_R}\left[A\left(e^{\gamma\theta} + e^{-\gamma\theta}\right) + \frac{2cJ_q\cos\theta}{b+1} - \frac{J_q\cos\theta}{\Re_l}\right] + const \quad (3.43)$$

To solve for "*const*", there are two sets of boundary conditions to be used, as was the case for q-axis flux; $B_{yq} = 0$ at $\theta = \frac{\theta_p}{2}$ and $B_{yq} = 0$ at $\theta = \frac{\pi}{2}$. These boundary conditions represent the no pole side flux and pole side flux cases.

Neglecting Pole Side Flux

$$B_{yq}(\theta) = -\frac{1}{2YL_R}\left[A\left(e^{\gamma\theta} + e^{-\gamma\theta}\right) + \frac{2cJ_q\cos\theta}{b+1} - \frac{J_q\sin\theta}{\Re_l} - A\left(e^{\gamma\frac{\theta_p}{2}} + e^{-\gamma\frac{\theta_p}{2}}\right) - \frac{2cJ_q\cos\frac{\theta_p}{2}}{b+1} + \frac{J_q\cos\frac{\theta_p}{2}}{\Re_l}\right] \quad (3.44)$$

Including Pole Side Flux

$$B_{yq}(\theta) = -\frac{1}{2YL_R}\left[A\left(e^{\gamma\theta} + e^{-\gamma\theta}\right) + \frac{2cJ_q\cos\theta}{b+1} - \frac{J_q\sin\theta}{\Re_l} - A\left(e^{\gamma\frac{\theta_p}{2}} + e^{-\gamma\frac{\theta_p}{2}}\right)\right] \quad (3.45)$$

Now, for the d-axis

$$B_{td}(\theta) = \frac{-\mu_o RJ_d\cos\theta}{pg_e} - \frac{pJ_d\cos\theta}{\Re_l RL_s} \quad (3.46)$$

As before, equation (3.46) is substituted in equation (3.41) and the integral solved.

$$B_{yd}(\theta) = \frac{R}{pY}\left[\frac{-\mu_o RJ_d\sin\theta}{pg_e} - \frac{pJ_d\sin\theta}{\Re_l RL_s}\right] + const \quad (3.47)$$

If the initial condition, $B_{yd} = 0$ at $\theta = 0$, is applied, and expression for B_{yd} is

obtained.

$$B_{yd}(\theta) = \frac{R}{pY}\left[\frac{-\mu_o R J_d \sin\theta}{p g_e} - \frac{p J_d \sin\theta}{\Re_l R L_s}\right] \tag{3.48}$$

3.9 Rectangular Current Distribution

3.9.1 The Q-axis Flux

In the previous section, the expressions for a variety of machine fluxes and flux densities were presented based on the sinusoidal distribution of current in the stator of the machine. In this section, a similar analysis is presented, except that the current distribution is rectangular, or of a block fashion. That is, it is a constant value, independent of stator position.

In this case, $J_q(\theta) = J_q$, a constant. Since the interest lies primarily in the q-axis flux, J_d can be assumed to be 0. Since J_q is no longer a function of θ, but rather a constant, then equation (3.20) can be re-written as

$$\frac{d^2\Phi_q(\theta)}{d\theta^2} - b\Phi_q(\theta) + 2cJ_q = 0 \tag{3.49}$$

In this case, J_q is simply some constant value with the units amperes/metre. As was for the sinusoidal case, this equation can be solved using the method of undetermined coefficients. The solution is given by

$$\Phi_q(\theta) = Ae^{\gamma\theta} + Be^{-\gamma\theta} + \frac{2cJ_q}{b} \tag{3.50}$$

The next step requires the values for the constants A and B to be determined. This cannot be performed directly. Firstly, the relationship between these constants must be examined. In order to do so, the expressions for airgap flux density need to be investigated. The details of this analysis are presented in Appendix C, Section C.5.1.

The solution to equation (3.50) becomes

$$\Phi_q(\theta) = A\left(e^{\gamma\theta} + e^{-\gamma\theta}\right) + \frac{2cJ_q}{b} \tag{3.51}$$

Just as for the sinusoidal case, there are 2 cases to solve in order to determine the expression for A.

Neglecting Pole Side Flux

Based on the boundary conditions of $\Phi_q = 0$ at $\theta = \frac{\theta_p}{2}$, the value of A in equation (3.51) is given by

$$A = \frac{-2cJ_q}{b\left(e^{\gamma\frac{\theta_p}{2}} + e^{-\gamma\frac{\theta_p}{2}}\right)} \tag{3.52}$$

Including Pole Side Flux

Once again, this is the case when it is assumed that not all the flux is contained wholly within the extremes of the pole face. Figure 3.11 is still valid and is the basis for the modelling used. For the rectangular current distribution, however, the total MMF enclosed by the loop described in this figure is given by $\frac{J_q R\theta_p}{p}$. Thus the expression to be dealt with is;

$$\frac{J_q R\theta_p}{p} = \int_{-\frac{\theta_p}{2}}^{\frac{\theta_p}{2}} \Phi_q \Re_q R \frac{d\theta}{p} + 2\Phi_q\left(\frac{\theta_p}{2}\right)\Re_{side} \tag{3.53}$$

Further analysis leads to the final result,

$$A = \frac{\gamma}{2b}\frac{bJ_q R\theta_p - 4pcJ_q\Re_{side}}{\Re_q R\left(e^{\gamma\frac{\theta_p}{2}} - e^{-\gamma\frac{\theta_p}{2}}\right) + p\gamma\Re_{side}\left(e^{\gamma\frac{\theta_p}{2}} + e^{-\gamma\frac{\theta_p}{2}}\right)} \tag{3.54}$$

As an aside, if in equation (3.54), $\Re_{side} \to \infty$, the the expression for A reverts to the value previously calculated, equation (3.52).

3.9.2 The Airgap Flux Density

In the process of finding the result of equation (3.49), several other relationships were discovered. They include a general expression for the airgap flux densities. These were presented as equations C.68 and C.69 in Appendix C. Since the expression for Φ_q has now been determined, the equations for the airgap flux densities can be completed. The expression for $\Phi_q(\theta)$ is given by equation (3.51) and so;

$$\frac{d\Phi_q}{d\theta} = \gamma A \left(e^{\gamma\theta} - e^{-\gamma\theta}\right) \tag{3.55}$$

Thus;

$$B_g(\theta) = -\frac{1}{2}\left[\frac{p\gamma A}{RL_R}\left(e^{\gamma\theta} - e^{-\gamma\theta}\right) - \frac{\mu_o R J_d}{p g_e}(\pi - \theta_p)\right] \tag{3.56}$$

$$B_g(\pi - \theta) = \frac{1}{2}\left[\frac{p\gamma A}{RL_R}\left(e^{\gamma\theta} - e^{-\gamma\theta}\right) + \frac{\mu_o R J_d}{p g_e}(\pi - \theta_p)\right] \tag{3.57}$$

3.9.3 Tooth and Yoke Flux Densities

Previously, section 3.6 presented the general expression for the tooth and yoke flux densities. To solve for the particular case of rectangular current, then use the expression for the stator current. In this case, $J_q(\theta) = J_q$, a constant. From equation (3.25),

$$\Phi_l = \frac{J_q}{\Re_l} = constant \tag{3.58}$$

From equation (3.27)

$$\frac{RL_s}{p} = (B_g - B_t) = 0 \tag{3.59}$$

Therefore, $B_g = B_t$.

The previous section already presented the results for $B_g(\theta)$. They were given in equations (3.56) and (3.57). The tooth and yoke fluxes are made up of d- and q-axes components;

$$B_{tq}(\theta) = -\frac{p\gamma A\left(e^{\gamma\theta} - e^{-\gamma\theta}\right)}{2RL_R}$$
$$B_{tq}(\pi - \theta) = \frac{p\gamma A\left(e^{\gamma\theta} - e^{-\gamma\theta}\right)}{2RL_R}$$
$$B_{td}(\theta) = B_{td}(\pi - \theta) = \frac{\mu_o R J_d(\pi - \theta_p)}{2pg_e}$$

Consider the q-axis case first. From equation (3.29), the following can be written;

$$B_{yq}(\theta) = \frac{R}{pY}\int B_{tq}(\theta)d\theta \tag{3.60}$$

Which, upon doing the integration, becomes;

$$B_{yq}(\theta) = \frac{A}{2YL_R}\left(e^{\gamma\theta} + e^{-\gamma\theta}\right) + const \tag{3.61}$$

To solve for "*const*", there are two sets of boundary conditions to be used, as was the case for q-axis flux; $B_{yq} = 0$ at $\theta = \frac{\theta_p}{2}$ and $B_{yq} = 0$ at $\theta = \frac{\pi}{2}$. These boundary conditions represent the cases of no pole side flux and pole side flux.

Neglecting Pole Side Flux

$$const = -\frac{A}{2YL_R}\left(e^{\gamma\frac{\theta_p}{2}} + e^{-\gamma\frac{\theta_p}{2}}\right) \tag{3.62}$$

Accordingly;

$$B_{yq}(\theta) = \frac{A}{2YL_R}\left[e^{\gamma\theta} + e^{-\gamma\theta} - e^{\gamma\frac{\theta_p}{2}} - e^{-\gamma\frac{\theta_p}{2}}\right] \tag{3.63}$$

Including Pole Side Flux

$$B_{yq}(\theta) = \frac{A}{2YL_R}\left[e^{\gamma\theta} + e^{-\gamma\theta} - e^{\gamma\frac{\pi}{2}} - e^{-\gamma\frac{\pi}{2}}\right] \tag{3.64}$$

At this point, the d-axis needs to be considered. Once again, using equation (3.29), it can be written;

$$B_{yd}(\theta) = B_{yd}(\pi - \theta) = \frac{R}{pY}\int B_{td}d\theta \tag{3.65}$$

If the boundary condition $B_y = 0$ at $\theta = 0$ and $\theta = \pi$ is used, then;

$$B_{yd}(\theta) = \frac{\mu_o R^2 J_d(\pi - \theta_p)\theta}{2p^2 Y g_e} \tag{3.66}$$

$$B_{yd}(\pi - \theta) = \frac{\mu_o R^2 J_d(\pi - \theta_p)(\pi - \theta)}{2p^2 Y g_e} \tag{3.67}$$

3.10 Model Studies

This Chapter has presented a number of expressions dealing with the various reluctances, fluxes and flux densities associated with the synchronous reluctance machine. Using the motor described in Appendix B, this section presents a series of sample results from the equations presented in this Chapter. The results presented include values for the q-channel reluctance, q-axis flux and airgap flux densities for both sinusoidal and rectangular current distributions.

3.10.1 Q-Axis Reluctance

The method required for calculating the q-axis channel reluctance is straight forward. There are a series of physical parameters that need to be calculated and then it is possible to come up with a value for the reluctance being sought, $\Re_q$. This method is described in Section 3.3.

1. Using equation (3.9), the slot pitch, l_{sp}, is calculated as $10.84 \times 10^{-3}m$.

2. Using equation (3.7), the tooth face surface area, A_s, is calculated as $250 \times 10^{-6}m^2$.

3. Using equation (3.11), the integral average cross sectional area of the rotor, A_{rl}, is calculate as $2.975 \times 10^{-3}m^2$.

4. The effective airgap, g_e, taking into account the slotting of both the rotor and the stator is calculated as $466.7 \times 10^{-6}m$.

5. The reluctances $\Re_{G1}$, $\Re_{G2}$ and $\Re_R$ are calculated as 5942209, 1980736 and 724890 A/Wb respectively.

6. Finally, $\Re_{eq}$, the q-channel reluctance is calculated and normalised to 61266359 $A/Wb/m$.

It is also possible to calculate a simple value for the d-axis reluctance. If it assumed that the reluctance through the d-axis of the rotor body is negligible, then the calculation can be made as follows.

1. The arc-length of the pole face is calculated using

$$l_{poleface} = R_R\theta_p \tag{3.68}$$

   This gives rise to the value $l_{poleface} = 108.38 \times 10^{-3}m$.

2. The d-axis reluctance is calculated using

$$\Re_d = \frac{2g_e}{\mu_o A} \tag{3.69}$$

   This gives rise to the value of $\Re_d = 92444\ A/Wb$. Note that the units for this expression of reluctance is different that that used for $\Re_q$. It means that to compare $\Re_d$ with $\Re_q$, the latter needs to be converted to a comparable system of units. To do this, the step of normalisation is avoided. This gives a value of $\Re_q = 664127\ A/Wb$.

3. The Saliency Ratio can now be calculated using the equation

$$\xi = \frac{\Re_q}{\Re_d} \tag{3.70}$$

Using this equation, the value of the saliency ratio for this motor is given by $\xi = 7.18$.

3.10.2 Q-Axis Flux

Graphical representations of the q-axis flux can be made. Equations 3.33 and 3.51 are expressions that describe the flux in the "q-channel" of the rotor. By changing the value of θ in these equations, it is possible to visualise this flux. When the pole side effect is excluded, then the valid range for θ is $-\frac{\theta_p}{2}$ to $\frac{\theta_p}{2}$. Inclusion of the pole side effect extends the range for θ to $-\frac{\pi}{2}$ to $\frac{\pi}{2}$.

The expected result would be a distribution that is a minimum at the extremes of the q-channel and a maximum at the centre. It should closely match the flux distribution one would expect in the yoke of the Synchronous Reluctance Motor.

Sinusoidal Distribution

Using Equations 3.33, 3.34 and 3.36 a plot of Pole Arc Angle vs Q-Axis Flux can be obtained and is illustrated in Figure 3.12. The current distribution is given by Equation 3.30. The current distribution is given by $J_q = 4000A/m$ and since the key area of interest is the q-axis, the current density in the d-axis is $J_d = 0$. It is interesting to note that the values of flux at the extremities of the pole are higher with the inclusion of the pole side flux term. This is the expected result. The no pole side flux case assumes that the flux is wholly contained within the limit of the pole face. Hence, it is expected that the value of the flux at the extremes of the pole should be zero, as it is in Figure 3.12.

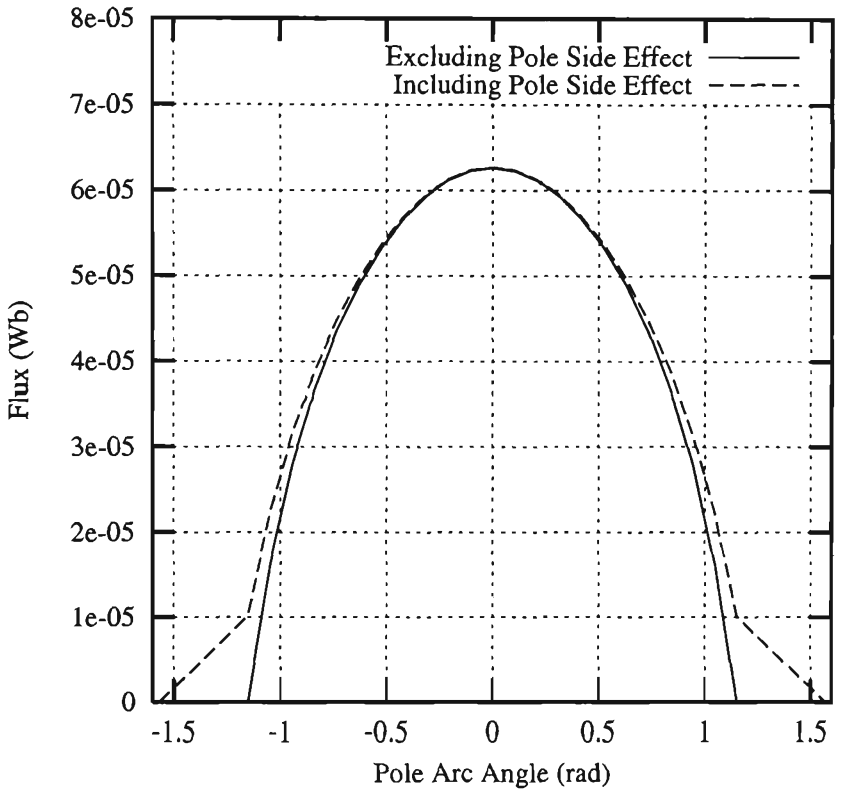

Figure 3.12: Pole Arc Angle vs Q-Axis Flux, Sinusoidal Current Distribution

The linearisation of the flux distribution at the pole ends is a result of the assumption that the pole side can be modelled as a reluctance using a fixed airgap. In practice, the distribution would be different than this and would depend on the geometry of the rotor design.

Rectangular Distribution

Using Equations 3.51, 3.52 and 3.54, a plot of Pole Arc Angle vs Q-Axis Flux can be obtained and is illustrated in Figure 3.13. The current distribution is $J_q = 4000\ A/m$ and $J_d = 0$. The interesting feature of this graph is the squared nature of the flux distribution. This is to be expected with the current distribution used. The overall level of flux in the q-axis is higher compared to that for sinusoidally distributed current. For the same level of current density, the overall flux level in the machine is much higher. In (Coates et al., 1997), the authors show how this effect can be utilised to optimise the torque production in the SyncRM.

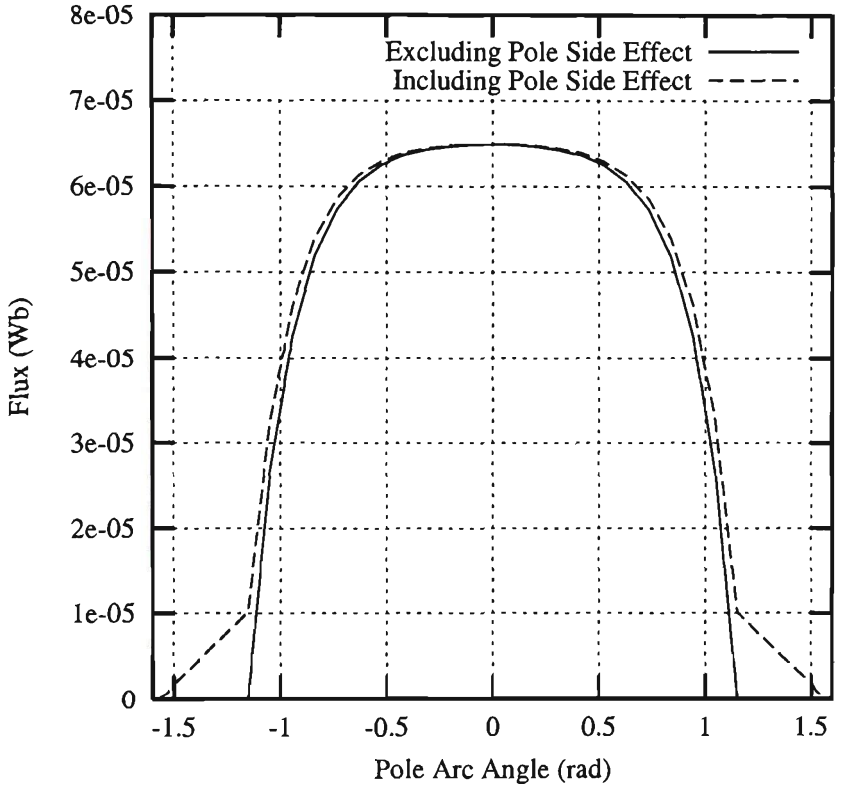

Figure 3.13: Pole Arc Angle vs Q-Axis Flux, Rectangular Current Distribution

3.10.3 Flux Densities

The analysis produced expressions for the airgap flux density distribution. These expressions were derived as part of finding the solution for the q-axis flux. They relate the value of the flux density in the airgap to the pole arc angle.

Sinusoidal Distribution

Using Equation 3.38, the plot illustrated in Figure 3.14 is obtained. The "mirror" value of Equation 3.38, Equation 3.39, is not plotted here. It is the same shape but reversed. That is, instead of sweeping from maximum positive to maximum negative as the pole arc is traversed from $-\theta_p$ to θ_p, the plot would be maximum negative to maximum positive.

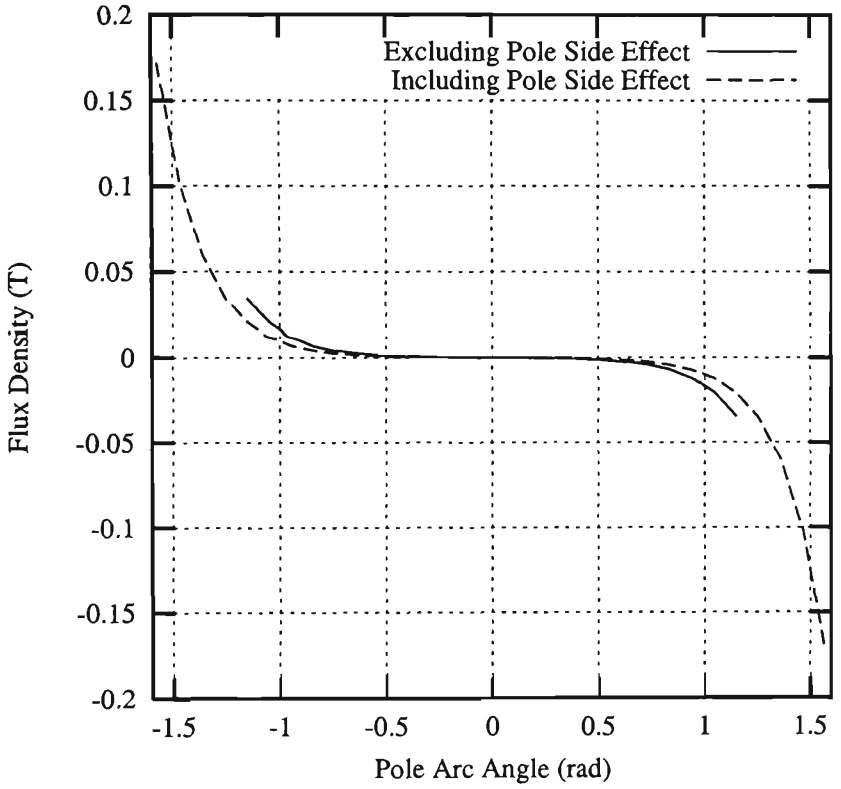

Figure 3.14: Airgap Flux Density vs Arc Pole Angle, Sinusoidal Current Distribution

Rectangular Distribution

Using Equation 3.56, the plot illustrated in Figure 3.15 is obtained. It is similar to that obtained for a sinusoidal current distribution, except that the flux density levels are higher as expected.

3.11 Conclusions

The greatest difficulty with previous analytical models was the inadequacy of the q-axis modelling. One of the reasons why this modelling was incomplete was the omission of the zigzag effect that has been introduced in this Chapter. In (Staton et al., 1993) much work was performed in determining the optimum number of laminations required in an axially laminated rotor in order to maximise the saliency ratio. However, whilst increasing the number of laminations

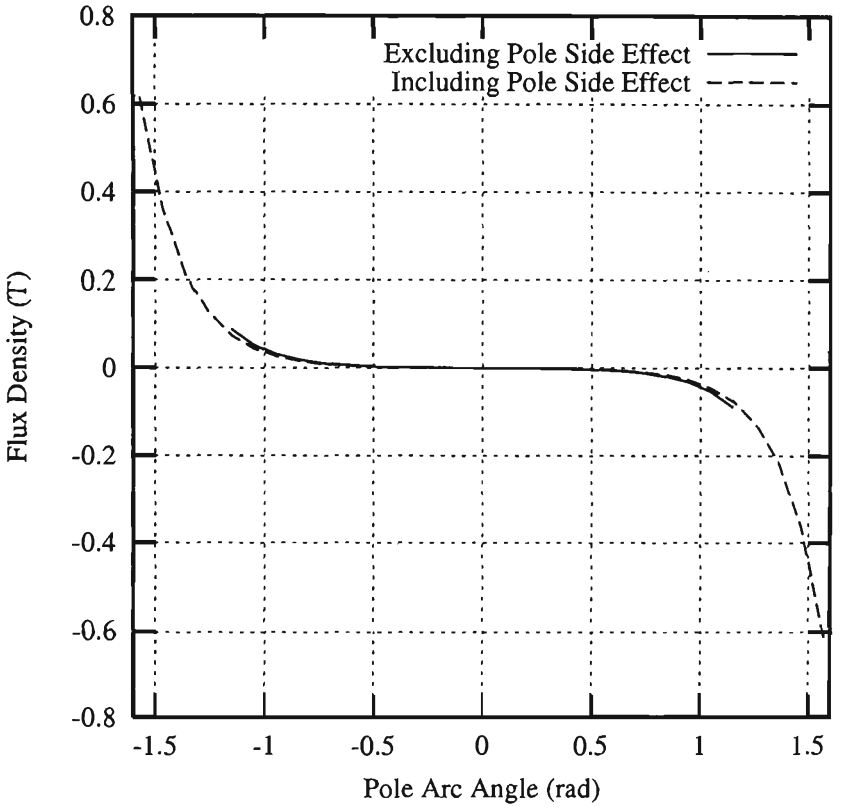

Figure 3.15: Airgap Flux Density vs Pole Arc Angle, Rectangular Current Distribution

has the desired effect of reducing torque ripple, if the number is increased such that the thickness of the rotor lamination is of the order of 10% of the stator tooth, then the saliency ratio will be reduced as a direct result of these zigzag flux paths. This has a further negative impact upon calculations involving efficiency and power factor for example.

The results from the work presented in this Chapter indicate that there is a point beyond which the gains made by using thinner laminations are diminished and in fact a reduction in saliency will occur. There should be an optimal value for the thickness of the lamination.

The introduction of an expression for the q-channel reluctance is important since it relates the physical dimensions of the synchronous reluctance motor to the q-axis inductance. The calculation of the q-channel reluctance enables the development of expressions for the flux distribution in the airgap of the motor. Whilst these expressions do not predict the variations in airgap flux due to

zigzag effects, they do include the average effect on the overall fluxing of the motor.

This Chapter represents a significant improvement in the modelling of the q-axis of the SyncRM by introducing concepts that have been neglected in previous research.

Chapter 4

Finite Element Modelling

4.1 Introduction

In the previous Chapter, equations were derived that could estimate the values of flux and flux densities in various parts of the machine. One of the aims of that Chapter was to produce such expressions because they are simpler and easier to manipulate. It is the aim of the Finite Element (FE) modelling to validate the analytical equations.

This Chapter compares the results of the work from the chapter on Magnetic Circuit Modelling with that of a Finite Element Model. It presents results from finite element analysis of a Synchronous Reluctance Motor that supports the modelling work and confirms the existence of the zigzag flux. Both aspects of the existence are important. The zigzag flux concept is important for the modelling, in particular the calculation of the q-axis reluctance.

4.2 The Finite Element Model

The aim of this Chapter is to compare the results from the analytical modelling with that from a FE model. It is not the intention of this Chapter to provide

a detailed representation of the FE work, but rather a broad overview relevant to the goals of the Chapter. The motor chosen to perform the analysis on is a two pole device. The rotor is an axially laminated one, made up of laminations that are 0.5 mm in thickness. A standard design of interleaved magnetic and non-magnetic laminations are used. The effect of the rotor shaft is neglected. The stator is a standard squirrel cage induction motor design and it has 24 slots. Normally, due to symmetry, only $\frac{1}{4}$ of the machine need be modelled. Since the rotor is to be misaligned slightly in order to observe the zigzag effect, the entire machine is modelled. This leads to a finite element model with a considerable number of elements. Whilst this is not a problem as far as the modelling process is concerned, it is difficult to present the data in such a way that the results are clear rather than confused. For example, contour plots created with the large number of elements that the model has appears crowded. Instead of presenting plots of the entire machine, results from sections of interest are produced instead.

In order to gain some appreciation of the complexity of the finite element model used, consider Figures 4.1 and 4.2. Figure 4.1 presents the stator model alone whilst Figure 4.2 presents the rotor.

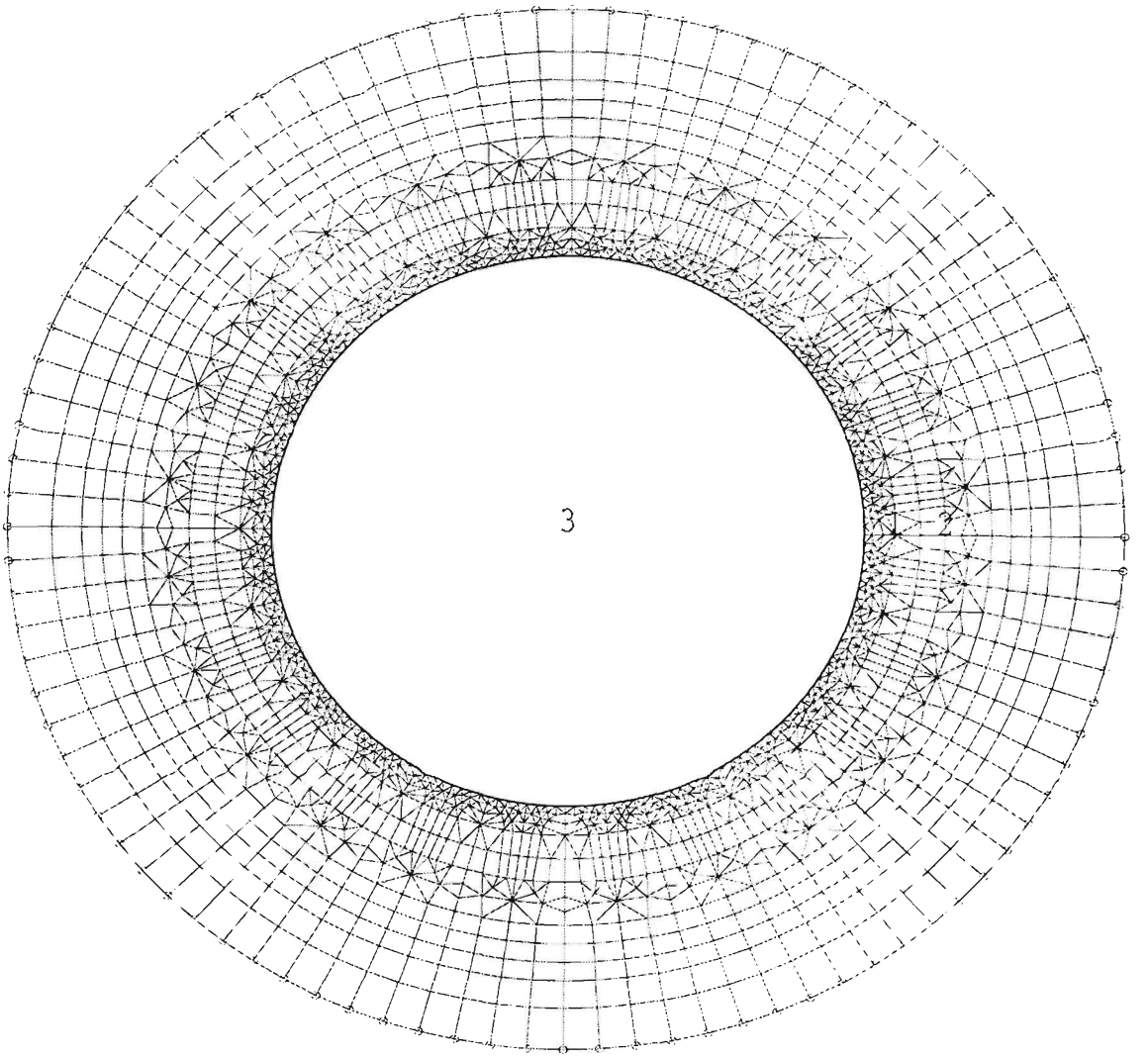

Figure 4.1: FEM Model Stator

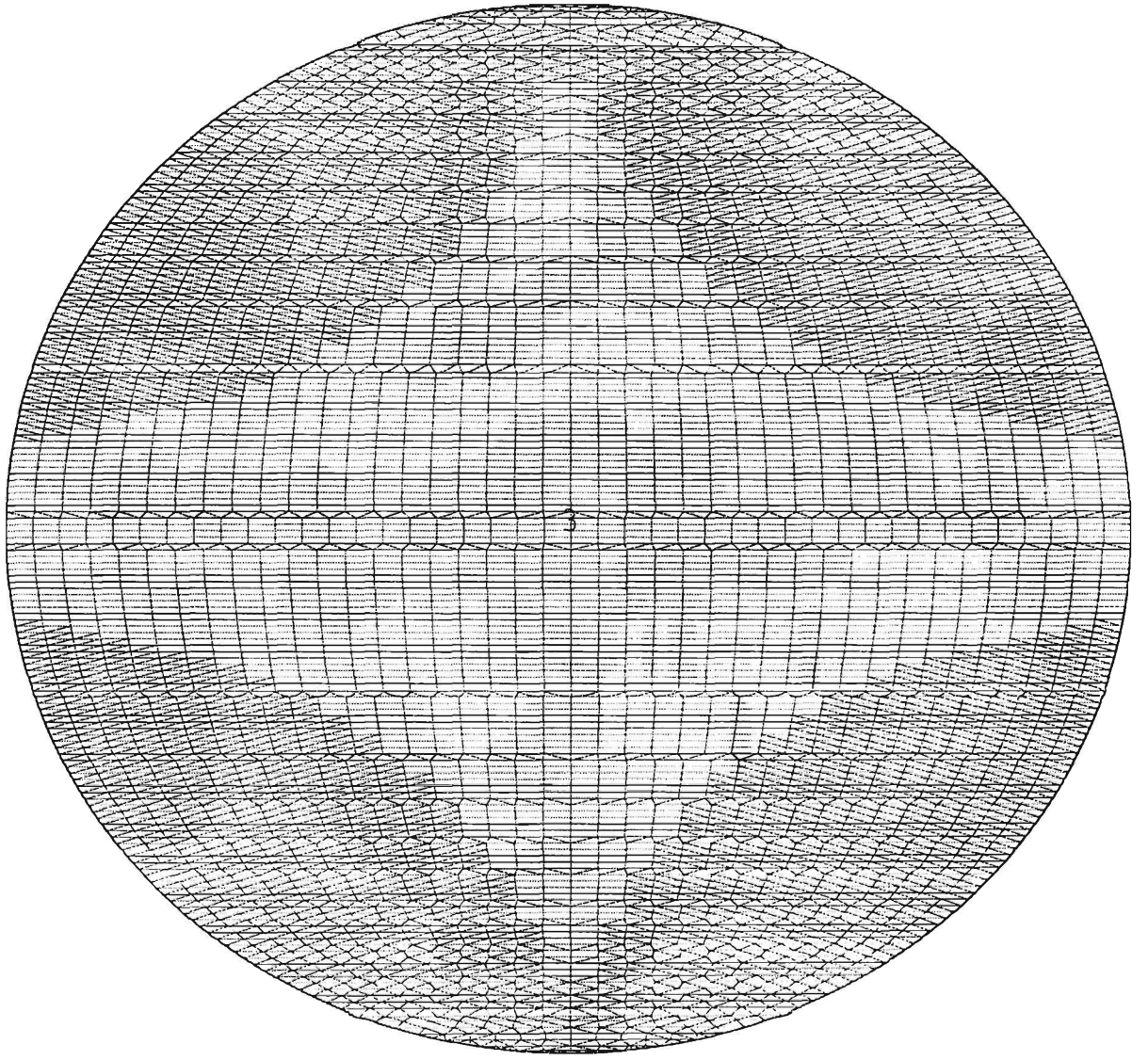

Figure 4.2: FEM Model Rotor

The rotor consists of a large number of laminations and elements. The thin rotor laminations are essential in observing the zigzag effect. The analysis of the model requires the placement of the current sources in the stator of the design. This current is the current that is responsible for driving the MMF's of the machine. The current is placed inside the slots of the stator.

A full physical description of the motor being modelled is presented in Appendix B.

4.3 Zigzag Flux Existence

Consider how the zigzag flux phenomenon might be observed. Previously, the zigzag flux has been described as a flux which has a path that "winds" its way through the laminations of the rotor. If this is the case, then one of the best places the zigzag flux could be observed would be in the rotor itself. The phenomenon should have the effect of decreasing the q-axis reluctance, leading to an increase in the amount of q-axis flux in the stator yoke. Since the yoke is the return path for the q-axis flux, any change in the q-axis flux value will be observed in the yoke back iron. Therefore, the best place to observe the effect would be along the q-axis of the rotor and the best place to measure the effect would be in the stator yoke.

In the earlier work, the existence of the zigzag flux was said to depend on two factors; the thickness of the rotor laminations and the relative position of the rotor with respect to the stator. In this first instance, consider the rotor in the "neutral" position. Previously, this position was described as "Slots Exactly Aligned" in Figure 3.2 in Chapter 3.

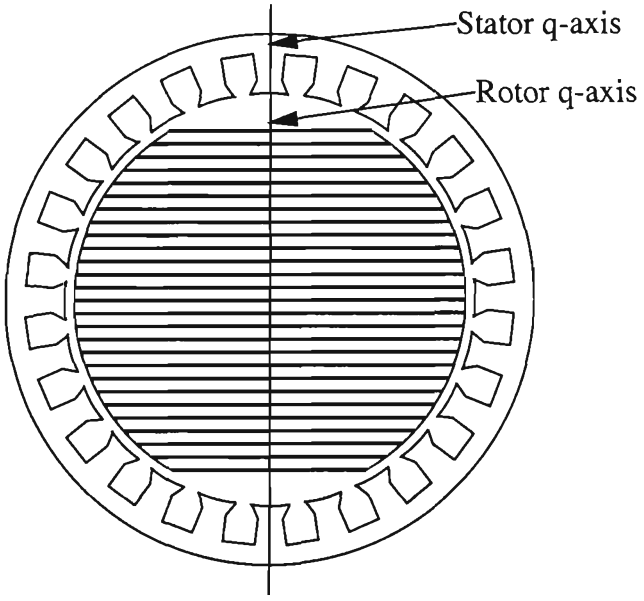

Figure 4.3: Rotor-Stator Aligned

With this alignment, the zigzag flux should be at its minimum. To visualise the effect, observe the flux vector normal to the q-axis. Ordinarily, this would be the place to view the d-axis flux. Under such aligned circumstances and with no d-axis excitation applied, little or no d-axis flux should be observed. The modelling also predicts little or no zigzag flux. Figure 4.4 illustrates how the flux vector is observed.

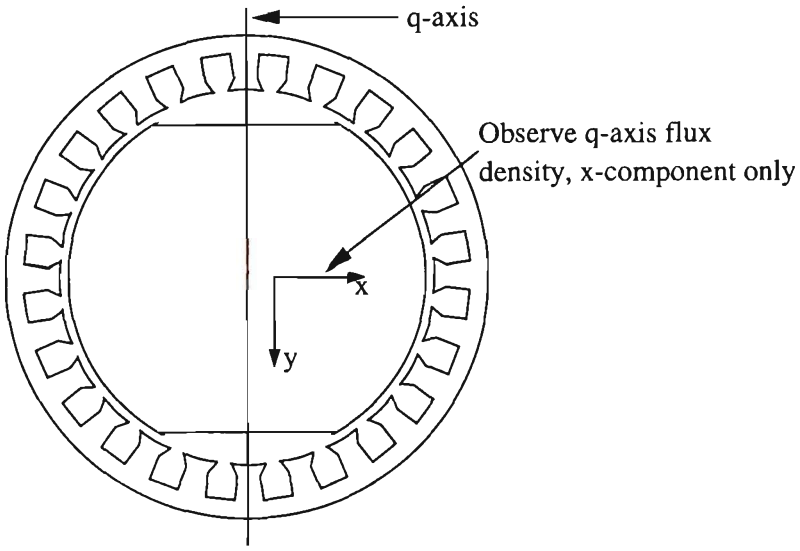

Figure 4.4: Zigzag Flux Observation

The low levels of flux in this direction are shown in Figure 4.5 which is a plot of the x-component of the rotor flux density vector along a path traversing the rotor q-axis. In this case, the excitation is equivalent to 4000 A/m of airgap, distributed as a rectangular block in the stator. Since the effect that is being sought is associated with the q-axis, then the excitation is applied only in the q-axis. In Chapter 3 the current densities were referred to as J_q and J_d. With respect to this nomenclature, the excitation used in the FE analysis is equivalent to $J_q = 4000$ and $J_d = 0$. The observed flux density is of the order of $10^{-6} Wb/m^2$.

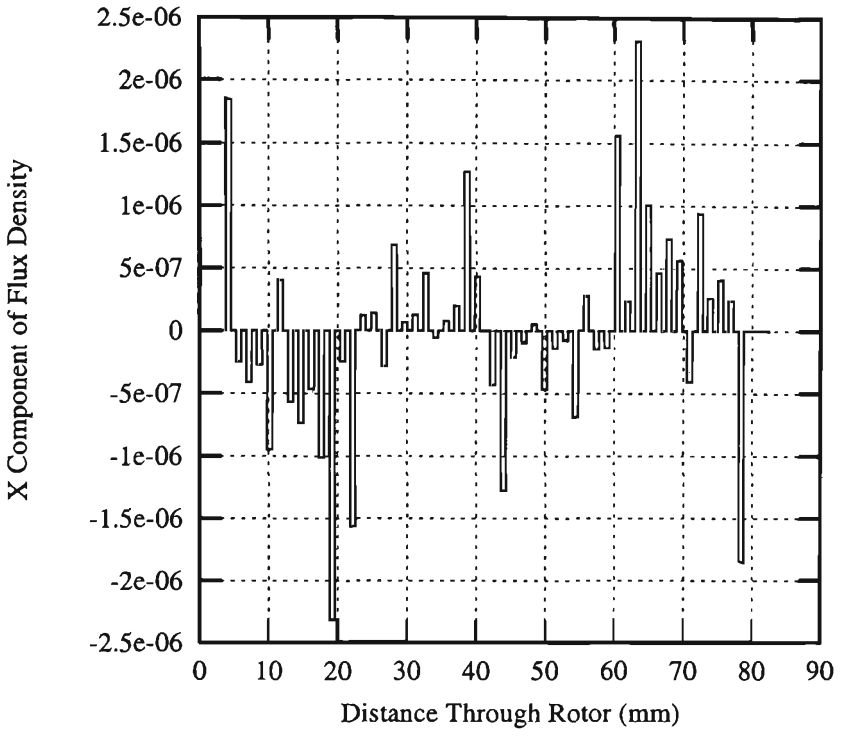

Figure 4.5: Zigzag Flux Phenomenon, Stator Teeth Aligned

This is the predicted result. Now consider the case where the rotor of the machine is rotated 3.75°counterclockwise. This is equivalent to $\frac{1}{4}$ of the slot pitch.

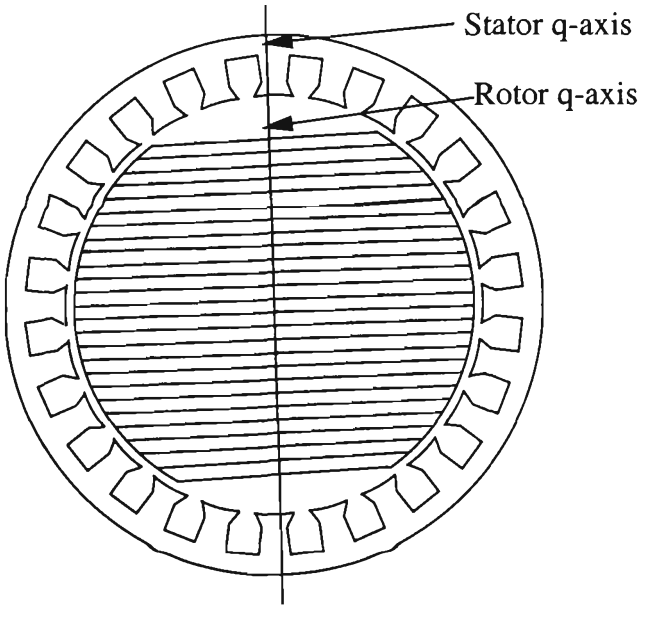

Figure 4.6: Rotor-Stator Misaligned

The placement of the current in the stator is also shifted by $\frac{1}{4}$ of a slot pitch, hence the shift in the stator q-axis. The shifted rotor alignment was described as "Slots Half Misaligned" in Figure 3.2 in Chapter 3. With the rotor half misaligned and only q-axis excitation being applied, there will be some d-axis flux. This is to be expected. Indeed, observation of the flux vectors normal to the q-axis reveals a trace which clearly shows the zigzagging nature of the flux in this region. Once again, an excitation current of 4000 A/m, distributed as a rectangular block, was used. This is equivalent to $J_q = 4000$ and $J_d = 0$.

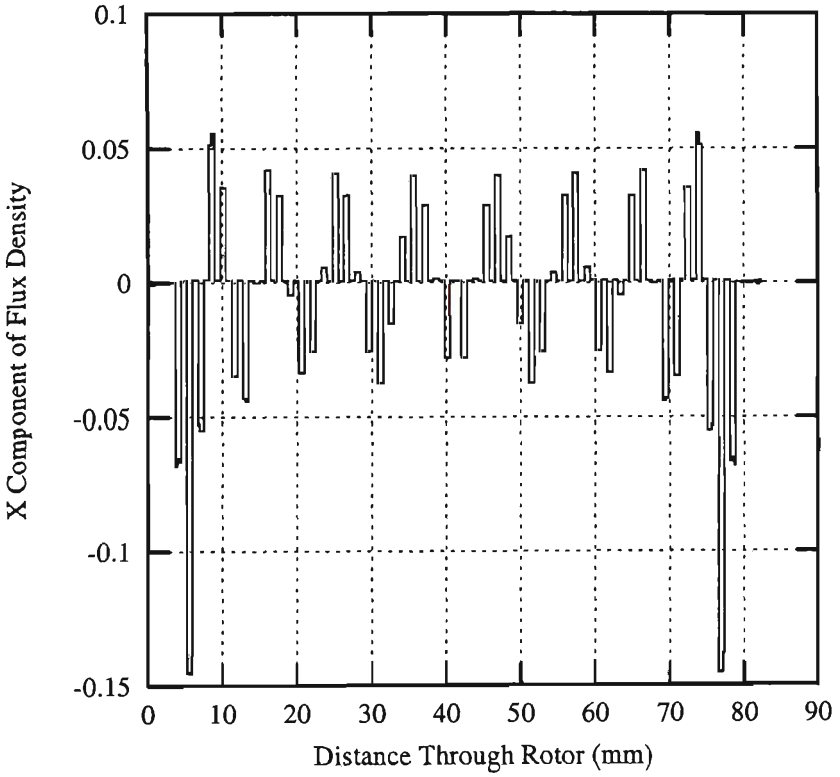

Figure 4.7: Zigzag Flux Phenomenon, Stator Teeth Misaligned

The order of magnitude of the flux excursions has increased by a factor of about 10^5. It is important to note that Figures 4.7 and 4.5 are only relevant for observing the zigzag effect and performing a measurement of the magnitude of the zigzag flux. The observation is a mixture of d-axis and zigzag flux. In order to separate the two effects, observations must be made elsewhere in the machine.

4.4 Machine Flux Correlation

The results presented in the previous section provided a method of visualising the zigzag effect. The zigzag name given to this effect is highlighted in the nature of the flux excursions that are observed. However, it seems incorrect to observe flux distributions normal to the q-axis when in fact it is variations in the q-axis flux that is being sought. The yoke of the machine is the best place to observe any changes in the magnitude of the q-axis flux. The return path for all q-axis flux through the rotor body is via the yoke. This is also true for d-axis flux. However, that part of the yoke where the q-axis flux is at its maximum is the place where the d-axis flux is at its minimum.

The part of the yoke which is of particular interest is indicated in Figure 4.8.

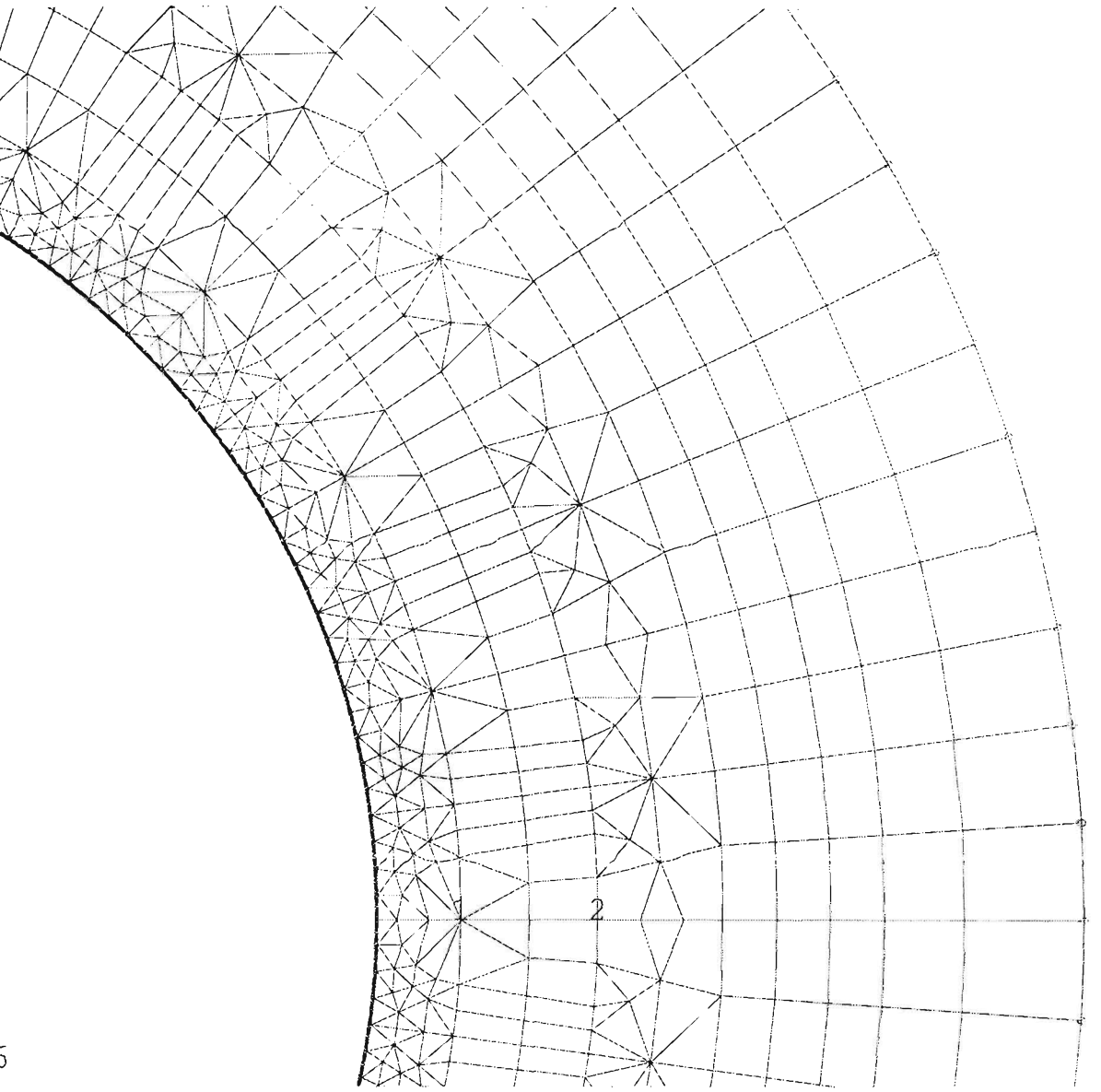

Figure 4.8: Q-Axis Yoke Flux Return Path

The results of the FE analysis allow the observation of the flux vectors in each element. These vectors can be viewed as a full vector result, or the individual x and y components of the vectors. Figure 4.9 is a flux vector plot for the aligned rotor case with an excitation of 4000 A/m of airgap, distributed as a rectangular block. It also shows the slot leakage flux very clearly. The flux returning via the yoke is a combination of slot leakage, zigzag and rotor body flux.

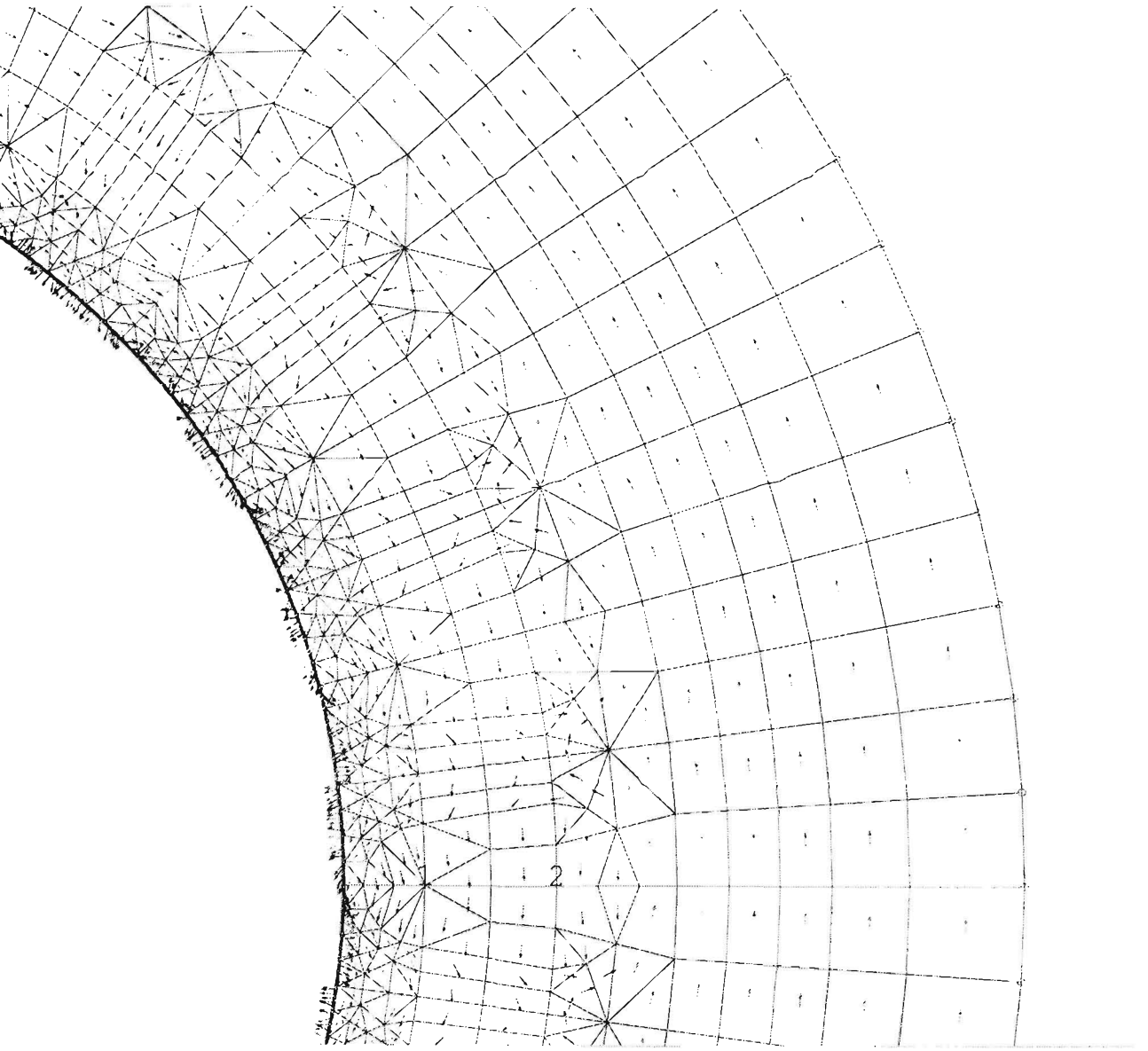

Figure 4.9: Q-Axis Yoke Flux, Aligned Case

Once again, this illustration is essentially for interpretation purposes. The real issue is to try to quantify the effects of the zigzag flux. From the results of the finite element simulation, the overall q-axis flux is calculated based on the numerical results. Knowing the radial width of each element and the length of the stator stack, the total flux can be calculated from the known element flux density and area. The elements of interest are the 6 that extend from the base of the stator slot with the number "2" inside it to the outer perimeter of the yoke.

4.4.1 Rectangular Current Excitation

Using the motor described in Appendix B and a rectangular current distribution of 4000 A/m of airgap, the following set of results is obtained.

Total Flux, FE Analysis, aligned rotor	23.92 μWb
Total Flux, FE Analysis, misaligned rotor	26.73 μWb
Total Flux, Modelling Analysis, aligned rotor	22.58 μWb
Total Flux, Modelling Analysis, misaligned rotor	26.96 μWb

Table 4.1: Summary of Flux Results, Rectangular Current Distribution

There is a strong agreement between the finite element result and that obtained by analytical modelling. Note that no modelling analysis was performed for the aligned case. Also, there is an increase in the overall level of q-axis flux comparing the aligned to the misaligned case. In this instance, the misaligned rotor has an additional 11.7% flux.

4.4.2 Sinusoidal Current Excitation

Using the motor described in Appendix B and a peak sinusoidal current distribution of 4000 A/m of airgap, the following set of results is obtained.

Total Flux, FE Analysis, aligned rotor	22.47 μWb
Total Flux, FE Analysis, misaligned rotor	25.23 μWb
Total Flux, Modelling Analysis, aligned rotor	21.96 μWb
Total Flux, Modelling Analysis, misaligned rotor	25.81 μWb

Table 4.2: Summary of Flux Results, Sinusoidal Current Distribution

Once again there is a strong agreement between the results obtained from the analytical approach and those from the finite element approach. As for the rectangular distribution case, there is an increase in the overall level of q-axis flux

for a misaligned rotor. In this instance, the misaligned rotor has an additional 12.5% flux.

4.5 Conclusions

The previous Chapter presented an analytical model of the SyncRM that was able to calculate a variety of machine fluxes and flux densities whilst taking into account the zigzag nature of the q-axis flux path. This Chapter took the modelling process one step further and produced a finite element model that supports the analytical one.

The FEM devised in this Chapter was a far more complex model than had previously been published. Prior research has assumed a degree of symmetry that meant important effects were being ignored. By modelling the entire machine, it was possible to identify the zigzag flux path and to quantify the effect of this parallel circuit. The FEM confirms the existance of the zigzag flux by aligning the rotor and stator q-axis counter-clockwise by $\frac{1}{4}$ of a slot pitch. Observation of the horizontal component of the flux density through the rotor body indicated the presence of this zigzag flux.

The flux densities predicted by the analytical model are comparable to those predicted by the finite element model. Values were compared for two case; the aligned and misaligned case. These two cases represent conditions that predicted zigzag flux at its minumum and maximum. There was a high degree of correlation between the flux densities predicted by the analytical model and those predicted by the FEM.

This Chapter represents a significant improvement in the finite element modelling of the SyncRM machine by introducing a higher level of complexity that facilitates the identification of the zigzag flux path.

Chapter 5

Sensorless Rotor Position and Speed Estimation

5.1 Introduction

Accurate knowledge of the rotor position is required for the high performance vector control of the Synchronous Reluctance Motor. Without such information, it is not possible to convert quantities in the stator reference frame to those in the rotor reference frame. In conventional drive systems, the position information is obtained by shaft mounted sensors such as optical encoders or resolvers. Such sensors compromise the robustness of the drive system and increase the cost for each drive system.

The SyncRM possesses features that makes it particularly suitable to sensorless operation. Most notable is the distinct difference in the inductances of the d- and q- axes. Recent research has sought ways to implement a sensorless system for the SyncRM in order to make it more competitive with the squirrel cage induction machine. Chapter 2 reviewed some of these techniques, outlining some of the advantages and disadvantages. In that Chapter, the methodologies used were categorised into two broad strategies; parameter dependent and pa-

rameter independent techniques. The use of parameter dependent techniques will always have some sensitivity to variation of the particular values being used. The trade-off here is that in general, such methods provide a higher degree of accuracy compared to the parameter independent way.

A new sensorless algorithm for the estimation of position and speed for a SyncRM is presented in this Chapter. It is a technique that does not rely on any knowledge of machine physical constants, other than the number of poles. The importance of this algorithm is that it does not have the accuracy problems of many of the other parameter dependent methods. The only requirement is that there is a difference in the inductance of the d- and q- axes. The $L_d : L_q$ ratio is a parameter which is maximised in most designs.

The new algorithm also adopts a statistical approach to the position estimation process. Whilst such an approach requires additional computation cycles, it is shown, by simulation, that this has little or no impact on the accuracy of the algorithm. The algorithm works over the entire speed range of the machine. Estimates of rotor position are fed into a modified zero crossing algorithm which then provides estimates of rotor speed. A special start-up procedure is required to establish the initial position of the rotor.

The remainder of this Chapter is organised as follows. The first section describes in detail the basic algorithm used for position estimation. The second section is concerned with improving the accuracy of this algorithm by using a statistical approach. The next section discusses the issue of speed estimation from position estimates and describes a zero crossing technique. The final section presents a detailed simulation of the estimation algorithms used in a complete SyncRM system.

5.2 Rotor Position Estimation

5.2.1 Basic Estimation Algorithm

The defining feature of the SyncRM is the significant difference of the inductances measured in the d- and q- axes. In a modern machine, with an axially laminated rotor, this ratio would be in the order of 10:1. An ideal SyncRM has only these two inductances. In a real machine, winding resistance, leakage reactance, rotor and stator iron losses and saturation in the d-axis are also present.

For the purpose of illustration a computer simulation has been carried out of a SyncRM variable speed drive system. It is based on a model of the SyncRM that has a saliency ratio equal to 10:1 and includes a stator winding resistance. The ratio is a nominal value only, one selected for the simulation. It will be demonstrated later that this value is not critical for the algorithm to produce satisfactory results.

Consider Figure 5.1, a plot of the current space phasor of the SyncRM under a light load rotating at a constant speed of 50 rads^{-1}. It is clear from the inspection of Figure 5.1 that the high frequency behaviour of the current space phasor is to move back and forth predominately in the direction of the q-axis. This is consistent with the inductance in that axis, L_q, being much smaller than that of the d-axis, L_d. The current space phasor contains high and low frequency components. It is possible to filter out the low frequencies by measuring the change in current between consecutive switching instants. The filtered current space phasor consists of a series of straight lines which tend to be longer in the q-axis than in the d-axis.

If the data points from two consecutive switching instants were to be drawn on a graph, then it would look like Figure 5.2.

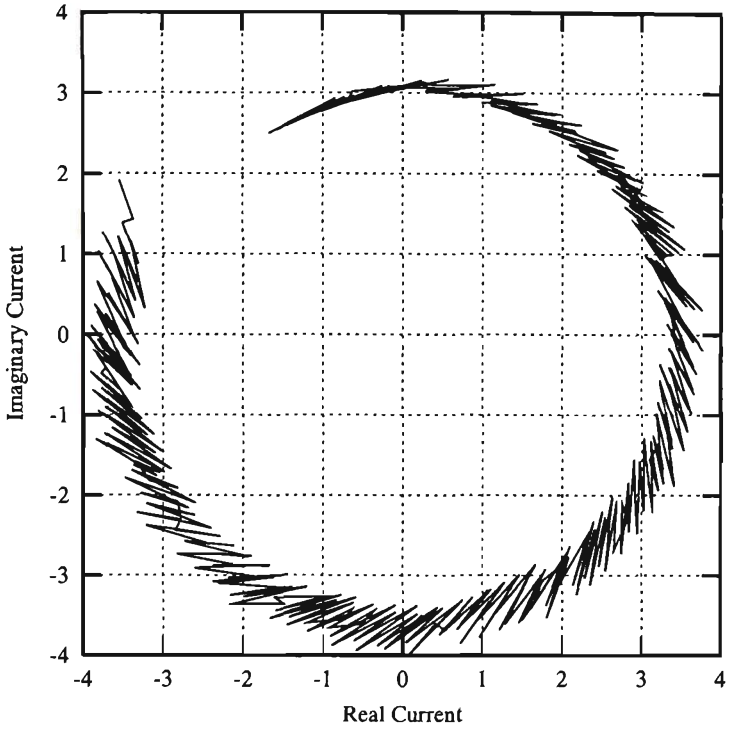

Figure 5.1: Stator Current Space Phasor Under Light Load

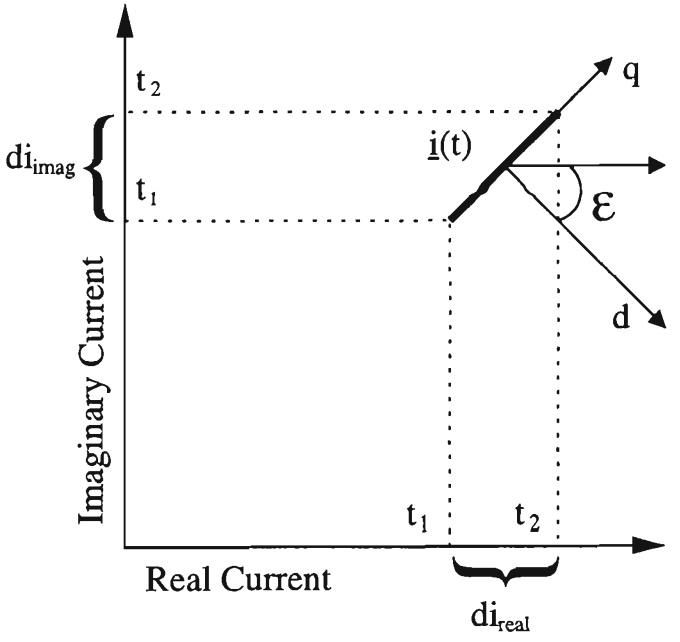

Figure 5.2: Consecutive Stator Current Space Phasor Samples

This is a much closer look at what is happening in Figure 5.1. Thus, if the q-axis is along the incremental current phasor, the d-axis is perpendicular to it. It is therefore possible, using simple geometric relationships, to determine a value for ε, the rotor position. The expression for the rotor position is given in

Equation 5.1.

$$\cos(\varepsilon) = \frac{di_{imag}}{\sqrt{di_{imag}^2 + di_{real}^2}} \tag{5.1}$$

This expression forms the basis of the position estimation technique.

5.2.2 Position Estimation Tracking

In the previous section an expression was given for the estimation of rotor position based on the value of real and imaginary stator currents. This expression provides a value for the sine or cosine of the rotor position. It cannot, however, distinguish between say ε and $\varepsilon + \pi$. In the next data plot, the raw output from the algorithm is presented.

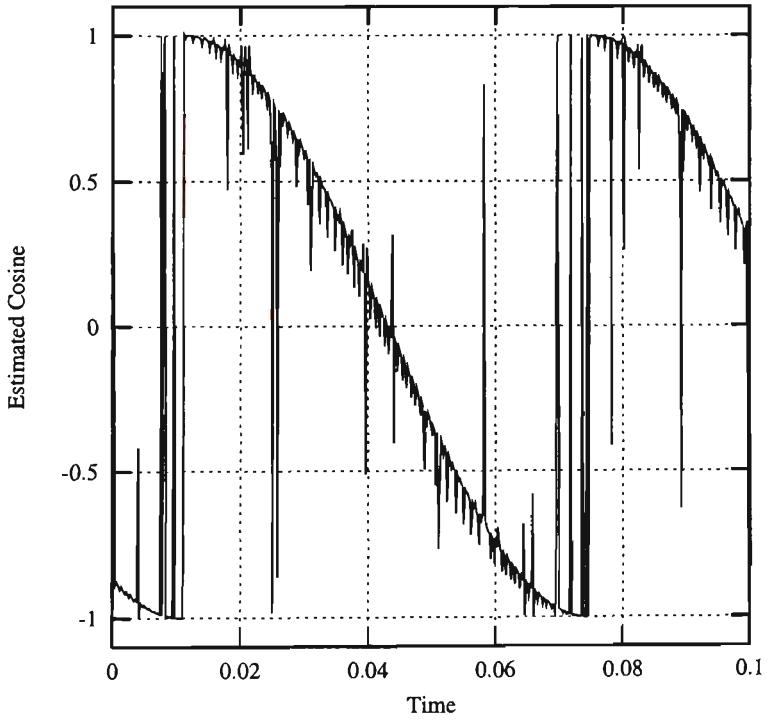

Figure 5.3: Unprocessed Algorithm Output

Observation of this Figure reveals several issues; the output is not continuous and there is noise affecting the quality of the estimation output. These are two separate issues that are dealt with differently.

The tracking problem can be overcome by a simple amount of logic inserted into the estimation process. The requirement is essentially that the output does not change sign, while its magnitude is high (greater than 0.5) without first passing through zero at the correct place. The larger excursions from the signal appears to be noise. What is happening is that the estimation output is switching from $cos(\varepsilon)$ to $cos(\varepsilon + \pi)$. Some of the excursions are switching noise and will be dealt with later in the Chapter.

Insertion of the logic to "track" the output of the algorithm produces a better quality output. The "tracked" version is show in Figure 5.4.

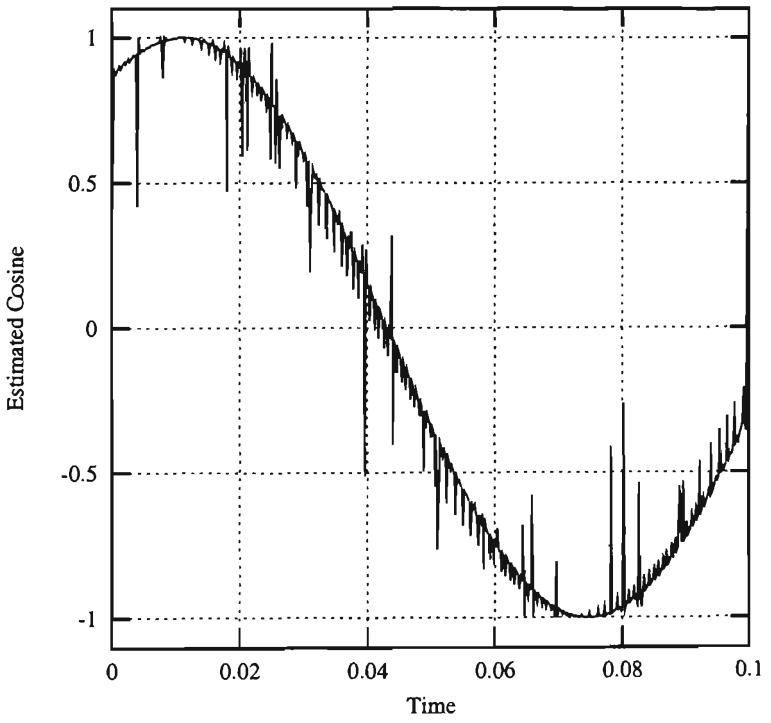

Figure 5.4: Algorithm Output with Tracking Processing

The quality of this signal is better than that illustrated in Figure 5.3. The tracking issue is important. The estimation algorithm cannot jump from ε to $\varepsilon + \pi$. If it was to do so, the the control algorithm would have significant problems. The introduction of tracking should not impede the zero-crossing of the estimated value. The estimation of the cosine of the rotor angle is valid for values less than zero. Its important to ensure that the transition from positive to negative and negative to positive occurs without any "bumps" in the estimated

value.

5.2.3 Low Speed Problem

At low speeds, the processing of the current space phasor requires special treatment. The algorithm requires information from relatively large and frequent values of $\underline{di}$. The simple estimation algorithm does not work well at low speeds since there are many zero vector selections and these result in small values of $\underline{di}$. To overcome this problem, the $\underline{di}$ used in the algorithm is first passed through a speed dependent thresholding filter. The task of this filter is to compare the current phasor with a speed dependent factor. If the current is larger than this factor it is passed through and forms part of the estimation algorithm. If it is not, then no new estimate is made on position.

The filter has the characteristic of passing only the higher values of $\underline{di}$ at the lower speeds. This has the effect of removing less useful data from the algorithm. Although the flow of data is now reduced, at lower speeds this is not a problem. The effectiveness of the thresholding technique is illustrated in Figure 5.5. It shows the position estimation algorithm at work for a speed reference of 5 $rads^{-1}$. The considerable amount of "noise" appearing on the non-thresholded estimation is due to the large number of zero vector selections and subsequent small changes in q-axis current. When the data is passed through the filter, the performance improves to an acceptable result.

The thresholding nature of the filter is observed in the stepped nature of the estimate value. The algorithm does not perform any sort of prediction based on previous estimates. Instead, if a sufficient $\underline{di}$ does not occur, then the algorithm waits. Hence the stepped nature. The threshold filter is implemented as a speed dependent algorithm. In essence, the higher the speed, the lower the minimum value of $\underline{di}$ that is required to make a reasonable estimate of rotor position. Once the rotor has achieved a certain speed, this filter has no effect.

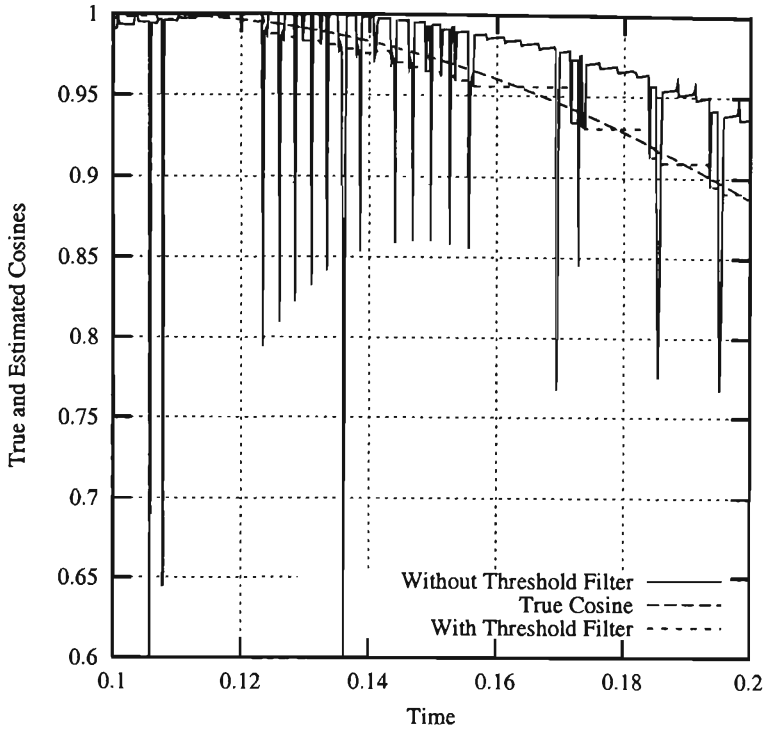

Figure 5.5: True and Estimated Cosine of Rotor Position, Threshold Filter

5.2.4 Statistical Estimation

The simplest form of the estimation algorithm was given in Equation 5.1. Once the "tracking" and low speed problems have been resolved, the problem of obtaining a reasonable quality estimate of the cosine of the rotor position remains. The output from the simplest form of the algorithm was presented in Figure 5.4. Whilst this estimation appears to be clearly sinusoidal in shape, it is not suitable for use as a position feedback signal due to the level of noise that appears on the signal.

It is possible to carry out some simple filtering to improve the quality of the estimation signal. Based on the contention that the largest $\underline{d_i}$ will be in the direction of the q-axis, it makes sense to weight the individual estimates by the square of this distance and take the weighted average over a number of samples. In this way, those estimates that are calculated from larger values of $\underline{d_i}$ contribute to the weighted average more than those with lesser values of $\underline{d_i}$. Figure 5.6 shows the result of taking the twelve most recent weighted estimates.

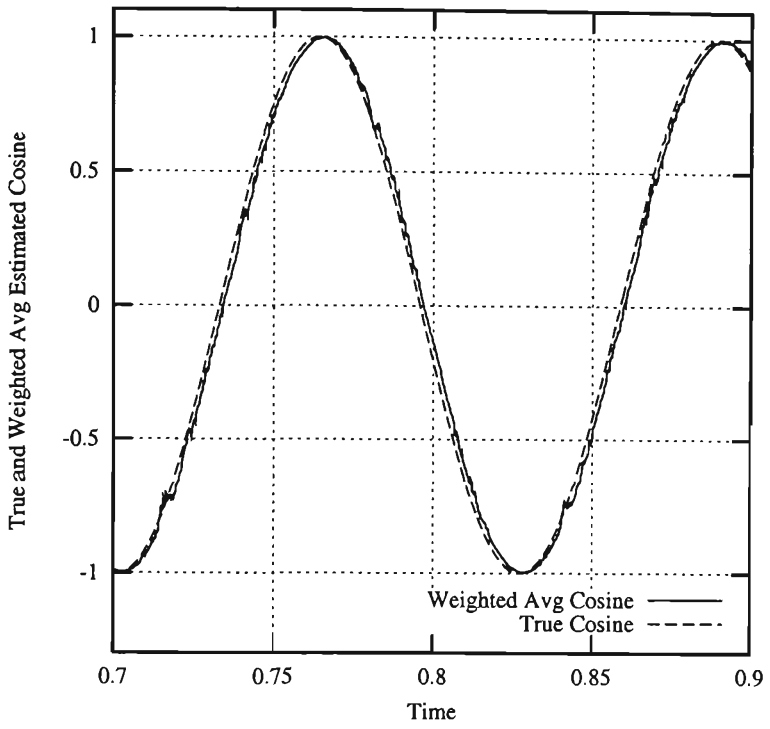

Figure 5.6: True and Weighted Average Cosine of Rotor Position

Clearly this is a superior result compared to Figure 5.4. However, there is still an issue with the sample number for the averaging process. The results in Figure 5.6 were generated using 12 samples, an arbitrary number in the sense that it was the smallest sample number required to produce a satisfactory result. Selection of an arbitrary number leads to inconsistent results when the simulation is extended to cover a broader speed range. It makes more sense to filter the output signal rather than apply a simple averaging technique. Averaging is a simple filter, however applying a digital filter such as a Chebyshev Type 1 filter, a much better result is obtained for a greater range of speeds. Figure 5.7 is a plot of the true and estimated cosine of the rotor position using such a filter.

In Figure 5.7, the filter type used was a 3rd order Chebyshev, Type 1 filter with a passband ripple of -0.01 dB and a cut-off frequency of $0.2 * f_s$. The term, f_s, is the sample and switching frequency, which was 5000 Hz for the results generated. The disadvantage is, however, an increased delay in the output from the estimation algorithm. In Section 5.4 a detailed study is performed of the position and speed simulation. It is shown here that this increased delay has a

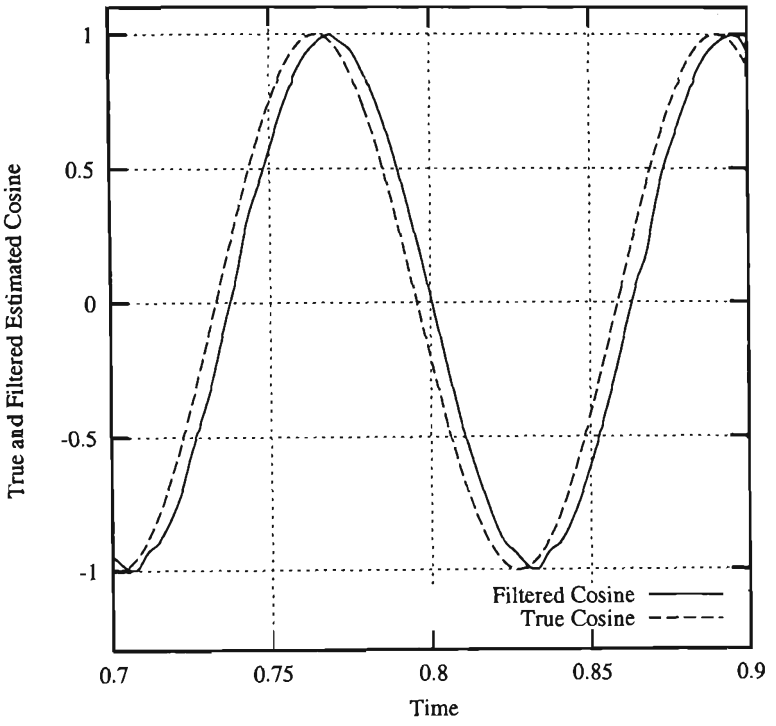

Figure 5.7: True and Filtered Estimate Cosine of Rotor Position

negligible effect.

5.2.5 Saliency variation

The algorithm for the position estimation is robust even when the saliency ratio of the motor is poor. Figure 5.8 should be compared with Figure 5.7. Both are the same simulation, except in the second case, the saliency ratio is 1:3.

Whilst there is a clear degradation in the quality of the rotor position estimation, it is still an acceptable result. The estimation tracks the rotor position well. The result is robust for the speed estimation algorithm as will be demonstrated in Section 5.3. The performance of the algorithm for low saliency ratios is important since it provides insight into the operation of the system under saturation. When a machine is saturated in the d-axis, the inductance of that axis falls, resulting in a reduced saliency ratio.

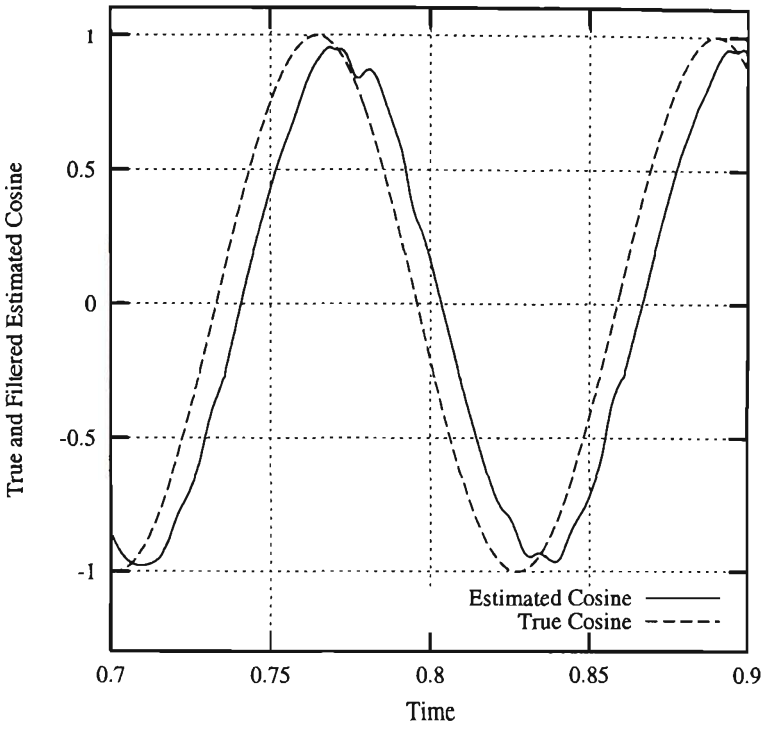

Figure 5.8: True and Estimated Cosine of Rotor Position, Poor Saliency Ratio

5.2.6 Initial Position Estimation

Integral to the problem of sensorless control of the SyncRM is the issue of producing an initial estimate of the rotor position. Without initial knowledge of the position of the rotor, it would not be possible to track the position and hence achieve the desired sensorless control.

During startup, rotor inertia keeps the speed at zero for a relatively large period compared to that of the sampling interval. During this time, the initial rotor position has to be estimated. If a predetermined set of voltage vectors is applied for a short duration during this startup phase, the sensorless rotor position algorithm is able to supply an estimate of the rotor position. The sequence V_1, V_5, V_4, V_6, V_2, V_3 was used. On the average, this should result in zero net torque being produced.

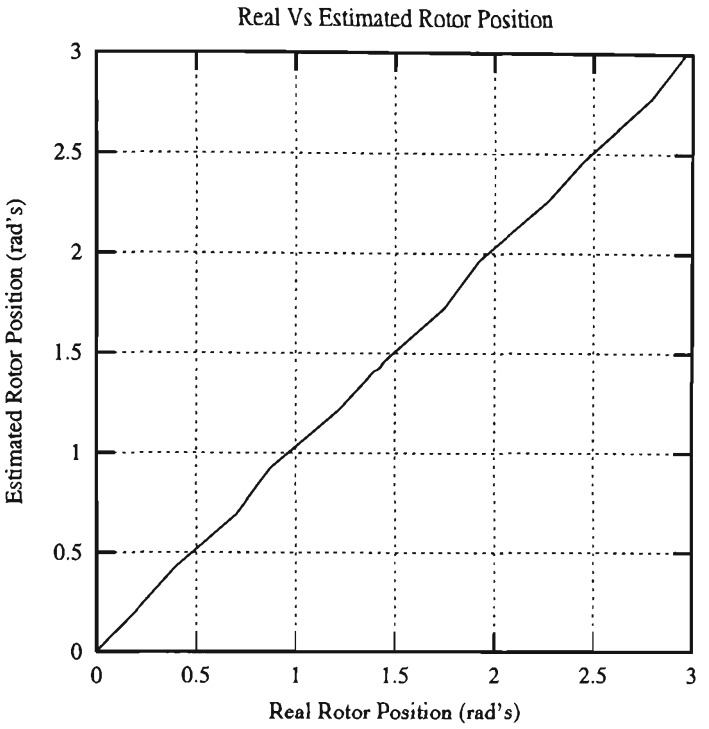

Figure 5.9: Startup Algorithm Performance

Figure 5.9 is a plot of the startup algorithm's performance. If the rotor position was able to be calculated exactly, then the charactersitic of this polt would be a stright line. The algorithm produces estimates which deviate from the ideal response. Section 5.4 addresses this issue.

5.3 Rotor Speed Estimation

Now that an estimation for the rotor position is achievable, it is desirable to be able to estimate the rotor speed. If the aim of the investigation is to provide a method for sensorless control of the SyncRM, then a speed estimator is the next step. The technique used in this thesis is that of a modified zero crossing technique. The simple position estimate is used to produce the speed estimate. It is not sufficient to use a direct derivative of the position signal because although the signal appears to be acceptable, there is sufficient switching frequency signal remaining in the signal to cause severe problems with this approach.

Other techniques, such as direct frequency estimation, whilst providing a

reasonable estimation of speed from the position signal, are computationally intensive and not really suited to on-line speed estimation from a time varying position signal. Several techniques have been investigated using such concepts and it was found that the zero crossing technique provided the best performance versus computational overhead ratio.

Zero crossing is a relatively simple technique that can be used effectively in the estimation of sinusoidal frequencies. In the case of speed estimation, we are seeking an estimate of the frequency of the sinusoid that represents the cosine of the rotor position.

5.3.1 Zero Crossing Method

The interval between zero crossings for a periodic signal gives a good estimation of its frequency with reduced computational effort. It does not, however, give any indication of the frequency content of the signal. This is not an issue in the case of speed estimation. The algorithm that is proposed utilises the zero crossings of both the sine and cosine estimates produced from the position estimation algorithm. By using the two signals, we can obtain estimates of speed at twice the rate that is possible using a single sinusoid. If the computation is made at every zero crossing, then estimates are produced at even closer intervals. The net effect is that estimates of speed are being made $4p$ times per revolution, where p is the pole pair number.

If $K(n)$ is the number of sampling intervals between consecutive zero crossings, then T_e, the estimated period, can be calculated using Equation 5.2.

$$T_e = 4 * K(n) * T_s \tag{5.2}$$

The sampling interval is given by the value T_s. Once the estimation of period is obtained, it can be converted readily to other units to suit those being used in the control system. The disadvantage usually associated with the zero cross-

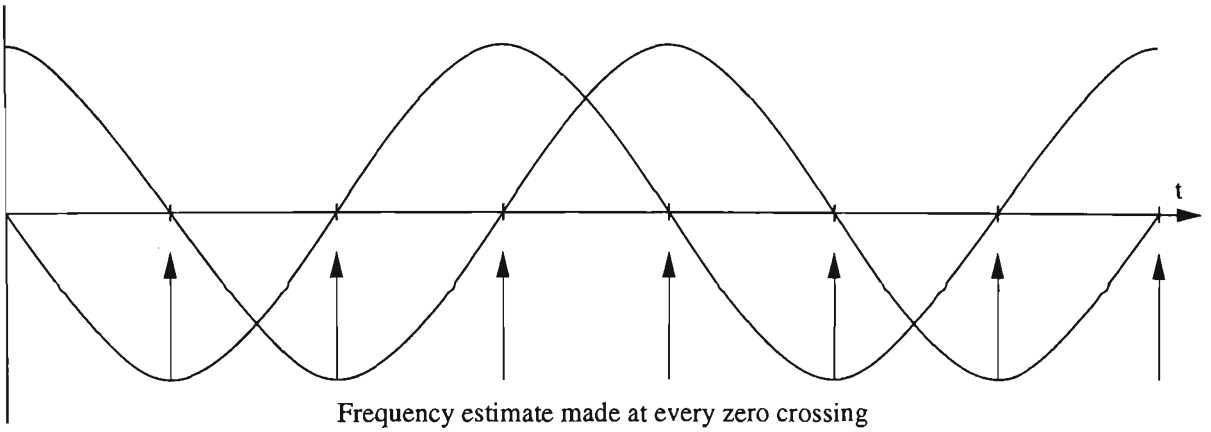

Figure 5.10: Zero Crossing Speed Estimation

ing technique is the reduced number of estimates available at low speed. The method adopted here provides estimates at higher rates since the estimate of speed is made more frequently.

Direction is established by inspection of the phase of the sine and cosine terms. If the sine of the rotor position leads the cosine of the rotor position, then the motor is rotating in the clockwise direction. If the inverse is true, then the motor is rotating in the opposite direction. The difficult period for direction selection occurs at very low speeds during the changeover from one direction to the other. The filtering used in the algorithm is sufficiently robust to provide a signal whose quality allows the directional logic to function accurately.

5.4 Position and Speed Simulation Study

This section presents a variety of results from the simulation study performed using the position and speed algorithms presented. The purpose of the simulations were to determine the accuracy and usability of these new algorithms. The results that have already been presented are based on the output from such simulations. Fine tuning of the filtering parameters, accuracy at low and high speed as well as the start-up issue were all resolved using a simulation as a mechanism for testing the concepts.

The simulation is that of a Synchronous Reluctance Motor drive system,

operating under load in closed loop. Two methods of providing speed feedback were employed. The first involved using an inertial model of the simulated drive system to calculate the speed of the drive. The second method uses the estimated speed as the the feedback for the control algorithm. In the text that follows, these two methods will be referred to as either the "Exact Feedback" case or the "Estimated Feedback" case.

The simulated motor is similar to the device used in the experimentation phase. It is a 6 pole, axially laminated reluctance motor. The per unit base for this machine is (Platt et al., 1993);

1 pu power	22 kW
1 pu voltage	415 V RMS
1 pu current	17.7 A RMS
1 pu impedance	23.4 Ω
1 pu frequency	50 Hz
1 pu speed	104.7 rad/s
1 pu torque	210 Nm

Table 5.1: Simulated SyncRM Parameters

The control system of the simulated system is a simple set up. The controller consists of a simple PI torque control loop. The torque reference is limited to 1.5 times the rated torque (315 Nm). The drive is assumed to be unloaded and the moment of inertia is 1.0 kgm^2. This parameter is an assumed value since the actual rotor moment of inertia was not known at the time of the simulation studies. The controller maintains a constant value of i_d and the torque is controlled solely by variation of i_q.

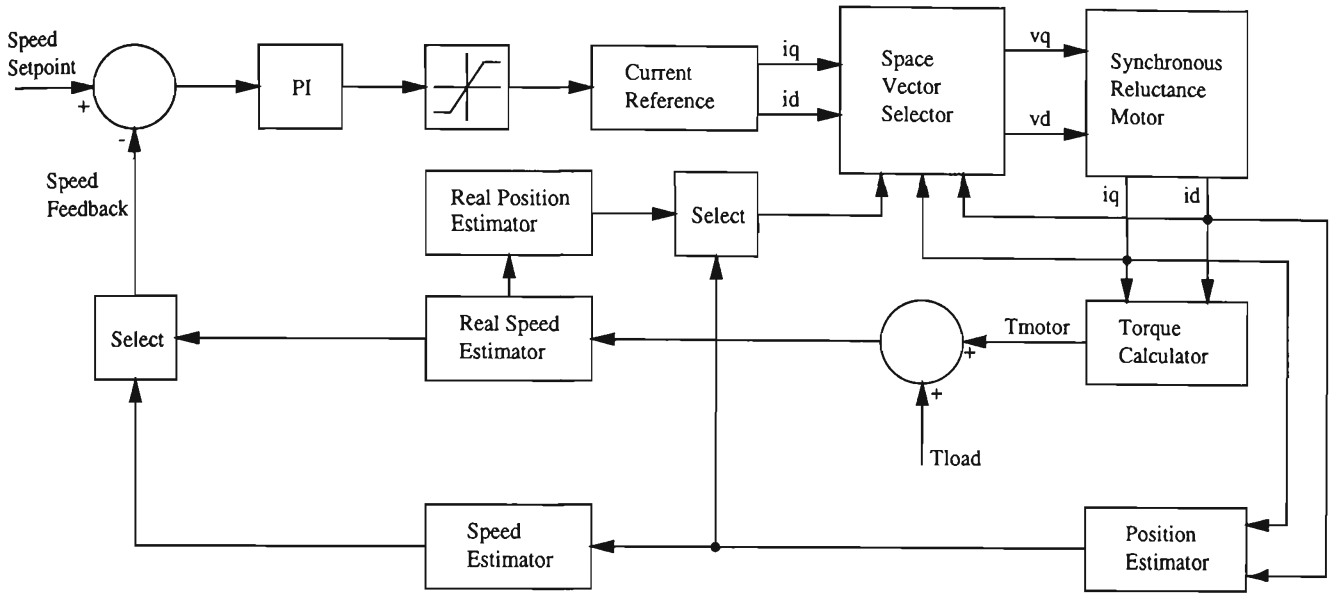

Figure 5.11: SyncRM Simulation Block Diagram

Figure 5.11 represents a simplified block diagram of the Synchronous Reluctance Motor simulation. One speed estimator represents the actual motor speed and the other represents the estimation of the motor speed. They both exist as estimators since it is a simulation and not a real world implementation. If it were a real implementation, then the "Real Speed Estimator" would be a block of code estimating speed from data derived by a shaft encoder, for example.

The "Select" function in the speed feedback loop allows the changeover between "Exact Feedback" and "Estimated Feedback". Ordinarily, this selector chooses the source of the speed feedback to be the exact or estimated source. There is no changing of the source during the course of the simulation. The startup code is not represented in Figure 5.11. This is for the sake of clarity. In essence, the estimation of the motor starting position is made before the illustrated simulation takes place.

5.4.1 Exact Feedback Simulation

The exact feedback case represents the most common form of speed control. It is analogous to the motor and sensor combination, where the sensor is an encoder that measures rotor position. In the simulation, the rotor position is

estimated from an inertial model of the reluctance motor. The control rate for this and all the other simulations is fixed at 5-kHz, which is also the switching frequency of the inverter.

The first set of results shows the controller in action. It is a plot of the speed setpoint, actual speed and estimated speed as a function of time. The controller accelerates the drive at current limit and then stabilises the torque reference once the desired speed has been achieved. The PI regulator was tuned for optimum performance and the gains are maintained constant over the entire speed range of the drive system. The response chosen to first demonstrate the simulated system is a step response with a full speed reversal. Figure 5.12 presents the speed response results.

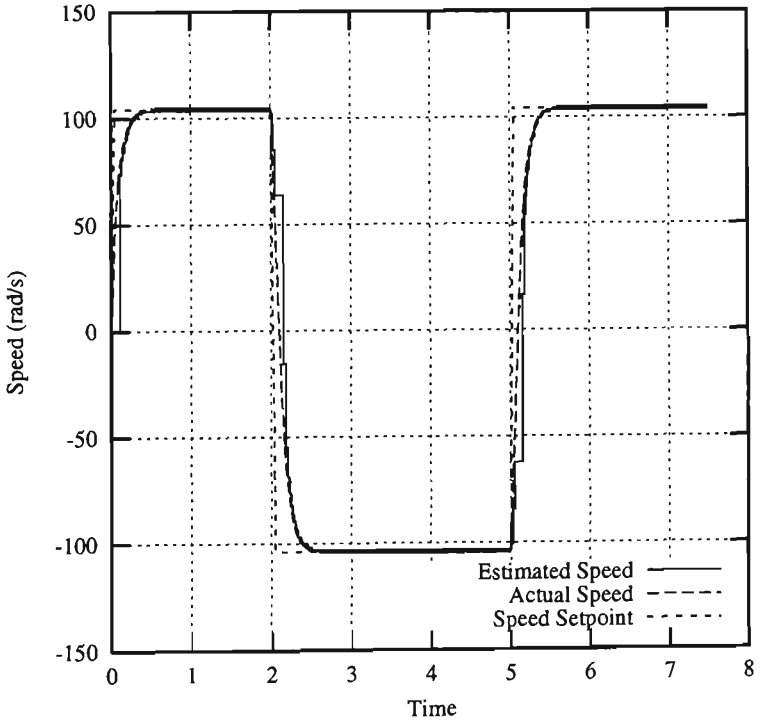

Figure 5.12: Exact Feedback Speed Response

The motor exhibits the typical response of a drive accelerating under current limit. The more important result of this simulation is the performance of the speed estimation algorithm. Figure 5.12 also shows the effectiveness of the speed estimation algorithm. It is able to track the actual speed of the Synchronous Reluctance Motor. Recall that in the exact feedback simulation, the speed

feedback of the drive system is the actual speed and not the estimated speed. Performing the simulation this way, it is possible to observe the behaviour of the speed estimation algorithm. The stepped nature of the zero crossing estimation technique is observed.

Figure 5.13 is a plot of the machine torque. The torque limit can be observed limiting the torque applied to the motor current reference calculator during the acceleration phase. From the test results obtained by the authors of (Platt et al., 1993), this machine is capable of producing far more torque than the limit used here. The point of this simulation, however, is to observe the performance of the speed estimation algorithm. The third and final plot is that of the q-axis current and is given in Figure 5.14. Since the method of torque control is to maintain i_d constant and vary i_q, it is interesting to observe the behaviour of this controlling current. As expected, the i_q waveform is very similar in shape to that of the torque waveform.

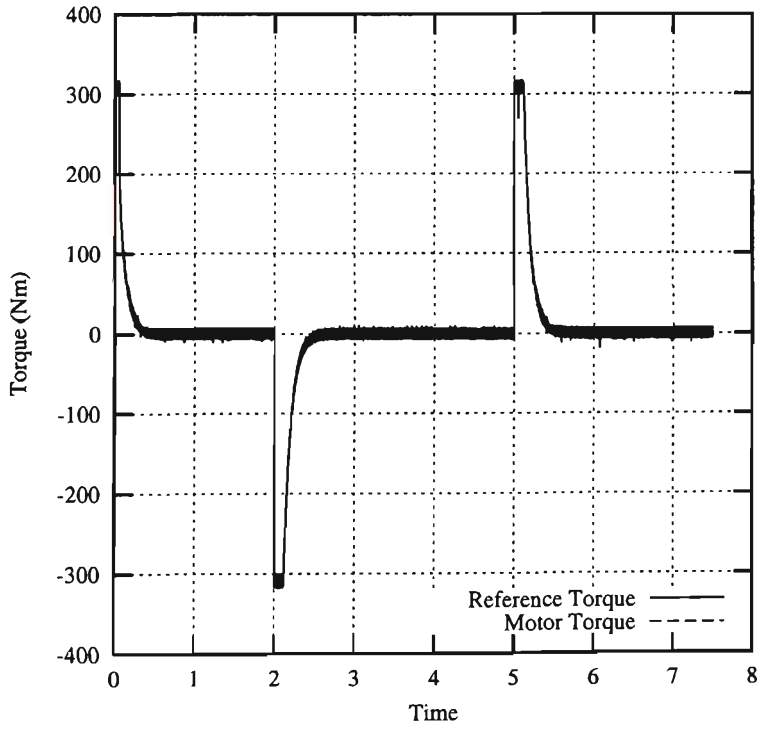

Figure 5.13: Exact Feedback Torque Response

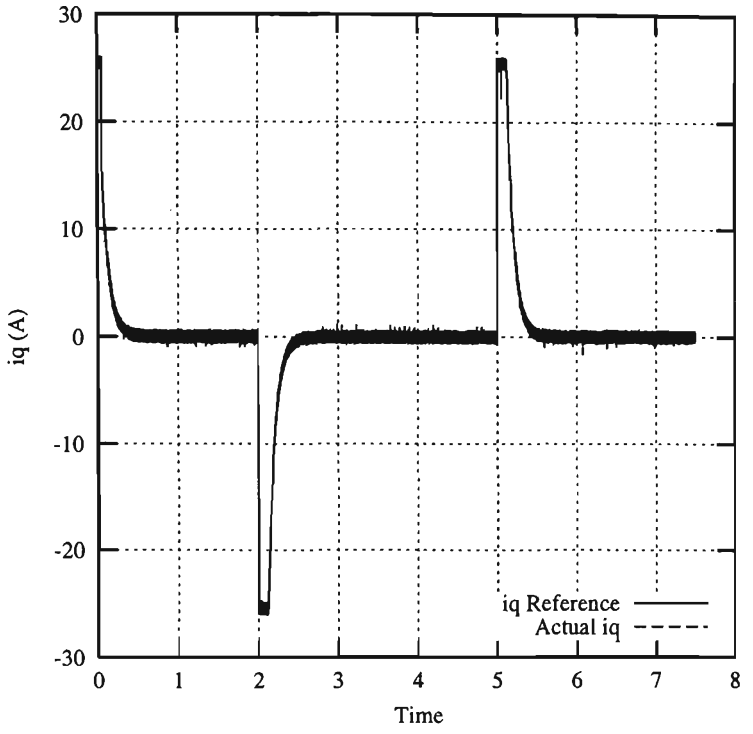

Figure 5.14: Exact Feedback iq Response

5.4.2 Estimated Feedback Simulation

This section presents simulation results that illustrate the accuracy of the new sensorless speed estimation algorithm. The results that follow are similar to those presented in the previous section. However, this time, the feedback of the motor speed comes from the new estimation technique and not from the real motor speed. Referring to Figure 5.11, the blocks labelled "Select" are switched over to direct the calculation from the "Speed Estimator" and "Position Estimator" blocks. The initial rotor position is known prior to the commencement of the dynamic simulation. This is achieved by the use of the startup algorithm described in Section 5.2.6.

The accuracy of the estimation method has already been demonstrated in the previous section. Even though the control loop utilised the "Exact Feedback" path, the speed estimator tracked the actual speed very closely. The results from a simulation using this "Estimated Feedback" are very similar to those results obtained using the "Exact Feedback". Such a set of results are

presented in Figure 5.15.

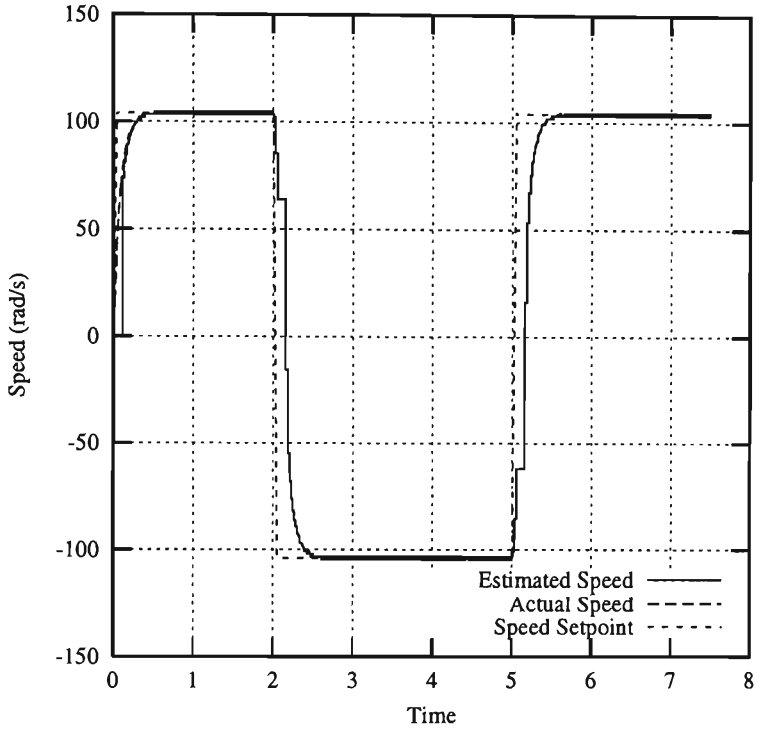

Figure 5.15: Estimated Feedback Speed Response

To the naked eye, Figures 5.15 and 5.12 look identical. There are a few subtle differences. One method of measuring the performance of the algorithm is to calculate the mean squared error between the motor speed and the motor speed setpoint. Equation 5.3 represents the mean squared error calculation.

$$MSE = \frac{\sum_{i=0}^{n} (\omega_{err_i})^2}{n} \tag{5.3}$$

The value w_{err_i} represents the speed error at sample i and n is the total number of samples. The MSE for the "Exact Feedback" simulation illustrated in the previous section was 22.66. The same simulation using the "Estimated Feedback" produced a MSE of 24.15. This represents a minor deterioration in the overall performance.

5.5 Conclusions

This section introduced a new method of rotor position and speed estimation for the Synchronous Reluctance Motor. The method has been shown, through simulation, to be effective despite knowledge of the machine inductances. This is an important factor is designing an algorithm to provide rotor position estimation.

The results of all the simulations presented in this paper have been based on an ideal machine with L_d, L_q and R_s. The effects of iron loss have been ignored. Another critical assumption is that the sampling occurs at the exact point in time that the inverter switching takes place. Each voltage vector is applied for a fixed period of time, δt, equal to 0.2 milliseconds.

A set of computer simulation studies were performed to evaluate the performance of the new speed estimation algorithm. The simulation used a simple PI speed control system and the modelled Synchronous Reluctance Motor resembled the laboratory machine. The results of the estimated feedback case reveal a slightly worse mean squared error when the speed estimator is used in the feedback path.

Plots of the performance of the algorithm were made for the unloaded case. The drive was give a full speed step followed by a period of constant speed and then a full speed reversal. The system response was typical of a drive system accelerating under current limit for both cases. The speed and position estimation algorithms performed accurately during speed reversals.

Chapter 6

Experimental Results

6.1 Introduction

In Chapter 5, details of the rotor position sensing and speed estimation algorithms were presented. A detailed simulation study provided results that demonstrated the viability of the algorithms used. This Chapter takes the process to the next level and present the results of the "real world" application of these algorithms.

The implementation of the algorithms using a realistic scenario is important since it is the ultimate proof of the usability of the concepts developed. There are many variables that are introduced with a real system that are not included in the simulation models. Of particular interest is the ability to measure the line currents with sufficient accuracy so that the estimates of the d- and q-axis currents can be made. The sensorless scheme depends on the reliable measurement of these parameters.

The experimental setup includes a PC hosted DSP control card, a customised version of a commercial inverter and a 6 pole, 22 kW SyncRM with an axially laminated rotor. This Chapter describes the experimental validation of the sensorless rotor position algorithm.

The remainder of this Chapter is organised as follows. The first section describes the experimental setup. An outline of the hardware and software used and developed is presented. The next section presents the results of the validation of the startup algorithm. Since this is a key part of the overall control strategy, it is important to observe the performance of the algorithms for the case of a standstill rotor. The following section presents the experimental work associated with the validation of the rotor sensorless position control scheme. It is essentially an analysis of the results for a wide range of speeds of the SyncRM. Results on the performance of both the position sensing and rotor speed estimation are given. Finally, some comments on accuracy and performance are presented.

6.2 Experimental Hardware Setup

The experiments performed were aimed at establishing the validity of the sensorless rotor position detection algorithms developed in Chapter 5. The hardware used includes a PC and Digital Signal Processing Card, an Inverter and a SyncRM. Figure 6.1 illustrates the key elements of the experimental setup.

6.2.1 Computer Hardware

The personal computer (PC) is the central component of the experimental setup. A Digital Signal Processor (DSP) based control card is installed in the PC. The signals to and from the various sensors and the inverter are all connected to this DSP card. The DSP runs the software that controls the inverter and consequently the SyncRM. The software is written using the "C" programming language.

The DSP card is made by a company called Innovative Integration. The card is referred to as the ADC64. The card is essentially a data acquisition device but is also suitable for control applications. A brief description of this board is given

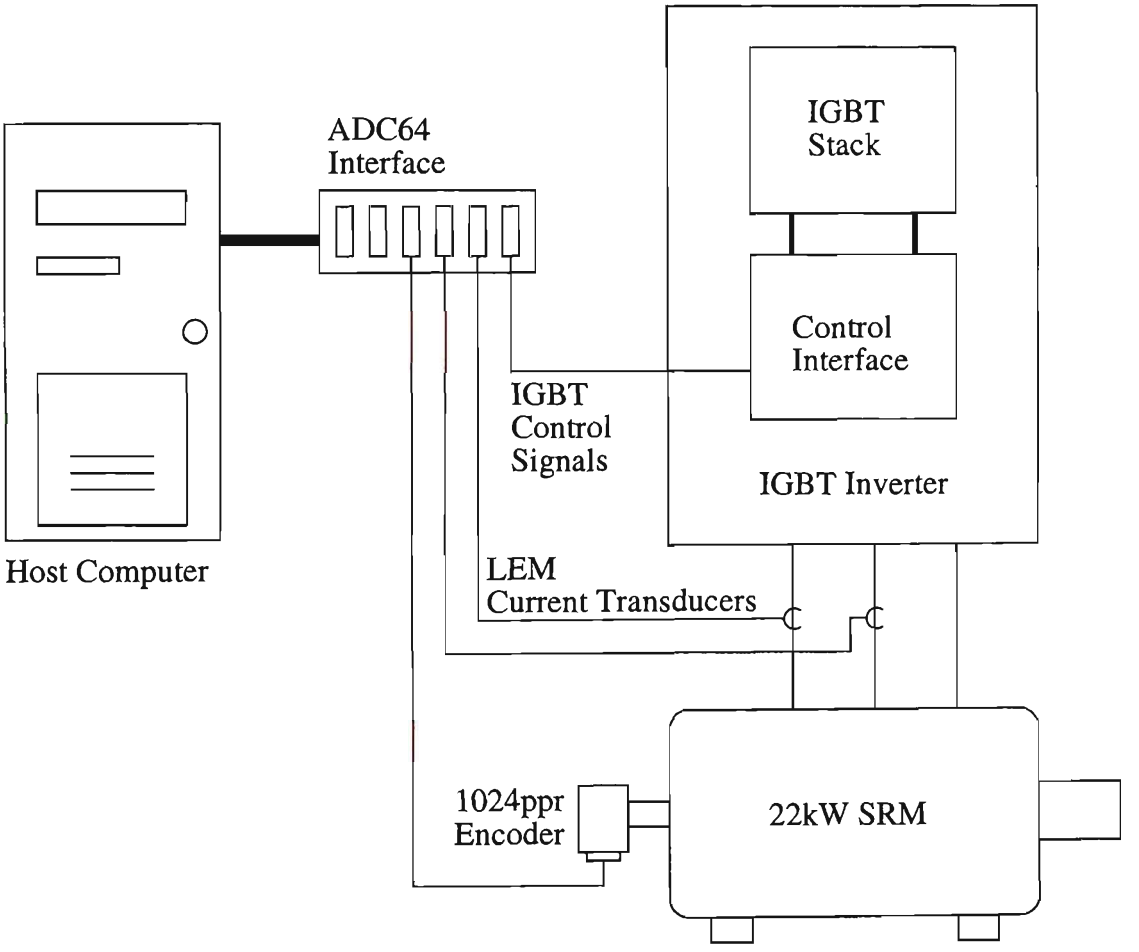

Figure 6.1: Experimental Setup

in this section. Details of the ADC64 can be found in (Innovative-Integration, 1996).

The ADC64 interface card has the following features;

1. TMS320C32 DSP clocked at 60MHz.
2. 64, 16bit A to D Converters with a maximum sampling rate of 200kHz.
3. 16 bits of TTL compatible digital I/O.
4. 2, 16 bit A to D Converters rated at 200kHz.
5. 1, 16 bit timer using an independent 10MHz timebase.

Programs for use by the ADC64 are developed on the PC. A set of libraries are provided by the manufacturer so that interfacing to the hardware of the ADC64 is possible from within the "C" programming environment. Once the code is written, it is compiled using a Texas Instruments Compiler. The output of the compiler, once it is linked with the run-time libraries, is an object file that is "downloaded" to the ADC64 for execution. If there is no streamed I/O used in the code that is downloaded, then the program running on the ADC64 does so essentially independent of the host PC. In this way, the performance of the code is not limited by the performance of the PC.

All of the signals required for the experiments are wired back to an interface card located externally to the PC. This interface card provides a convenient place for terminating the signals. A multi-core cable with the required 100 pin connector is then used to connect the ADC64 card to this interface. This point of termination makes the task of modifying or adding to the interface much simpler than having to modify a 100 pin connector.

6.2.2 IGBT Inverter

The IGBT Inverter used for these experiments is not a custom built device. The device ratings are given in Table 6.2.2.

Parameter	Rating
Supply Volts	460 VAC
Nominal DC Bus Voltage	600VDC
Continuous Current	52A
Peak Current	78A

Table 6.1: IGBT Inverter Ratings

This inverter was donated to the University by Australian Baldor. It is a Baldor SweoDrive 914L-58-240 Device. More details about the device can be found in (Baldor, 1993). The device was customised to suit the interface requirements of the DSP. For experimental purposes, the controller supplied with the inverter is not required. The circuitry was modified such that the ADC64 was able to control the inverter. This included a circuit between the ADC64 and the IGBT stack that ensures that shoot-through could not occur. The delay between turning off one device and turning on the other device in the same leg was set at $2\mu sec$.

6.2.3 Current Measuring Devices

Two Hall-effect current sensing devices are used to measure the current in two phases of the SyncRM. The sensors used are the LEM Current Module, Type 50PS1. The output of the device was configured so that a $\pm 50A$ current produces a $\pm 5V_{DC}$ output.

6.2.4 Synchronous Reluctance Motor

For more detail about this device, the reader should refer to Appendix E. The device is a 22kW motor with an axially laminated rotor. The stator is from a standard 22kW squirrel cage induction motor. The rotor was designed and built by the Pacific Power Energy Efficient Research Centre a t The University of Wollongong. Figure 6.2 is a simplified cross section of the rotor (Platt et al., 1993).

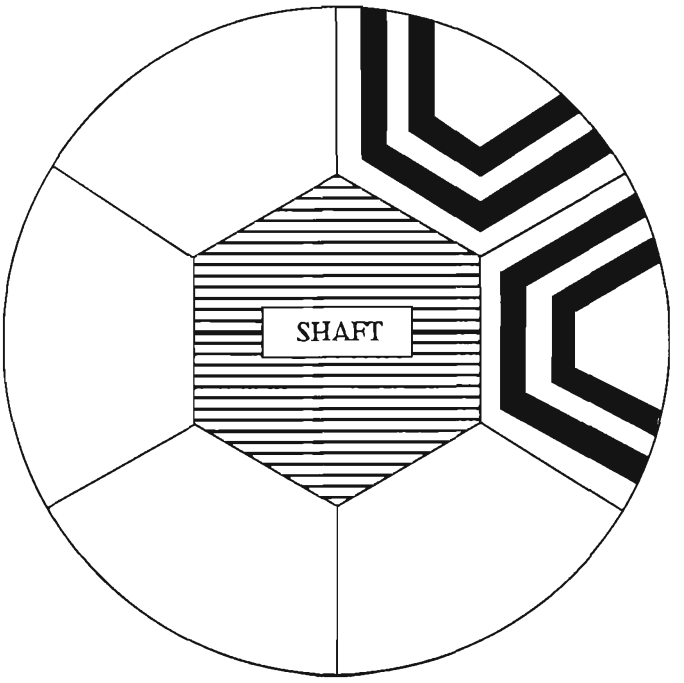

Figure 6.2: Simplified Rotor Cross Section

The poles are formed by alternate laminations of iron and non-magnetic material. The rotor has a ratio of magnetic to non-magnetic material of 1.5:1 (Platt et al., 1993). The slots of the stator are straight cut and the rotor was also built without skew. There are 17 magnetic and 17 non-magnetic laminations per pole.

Motor Parameters

A series of tests had previously been performed for this motor (Platt et al., 1993). The key results of these tests are included here for completeness. Please note that these results are direct extracts from (Platt et al., 1993) and not original work performed for this thesis.

Tests performed included a DC Resistance and Magnetisation tests. The results of these tests are presented in Table 6.2.4.

Parameter	Value
DC Resistance	0.3Ω
d-axis Inductance	0.135H
q-axis Inductance	0.013H

Table 6.2: Test Motor Parameters

6.2.5 Shaft Encoder

The shaft encoder is required to test the accuracy of the sensorless algorithms against a true, measured position signal. The device was also used during the early commissioning phase to observe the performance of the rotor position estimation prior to using this calculated value in the feedback loop of the control system. The device used is a Dynapar H20 Hub Shaft encoder that provides 1024 pulses per motor revolution.

6.3 Experimental Software Setup

The simulation studies presented in Chapter 5 form the basis of the software used in the implementation phase. When the simulation software was written, this requirement was always kept in mind. Essentially, the code for the simulation is identical to the code used in the implementation, except that now

currents are measured rather than simulated from a simple model. The sensor based control also utilises measured values of rotor potion and hence speed. Just as with the simulation studies, the experimental work first utilises sensor based feedback. This way, the controller can be commissioned and the performance of the motor observed. Once a desired performance is established, the sensorless algorithms can be used to close the feedback loops and the performance re-observed.

6.3.1 Main Program

In the real-time implementation of the sensorless control, the bulk of the processing is done in the interrupt control routine. There is an outer program, here called the main program, which deals with the start-up, initialisation of parameters and shutdown processes. Within the main loop, there is an interrupt control routine which runs at the sampling rate and it is used to perform the control, position estimation and vector selection. The following sections represent the structure of the main program.

- Software and Hardware Initialisation. This part of the program initialises software variables to some starting value. It also initialises I/O ports to be either input or output and sets up the hardware associated with the on-board D-to-A and A-to-D.
- User Interface. One of the features of the ADC64 DSP Card is the provision of a terminal interface to the software running on the card. Whilst access to these features is not possible during execution of the main control program, during the initialisation phase the user interacts with the program. During this phase, there is a procedure for establishing the initial rotor position.
- Interrupt Set Up. The timers used as part of the A-to-D conversion process and for generating a periodic interrupt need to be initialised. The periodic interrupt is used for the control section.

- Program Exit. Once the interrupts have been set up, control of the program the passes to the periodic interrupt handler. Since the code is running on the ADC64 and I/O interaction uses up too much time, it is not possible for the user to interact with it while the motor is being controlled. However, during the "User Interface" phase, the length of time that the program is required to run is one of the parameters entered. So, for example, if the user wanted to step the motor up to a certain speed and stay at that speed for 2 seconds then stop, then after the motor has stopped, control would then be given back to the main program from the interrupt handler. At this point, the inverter is placed in a safe state and any variables that were being logged while the control program was running are written to a file for offline processing.

The bulk of the work is performed by the interrupt handler. The pseudo-code associated with this routine would look like;

```
software_and_hardware_initialisation();
user_interface();
interrupt_setup();
do {
   do {
   } while(waiting for next interrupt);
   control_motor();
} while(control is required);
program_exit();
```

This is another way of representing the previous list. The nested "do-while" loops are the interrupt control routine. During the "Interrupt Set Up" phase, the periodic interrupt is set to occur at a rate of 5000 Hz. Thus, once program execution passes the set-up phase, the program sits in a loop, doing nothing until the next interrupt occurs. When it does, the program executes the control

and estimation functions then waits for the next interrupt, provided the run time has not expired.

6.3.2 Interrupt Control Routine

The control flow of this section of code is very similar to the original simulation code. The main variation is the interfacing requirement. The flow of the code is given in the following list.

- If the controller is not in sensorless mode, then the first task is to read the encoder value. The value that is obtained from the hardware is then translated into an electrical rotor position.
- The next task is the sampling of the analog signals. These include the two phase currents and the inverter DC bus voltage. The former is used in the control and rotor position estimation and the latter is used as an input to the regeneration control. Once the analog values have been sampled, they are scaled into values that reflect the parameter they are measuring.
- The phase currents are translated from 3 phase quantities into the two phase equivalent. This task is performed using the "Clarke Transform" (Fitzgerald and Kingsley., 1961). The mathematics of this technique are presented in Appendix D.
- The estimation of the rotor position is now performed. Data from the most recent value of phase currents along with previous values is used as explained in Chapter 5.
- With a new value of rotor position, a value for the speed estimation can now be made. This algorithm uses the modified zero crossing technique as described in Chapter 5.
- The currents are then translated into d-q form and used in the control algorithm. The control algorithm includes the speed control and inner

current loop. The output from this current loop is the voltage vector required for the motor. This is essentially the switching state of the inverter until the next control interval.

- Finally, a section which is not directly associated with the control of the motor is required. This phase updates the value of the digital-to-analog converters and writes variables into a storage array. The DAC is used to monitor some program variables in real-time so that they may be recorded outside of the main program. The write to a storage array is also used to store program variables that will be downloaded onto the disk of the host PC once the program completes.

Figure 6.3, on the following page, is a block diagram of the sensorless control scheme. The control scheme utilising the shaft encoder is omitted for clarity. When the experiment is operating in sensorless mode, the shaft encoder has no functionality.

The bulk of the calculations are done in the d-q reference frame. The phase currents are converted from the stator reference frame to the d-q reference frame using the current rotor position estimation. The newly calculated values for i_d and i_q are then used by the position estimation algorithm. The output of this algorithm is both the *sin* and the *cos* of the rotor position (in electrical radians). This information is applied to this zero crossing speed estimation code that outputs an estimated speed.

The speed regulator is a proportional-integral (PI) type that outputs a motor torque. The torque calculator determines the required i_q to establish this torque. The d-axis current is fixed in value. These references become the input to the current controller. This control block examines the error between the reference value and the actual value and calculates the appropriate voltage vector to affect the changes in current required. At this point, all the information that is needed to determine the required inverter state is know and that state is determined accordingly.

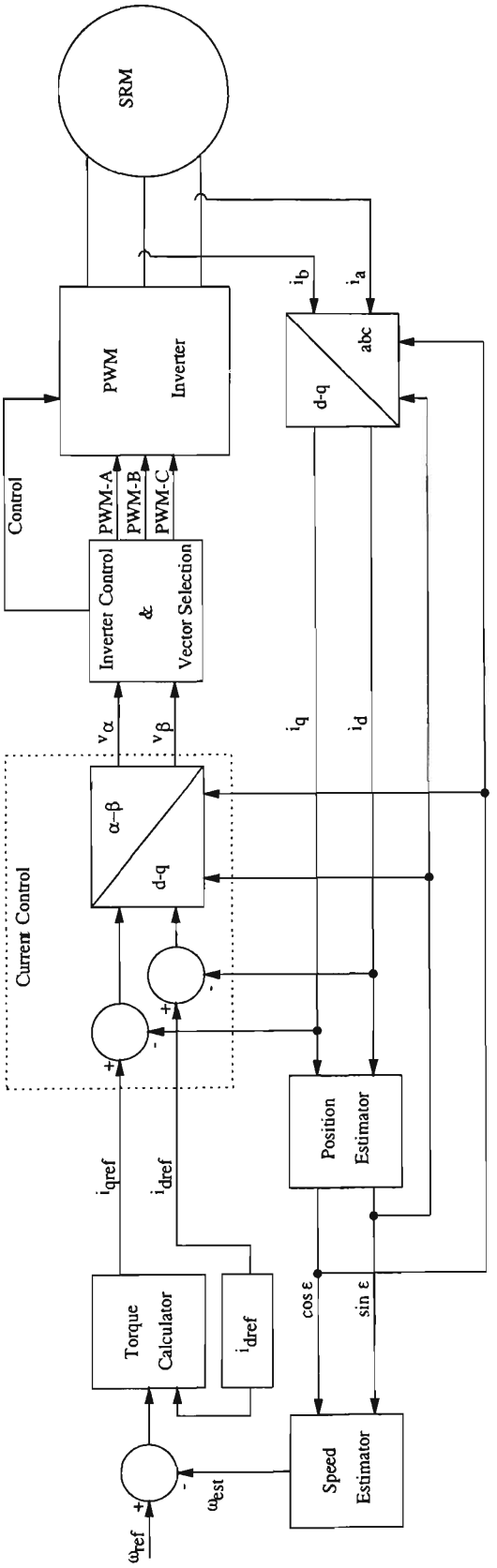

Figure 6.3: Sensorless Control Block Diagram

6.4 Startup Algorithm Performance

In a vector control scheme it is important to know the position of the rotor. This does not exclude the starting scenario. The rotor position technique developed for this Thesis is capable of measuring the rotor position at standstill.

The method implemented is the same as that presented in Chapter 5. The technique involves applying a predetermined set of voltage vectors to the motor. The resulting currents are analysed and the resulting position of the rotor is determined. Table 6.3 represents a set of results obtained using this technique. The rotor was placed in several positions and the estimated position was calculated. The actual position was established using a shaft encoder.

Actual Position (Radians)	Estimated Position (Radians)	Estimation Error (Radians)
0	0.1198	-0.1198
0.5	0.5175	-0.0175
1.0	1.1318	-0.1318
1.5	1.5183	-0.0183
2.0	1.9719	0.0281
2.5	2.3819	0.1181
3.0	3.1253	-0.1253

Table 6.3: Sensorless Initial Rotor Position Estimation Performance

These values represent one set of results and Figure 6.4 is a plot of this set of results. The repeatability of the techniques is satisfactory. Table 6.4 shows a set of results for several attempts at estimating the same rotor position.

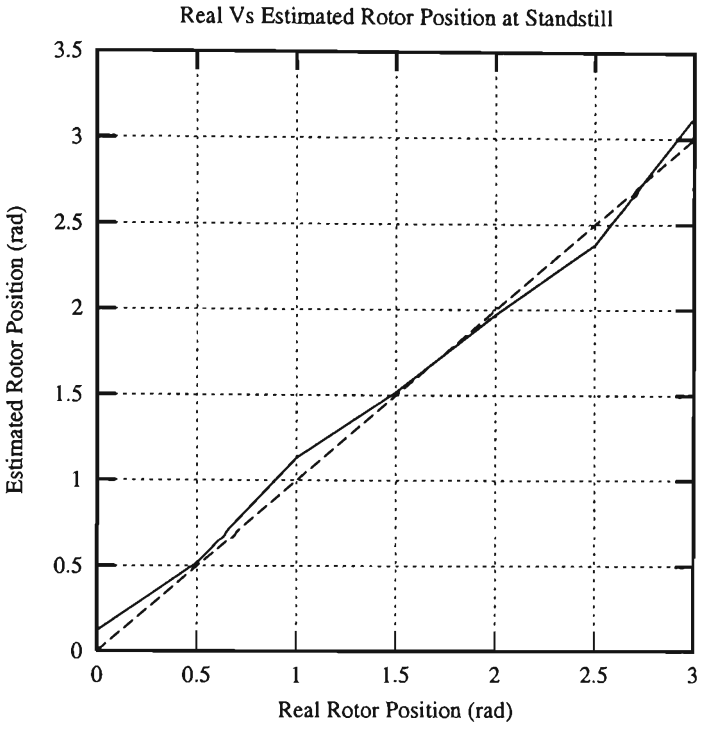

Figure 6.4: Startup Algorithm Performance

Actual Position (Radians)	Estimated Position (Radians)	Estimation Error (Radians)
0.5	0.5183	-0.0183
0.5	0.5175	-0.0175
0.5	0.5192	-0.0192
0.5	0.5166	-0.0166
0.5	0.5088	-0.0088
0.5	0.5157	-0.0157
0.5	0.5174	-0.0174
0.5	0.5149	-0.0149
0.5	0.5079	-0.0079
0.5	0.5070	-0.0070

Table 6.4: Sensorless Initial Rotor Position Estimation Performance, Repeated

6.5 Sensorless Speed Control

The experiments performed tested the SyncRM drive under a variety of conditions. Low, medium and full speed tests were performed and the results are presented in this Chapter. In most cases, the plot of the speed is presented for the sensorless case only since the sensed result was very similar. The position data presented in this Section is expressed as the cosine of the mechanical rotor position as this makes the data more observable.

One of the concerns that was highlighted during the simulation phase was the performance of the sensorless estimation algorithm at low speeds. The first test was therefore performed at low speed to observe what problems, if any might have to be overcome.

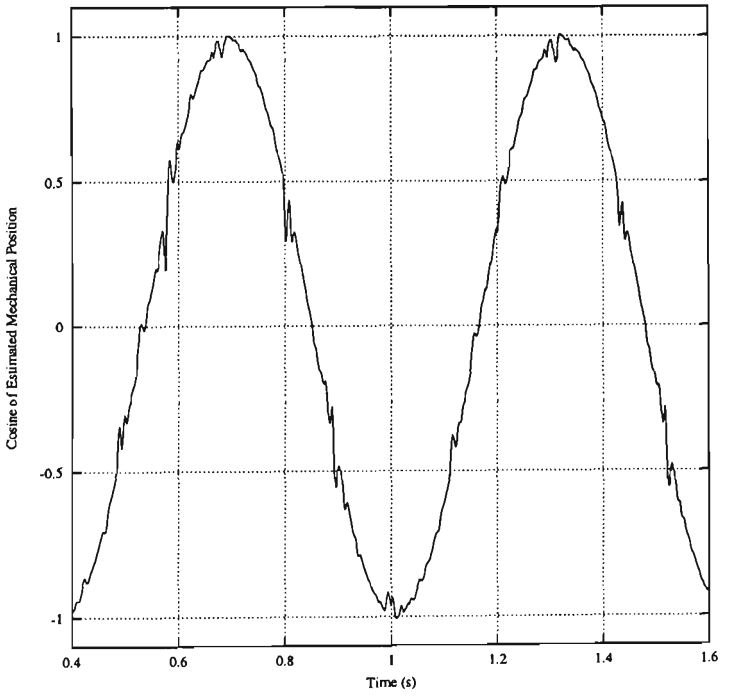

Figure 6.5: Cosine of Estimated Rotor Position, 10 rad/s

Figure 6.5 illustrates the output of the position estimation algorithm from the controller during a constant speed of 10 rad/s. In this Figure, the output is observed as the cosine of the estimated mechanical position. The result is a good quality estimate that is stable. Using this signal as part of the speed

estimation process means that the zero-crossings have to be at regular intervals (for the constant speed case) and be particularly "noise free" during the zero-crossing. Logic is in place to ensure that once a zero crossing is successfully detected, another one can take place for a small period of time. This additional filtering aids in ensuring a stable speed estimation.

Figure 6.6 illustrates the controller performance for a speed step to 10 rads/s followed by several reversals.

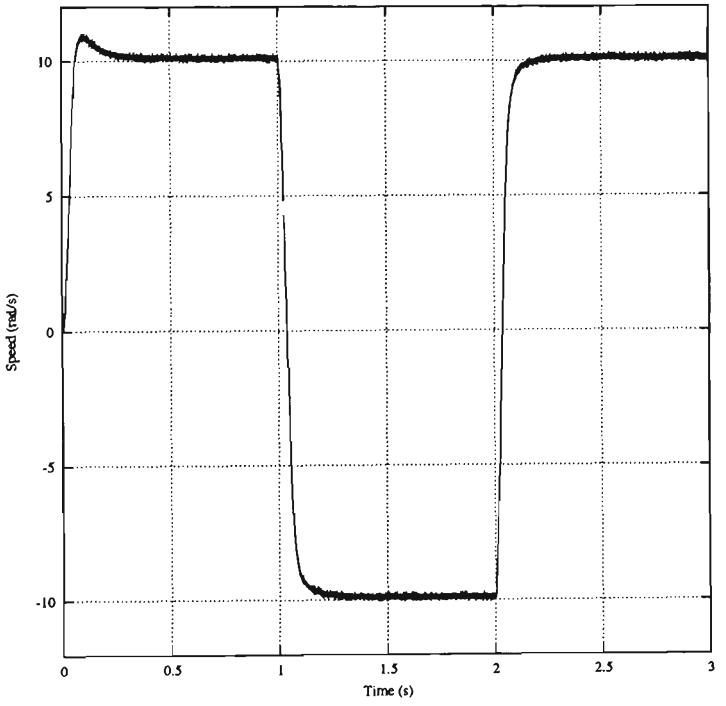

Figure 6.6: Speed Performance During ±10 Rads/s Reversal

The speed reversal is performed with no overshoot. It is also interesting to note what the q-axis current is doing during this time. Figure 6.7 illustrates the performance of the q-axis current. The control scheme implemented maintains a constant d-axis current of 5 amps.

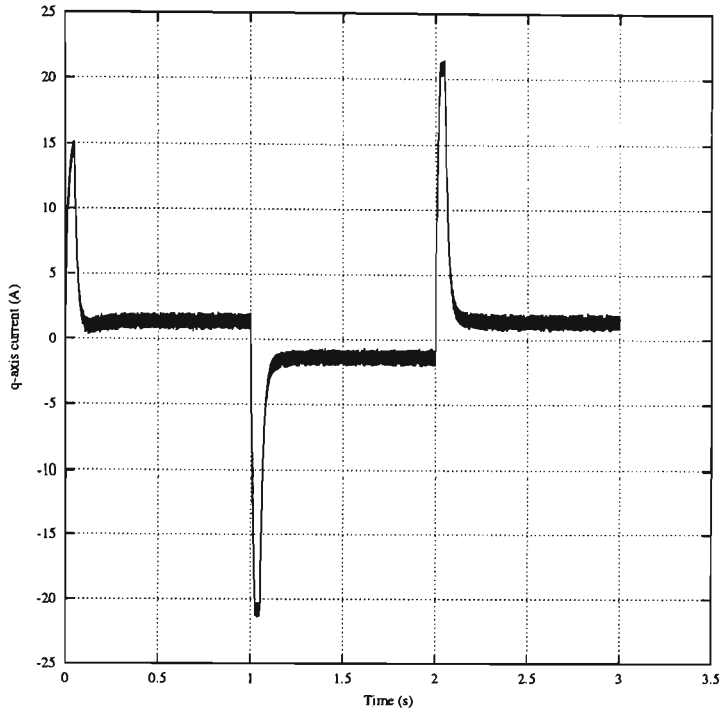

Figure 6.7: Q-axis Current During ±10 Rad/s Reversal

The next test was a speed step followed by a reversal at 26 rads/s. This represents approximately 250 RPM, or $\frac{1}{4}$ of the maximum speed of the drive. Figure 6.8 is a plot of the speed performance

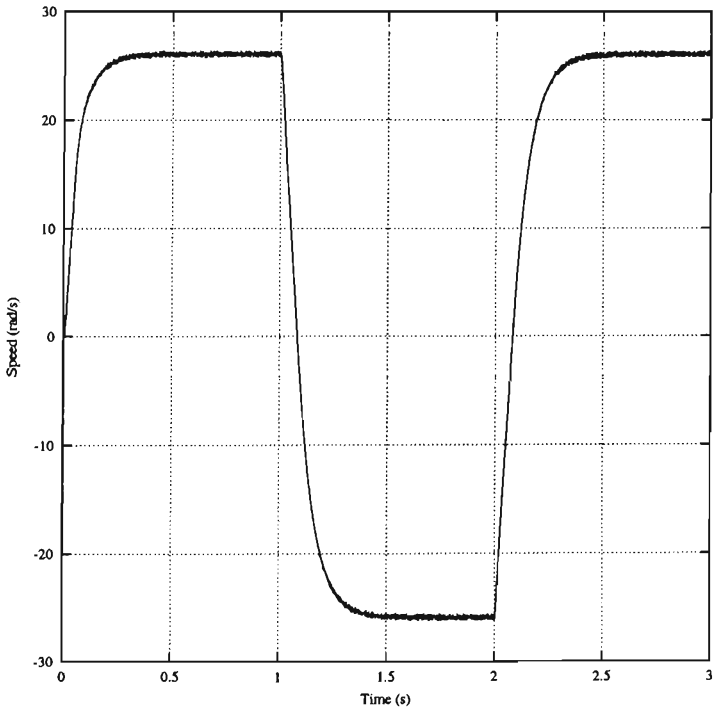

Figure 6.8: Speed Performance During ±26 Rad/s Reversal

Figure 6.9 is a plot of the q-axis current during the same test.

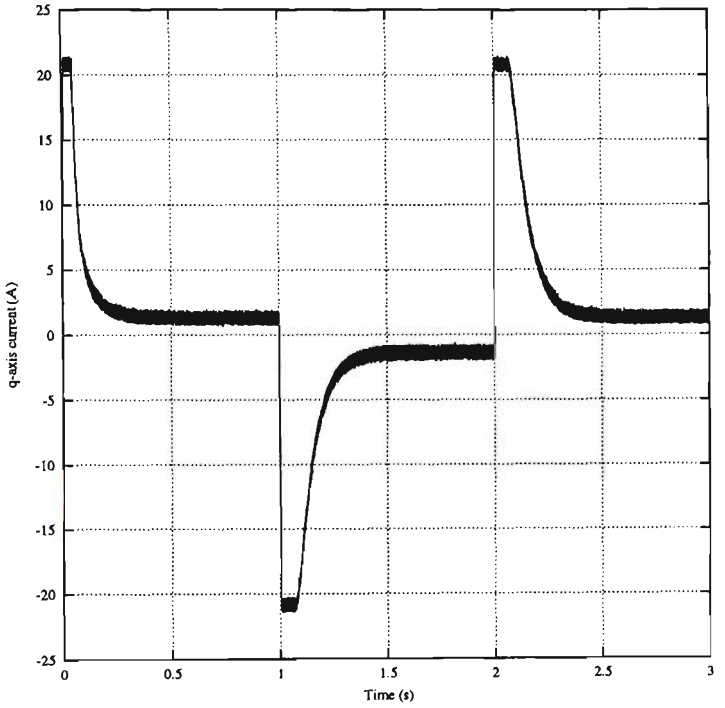

Figure 6.9: Q-axis Current During ±26 Rad/s Reversal

The q-axis current is accurately controlled. The output signal has high frequency switching noise embedded in it. Figure 6.10 is a plot of the d-axis current and Figure 6.11 illustrates the q-axis current setpoint during the same test.

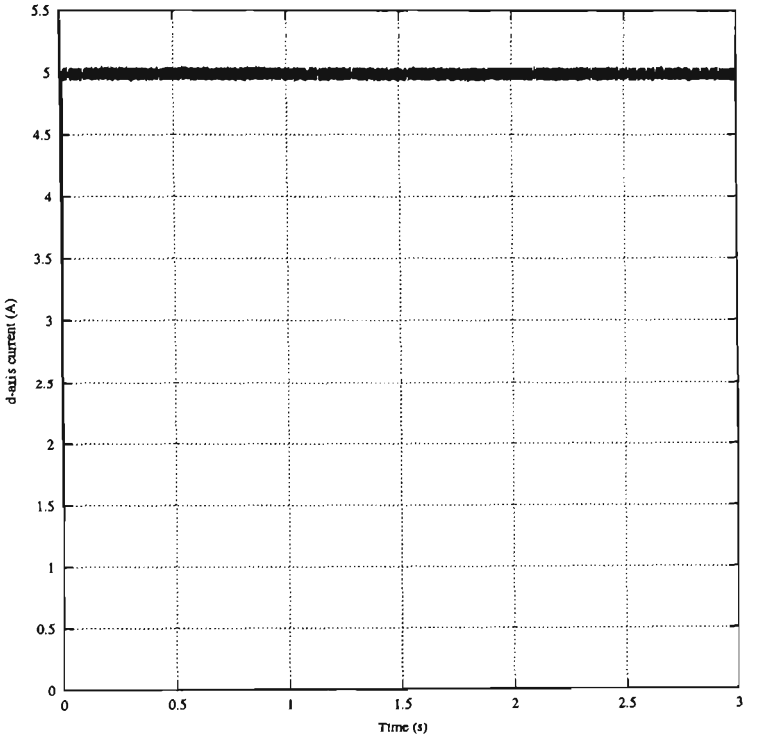

Figure 6.10: D-axis Current During ±26 Rad/s Reversal

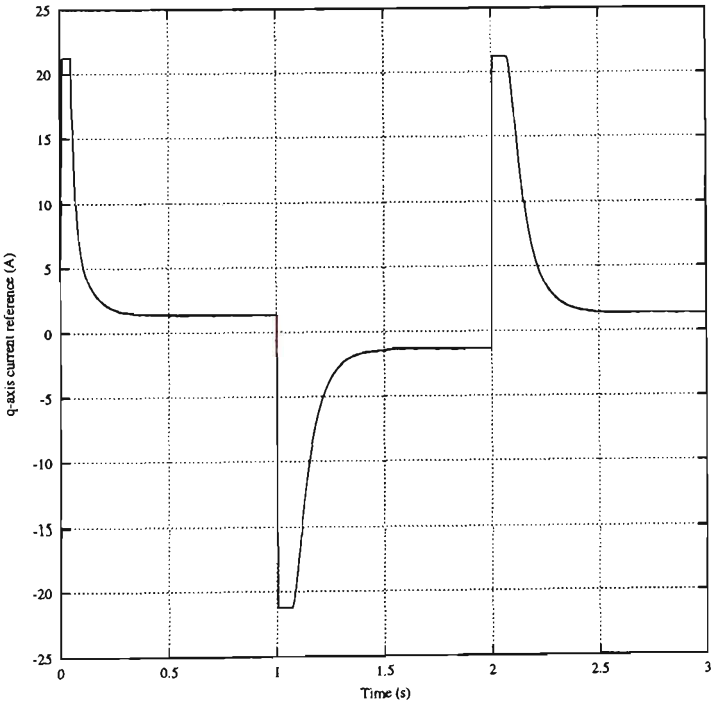

Figure 6.11: Q-axis Current Reference During ±26 Rad/s Reversal

It is also interesting to observe the position estimation output during a constant speed output of 26 rad/s. The position and speed estimate is clearly working as designed since the speed plots are smooth and stable. Figure 6.12

is a plot of the position estimator output and the actual position, derived from the shaft encoder.

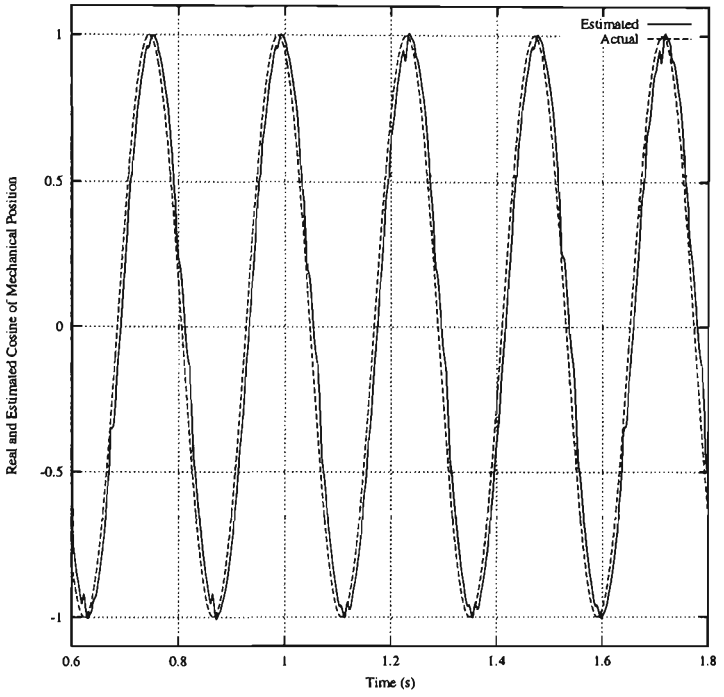

Figure 6.12: Cosine of the Real and Estimated Position at 26 Rad/s

The next two Figures, Figures 6.13 and 6.14, demonstrate the controller's ability to perform speed reversals at higher speeds. This time, a 52 rad/s speed reversal is performed. This is approximately 500 RPM, or $\frac{1}{2}$ of maximum speed.

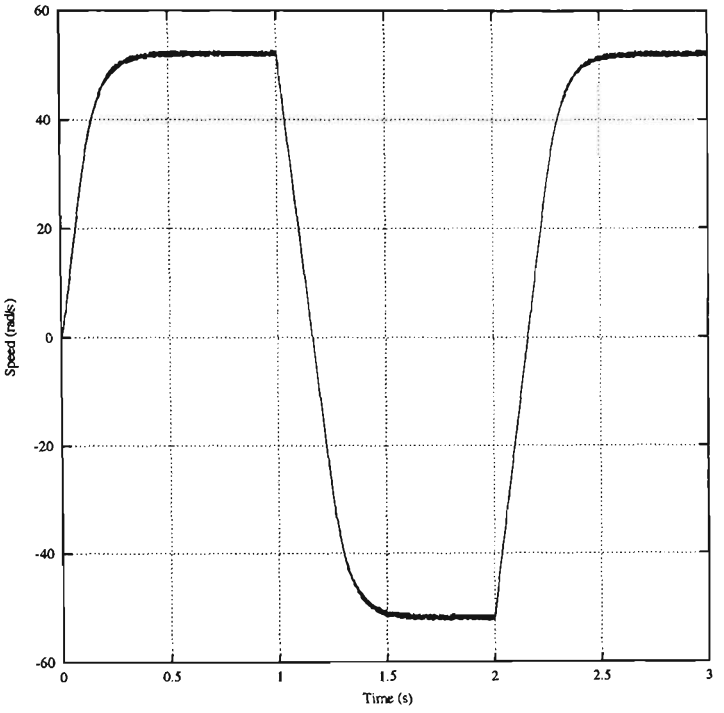

Figure 6.13: Speed Performance During ±52 Rad/s Reversal

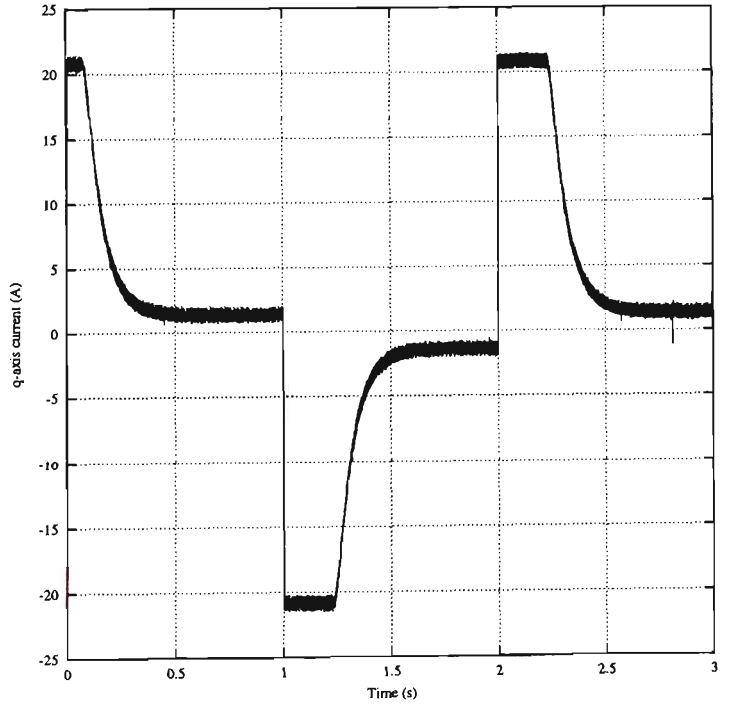

Figure 6.14: Q-axis Current During ±52 Rad/s Reversal

The process of obtaining data in real time is limited by the memory capabilities of the DSP board used as for the real time system. It does not have sufficient capacity to store vast amounts of data. Normally, data would need to

be stored to some other medium. During the experimentation phase, attempts were made to utilise the hard disk of the host computer as a place to store data as the SyncRM was being controlled. This was unsuccessful because writing to the host PC's hard disk compromised the DPS's ability to sustain a constant 5 kHz control loop. A consequence of this is that it is not possible to display the complete results of speed reversals at much higher speeds.

Figure 6.15 and 6.16 illustrate the performance of the controller in response to a step of 79 and 104 rad/s respectively. This represents 750 and 1000 RPM.

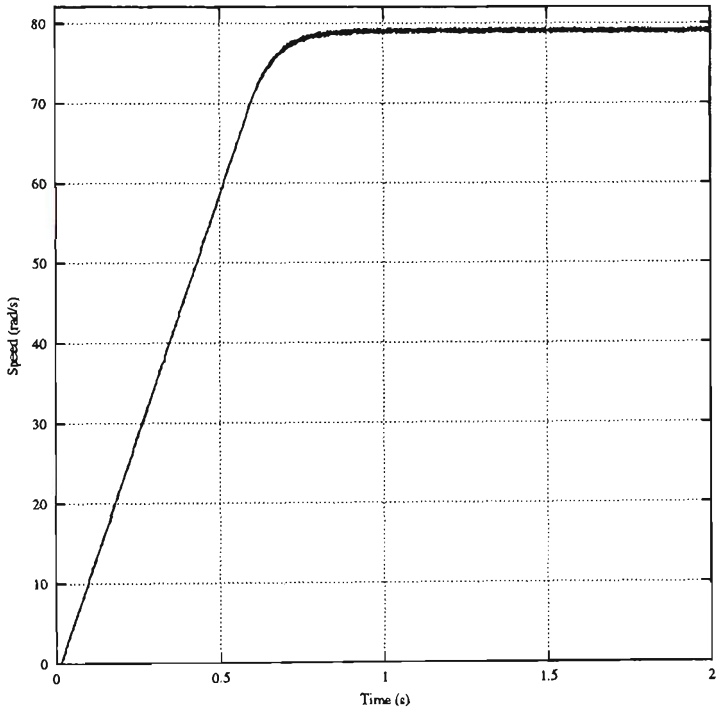

Figure 6.15: Speed Performance During ±79 Rad/s Step

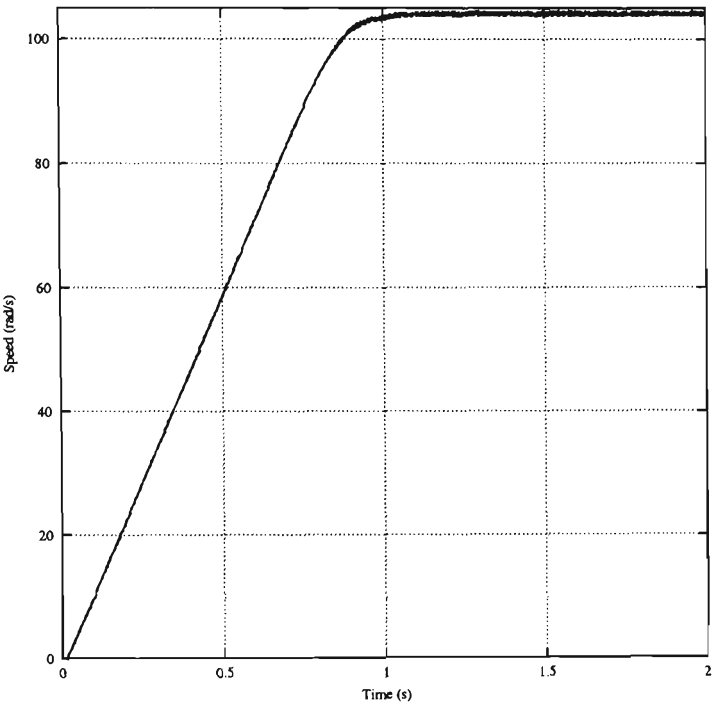

Figure 6.16: Q-axis Current During ±104 Rad/s Step

In the final plot, a 104 rad/s step is applied and the results for both sensor control and the sensorless control are graphed together.

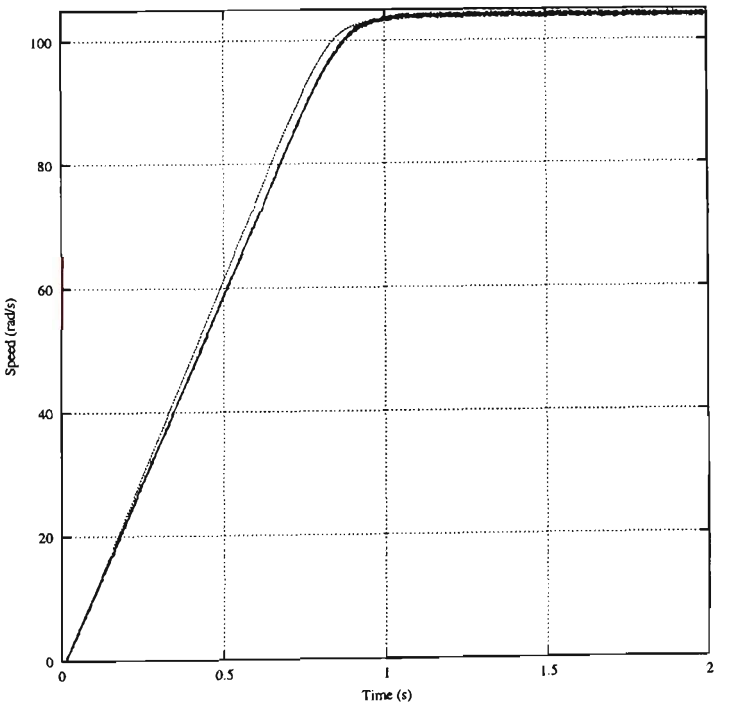

Figure 6.17: Speed Performance Comparison

In Figure 6.17, the slower of the two responses is that of the sensorless control case.

6.6 Conclusions

This section has presented the experimentation equipment used for testing the sensorless rotor position estimation algorithms. It has also provided a great variety of results showing the robustness of the algorithms. The 22 kW axially laminated synchronous reluctance motor was controlled over a wide speed range without the use of a shaft encoder quite effectively. It was observed that the dynamic response of the drive was of marginally less quality in the case of sensorless control compared to the control using a shaft encoder. This could be explained by the slight de-tuning of the PI control gains for the sensorless case. What amounts to a gain-scheduling was required to obtain the results reported.

The control scheme was tested under both transient and steady state conditions. In both cases, the performance was observed to be satisfactory. The following observations can be drawn from the results presented in this Chapter:

1. The initial position estimation algorithm works well and provides an acceptably small delay at the start. There is some slight variation in the real versus actual position characteristic using the proposed technique, but it is not significant enough to cause problems during the start up phase.

2. The sensorless controller produces good quality speed control with smooth accelerations under current limit. This was observed over a wide range of speeds.

3. The sensorless control scheme provides smooth control during speed reversals with little or no overshoot. The drive system was able to perform the reversals under controlled current conditions.

4. The measure q-axis current is quite noisy but it does not adversely effect

the control procedures. The statistical approach ensures that estimation is based on the average changes in current over several switching cycles.

5. The delay in calculating the rotor position because of the statistical approach does not result in a deterioration of performance of the drive system.

6. The inertia of the real drive system was larger than that used in the simulation study as is observed by the performance of both systems. This increase in inertia did not adversely effect the performance of the position estimation.

This Chapter's key outcome was the experimental verification of the new sensorless rotor position estimation for the Synchronous Reluctance Motor.

Chapter 7

Comments and Conclusions

7.1 Introduction

This thesis has considered the modelling and sensorless control of a synchronous reluctance motor. The two main goals of the work have been to develop a better understanding of the q-axis magnetic circuit and to develop a new sensorless rotor position detection scheme. These objectives have largely been achieved.

The motivation behind these two areas of research lie primarily in the many advantages that the Synchronous Reluctance Motor has over other members of the AC machine family. The inherent saliency of the axially laminated rotor make the machine an ideal candidate for sensorless rotor position detection. The vector control of an AC machine necessitates some form of rotor position feedback. If this can be achieved without the need for external sensors, then there are obvious advantages.

The vector controlled SyncRM has values of torque, output power and efficiency which are available with a better power factor and lower kVA rating for the supply inverter compared to the squirrel cage induction motor. All of this hinges on the proper design of the machine, hence the desire to understand the nature of one of the key magnetic circuits of the SyncRM.

This Chapter provides a summary of the work presented in this thesis. It outlines the key outcomes of the research and summarises the relevant contributions made to research SyncRM area of research. The next section outlines the future directions that the research may take. The final section provides the summary of this thesis.

7.2 Extensions and Comments

The work performed in this thesis has provided several key contributions to the body of knowledge associated with synchronous reluctance motors. Two key areas are the q-axis magnetic circuit modelling and the sensorless rotor position estimation. These contributions have the potential for further exploitation and development.

7.2.1 Magnetic Circuit Modelling

To be able to produce the best possible design for a reluctance motor, it is necessary to fully understand the magnetic circuits. The research performed in this thesis indicates that there is a component of the q-axis flux that zigzags its way through the rotor, effectively increasing the inductance of the q-axis. This has an adverse effect on the possibility of designing a machine with a high $\frac{L_d}{L_q}$ ratio. Future work in the area of rotor design should take this into account.

Rotor design optimisation should look at ways of reducing the zigzag flux effect when the laminations used in the rotor are relatively thin.

7.2.2 Sensorless Position Estimation

A new mechanism for rotor position estimation has been developed. It has been shown to work over a wide range of speeds. The algorithm has also been shown

to work accurately during periods of heavy acceleration and deceleration, whilst maintaining a high q-axis current value. This is effectively acceleration under current limit.

The hardware used for the experimental work was a highly customised commercial inverter, designed to be used for an induction motor drive. The switching elements in this inverter are not as high performance as devices that are available today. The switching elements, Insulated Gate Bipolar Transistors (IGBT) were only capable of switching frequencies of up to 5kHz. The gate drives were also part of the original commercial package. A consequence of using this package is that the experimental work was bound by the limitations of the inverter.

There is scope for further testing and development of the new sensorless scheme. This testing should be performed on a platform with more modern devices, capable of much higher switching frequencies. A purpose built device rather than a customised commercial unit would be the preferred hardware platform. This would alleviate some of the interfacing and reliability issues associated with the customisation process. The higher switching frequencies would certainly help in the accuracy of the algorithm for the low speed and light load case.

Another area that should be explored further is the performance of the new algorithms whilst the motor is being subject to higher, potentially more saturating (in the magnetic sense) loads. Since the algorithm relies on there being a difference between the L_d and L_q, heavy saturation would make this ratio smaller. The simulation work performed indicates that the algorithm is quite robust even down to low saliency ratios. Having a reliable hardware platform that would enable such testing to take place would first be necessary.

The experimental work in this thesis did not seek to find the optimal control mechanism for the reluctance motor utilising the new scheme. A simple PI vector control scheme was implemented. There is scope for further work in the

area of control of the SyncRM using more complex controllers capable of higher performance

7.3 Conclusions

A brief summary of the work presented in this thesis and the conclusions that can be drawn from the results are as follows.

1. **Chapter 1** provided a deeper insight into the motivations for this research. A brief history of the synchronous reluctance motor was provided. This Chapter also outlined the advantages that the SyncRM has over its AC counterparts. The thesis' major contributions were outlined as were a list of publications resulting from the research.

2. **Chapter 2** provided a review of the research that has been performed by other scientists and engineers on the SyncRM. The research reviewed was split into two areas; magnetic circuit modelling and sensorless rotor position detection. It discussed some of the methodologies used and highlighted some similarities and differences with the work presented in this thesis.

3. **Chapter 3** presented a detailed analysis of the q-axis magnetic circuit of a SyncRM. The concept of "zigzag" flux paths were introduced and a model presented that illustrates the existence of such flux paths. The key mathematical expressions describing the flux of the q-axis were also given. Appendix C provided the details behind the analyses. The Chapter also introduced the idea of the q-axis channel which represents what is essentially an expression for the q-axis reluctance, taking into account the effects of "zigzag" flux paths. The key conclusions made in this Chapter are;

   i. Q-axis flux paths do exist that "zigzag" between the rotor and the stator.

   ii. The q-axis can be modelled with a lumped reluctance value, if the "zigzag" paths are carefully modelled.

iii. The net effect of these stray flux paths is a reduction in the saliency ratio, particularly when the thickness of the laminations used in the rotor approach values close to 10% of the length of the stator tooth.

Using two different current distributions in the stator, results are obtained quantifying the values of flux, in particular the increase in the amount of flux found in the q-axis circuit when the rotor is misaligned.

4. **Chapter 4** devised a finite element model to confirm the analytical modelling performed. Unlike other FEM studies that have been reported in the literature, this study modelled a complete stator and rotor, searching for the proposed "zigzag" flux paths. The detailed FEM provided results that supported the equation derived for various flux densities from this analysis. The model was a two pole design. The analysis showed that the flux paths exist when the rotor is in the misaligned position. By observing the flux transversing the rotor under q-axis excitation it is possible to observe an increase in the value of this flux when the rotor is misaligned from the stator teeth. The major outcomes of this Chapter are;

   i. "Zig-zag" flux paths do exist and can be observed quite clearly.

   ii. The modelling performed in Chapter 3 was valid.

   iii. Modelling a complete rotor and stator combination rather than relying on the symmetry that a $\frac{1}{4}$ sized model has can provide a deeper insight into the fluxing of the complete machine.

5. **Chapter 5** introduced the sensorless rotor position detection algorithms. The development of the algorithm is presented in detail. The new algorithm does not depend on detailed knowledge of the magnetic parameters of the reluctance motor. The technique adopts a statistical approach, utilising recent values of stator phase currents to calculate the position of the rotor. Even though the performance of the algorithm improves as the saliency ratio of the machine increases, satisfactory performance can be obtained for quite low ratios.

The Chapter presented the results of a simulation designed to test the effectiveness of the method. A modified zero-crossing technique for calculating rotor speed from rotor position information was also derived. The simulation study also provided insight into how this method might perform. The simulation was able to emulate both the sensor and sensorless control of a reluctance machine. A simple approach to the control algorithms was adopted, with an emphasis on the performance of the sensorless position and speed estimation being the key objective. The simulation was written using the 'C' programming language. Using this approach, the body of the code that was used to estimate the rotor speed and position was able to be used for the practical implementation of the algorithms. The outcomes of this Chapter are;

i. A new method for estimating the position of the rotor for a synchronous reluctance motor was developed.

ii. The statistical method could be used without adversely effecting the dynamic performance of the machine.

iii. A detailed simulation study was able to confirm the viability of the proposed speed and position algorithms.

As part of the sensorless control strategy, a technique for calculating the position of the rotor at standstill was also developed and simulated.

6. **Chapter 6** discussed the real time implementation of the sensorless rotor position and speed estimation algorithms. The experimental work utilised a 6 pole, 22kW, axially laminated machine. The computing platform used for the experiments used a high performance digital signal processor and a highly customised 37kW inverter. Performance of the machine was recorded for both the sensorless and sensor controlled cases. The performance of the sensorless method was able to be directly compared to the sensor method.

   The experiment confirmed the validity of the estimation method for a variety of speeds, including standstill. It was observed that the performance of the method improved as the speed of the drive increased. Although the low

speed sensorless performance was acceptable, it was not of the same quality as the sensor case. This was predicted by the simulation work carried out in Chapter 5. Despite these results, the new method still proved to be robust and the drive was able to perform full speed reversals and accelerations under current limit conditions in a well controlled and stable manner. The main outcomes of this Chapter are;

i. The sensorless position estimation algorithm developed gives high accuracy estimates over a wide range of speeds.

ii. The quality of the position estimates can be used by a modified zero-crossing technique for speed estimation.

iii. Using a predetermined sequence of stator vectors, it is possible to determine the position of the rotor at standstill and use this estimate to start the motor.

The simple PI algorithms utilised were adequate for testing the accuracy of the estimation techniques.

In conclusion, this thesis has presented a new method for modelling the q-axis magnetic circuit of a synchronous reluctance machine. It has provided a simple set of equations that accurately estimate the flux levels of the q-axis from the physical parameters of the motor. The thesis presents a detailed finite element analysis to validate the analytical modelling and clearly identify the existence of a "zigzag" flux. This modelling provides much more detail than other methods reported in the literature.

In addition to this high level modelling, this thesis also provided a new sensorless rotor position and speed estimation technique. The method is unique, being mathematically elegant and based on a statistical approach. It was experimentally confirmed that the technique works well for all speeds including standstill.

Appendix A

Glossary

This Appendix contains a list of symbols used throughout the text.

J	Current Density, amps/metre
Φ_q	Q-axis magnetic flux, weber
$\Re_q$	Q-axis reluctance, amps/weber/metre
θ_m	Mechanical angle, radians
θ, θ_e	Electrical angle, radians
θ_p	Pole Arc angle, radians
μ_o	Permeability constant, $4\pi \times 10^{-7}$ amps/metre
g	Airgap, mm
g_e	Equivalent airgap, mm
R	Stator radius, mm
L_R	Rotor stack length, mm
p	Pole pairs
$\Re_l$	Leakage Reluctance, amps/weber/metre
K_{c1}	Carter's Coefficient
K_{c2}	Carter's Coefficient
$\Re$	Reluctance amps/weber
A_s	Surface Area of Tooth Face, mm^2

L_s	Stator Stack Length, mm
N_s	Number of Slots per Pole Pair
$\Re_{G1}$	Airgap Reluctance, amps/weber
$\Re_{G2}$	Airgap Reluctance, amps/weber
l_{sp}	Slot Pitch Length, mm
t_m	Thickness of Magnetic Rotor Lamination, mm
d_{nm}	Thickness Non-magnetic Rotor Lamination, mm
A_{rl}	Cross Sectional Are of Rotor, mm^2
K_a	Magnetic to Non-Magnetic Ratio

Appendix B

Motor Parameters

This Appendix presents the details of the motor used by the Finite Element Model. It is the same motor that was used in some of the early experimental work by Bowman *et. al.* on sensorless rotor position estimation (Bowman and Platt, 1993).

Table B.1 is an abbreviated list of the physical parameters of the modelled machine. The quantities that were used during the modelling process are presented.

Parameter	Value	Parameter	Value
Rotor Radius	41.15mm	Stator (inner) Radius	41.3mm
Stator Length	46.1mm	Rotor Length	44.8mm
No. Stator Slots	24	Pole Pairs	1
Air Gap	0.25mm	K_a	0.5

Table B.1: SyncRM Physical Parameters

The quantity K_a is the ratio of the thicknesses of magnetic to non-magnetic material in the rotor. The Stator Radius is defined as the inner radius. That is, the radius from the pole face to the axis of rotation. Figure B.1 is an illustration showing some of the physical attributes of the stator slot.

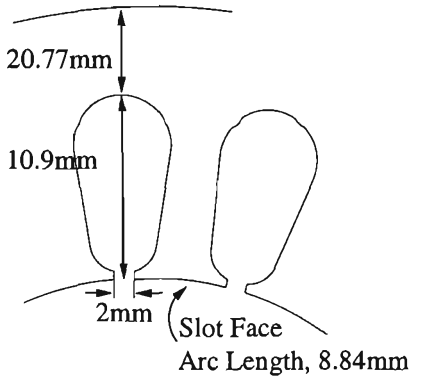

Figure B.1: Stator Slot Parameters

This isn't a scale illustration of the slot geometry, just one designed to show the more important features.

Appendix C

Magnetic Circuit Modelling Detail

C.1 Introduction

In Chapter 3, the basics of the magnetic circuit modelling were presented. The detailed mathematics associated with that modelling were omitted for the sake of clarity. This Appendix fills that gap by including the mathematical detail. The section headings used in this Appendix are identical to those in Chapter 3.

The detailed analysis is important since is reveals the nature by which the final expressions were developed. The assumptions and the results of the assumptions are given.

C.2 General Solution for Q-Axis Flux

In Chapter 3, Section 3.4, an expression for the general solution of the q-axis flux is given. This section is a short derivation of this expression. First, equation (3.16) is rearranged.

$$\frac{p}{RL_R}\frac{d\Phi_q}{d\theta} - B_g(\pi-\theta) + B_g(\theta) = 0 \tag{C.1}$$

Equation (3.17) is also rearranged.

$$\frac{\mu_o R}{pg_e}\int_{\theta}^{\pi-\theta} J(\theta)d\theta - B_g(\theta) + B_g(\pi-\theta) = 0 \tag{C.2}$$

If (C.1) is subtracted from (C.2), the the following expression is obtained.

$$\frac{\mu_o R}{pg_e}\int_{\theta}^{\pi-\theta} J(\theta)d\theta - \frac{p}{RL_R}\frac{d\Phi_q}{d\theta} - 2B_g(\theta) = 0 \tag{C.3}$$

Equation (C.3) can be integrated then directly differentiated without finding the solution to the integral. Such an action results in this expression.

$$\frac{\mu_o R}{pg_e}[-J(\pi-\theta) - J(\theta)] + \frac{p}{RL_R}\frac{d^2\Phi_q}{d\theta^2} - \frac{2dB_g(\theta)}{d\theta} = 0 \tag{C.4}$$

If (3.14) is rearranged an expression for $\frac{dB(\theta)}{d\theta}$ is obtained.

$$\frac{dB_g(\theta)}{d\theta} = \frac{\mu_o R}{pg_e}[\Re_q\Phi_q - J(\theta)] \tag{C.5}$$

Now, equation (C.5) can be substituted into (C.4) to obtain the following.

$$\frac{\mu_o R}{pg_e}[-J(\pi-\theta) - J(\theta)] + \frac{p}{RL_R}\frac{d^2\Phi_q(\theta)}{d\theta^2} - \frac{2\mu_o R}{pg_e}[\Re_q\Phi_q - J(\theta)] = 0 \tag{C.6}$$

Rearrangement and simplification of (C.6) leads the final result.

$$\frac{d^2\Phi_q(\theta)}{d\theta^2} - \frac{2\mu_o R^2 L_R}{p^2 g_e}\Phi_q(\theta) + \frac{\mu_o R^2 L_R}{p^2 g_e}[J(\theta) - J(\pi-\theta)] = 0 \tag{C.7}$$

The reader should now return to Chapter 3, Section 3.4.

C.3 Slot Leakage Reluctance

This section should be read in conjunction with Section 3.5 in Chapter 3. The aim of this analysis is to produce an expression for the equivalent slot leakage reluctance, $\Re_l$. The value for $\Re_l$ is a quantity that represents the reluctance of a "reluctance channel" and has the units of A/Wb/m of airgap. Reference is made to Figure 3.9 in the main body.

The first section of interest is the rectangular section bounded by W and L in Figure 3.9. In this section, the currently is uniformly distributed in the slot such that

$$J = \frac{I}{WL}. \tag{C.8}$$

The total MMF enclosed by the closed loop is

$$MMF = JWl. \tag{C.9}$$

This value for enclosed MMF must be equal to the MMF dropped by flux crossing the slot

$$MMF = HW. \tag{C.10}$$

where H is the magnetic field intensity. By equating this expression with the well known relationship $B = \mu_o H$ and substituting equation (C.9), we obtain

$$B = \frac{\mu_o Il}{WL}. \tag{C.11}$$

Now, the total flux enclosed in the slot is

$$\Phi = \int_0^L BL_s \, dl. \tag{C.12}$$

where L_s represents the length of the stator stack. Solution of this integral leads

to

$$\Phi = \frac{\mu_o I L_s L}{2W}. \tag{C.13}$$

Since reluctance is defined by flux and magnetomotive force, an expression for reluctance is found by substitution and leads to

$$\Re_{l1} = \frac{2W}{\mu_o L_s L}. \tag{C.14}$$

To include the effects of the trapezoidal opening of the slot, consider the MMF in this area given by

$$MMF = H\left(W - \frac{2lW_t}{T}\right). \tag{C.15}$$

Once again an expression for B is found by substituting equation (C.15) into $B = \mu_o H$ and simplifying to get

$$B = \frac{\mu_o I T}{WT - 2lW_t}. \tag{C.16}$$

The total flux enclosed by the tooth tip uses equation (C.12) except that l traverses the region indicated by parameter T

$$\Phi = \int_0^T B L_s \, dl. \tag{C.17}$$

Solution of this integral leads to an expression for the flux in the tooth tip area

$$\Phi = \frac{\mu_o I T L_s}{2W_t}\left[\ln\left(1 - \frac{2W_t}{W}\right)\right]. \tag{C.18}$$

Finally, the expression for reluctance in this area can be expressed as

$$\Re_{l2} = \frac{-2W_t}{\mu_o L_s T\left[\ln\left(1 - \frac{2W_T}{W}\right)\right]}. \tag{C.19}$$

The complete expression for slot leakage reluctance as used in this analysis is

found by combining C.19 and C.14 as a parallel circuit.

$$\Re_l = \left(\frac{1}{\Re_{l1}} + \frac{1}{\Re_{l2}} \right)^{-1} \tag{C.20}$$

The reader should now return to 3.5 in Chapter 3.

C.4 Sinusoidal Current Distribution

This section should be read in conjunction with Section 3.8 in Chapter 3. The aim of this section is to derive expressions for q-axis flux, airgap flux density, tooth and yoke flux densities for a sinusoidal distribution of stator current.

C.4.1 The Q-Axis Flux

The expression for the q-axis flux of the reluctance motor was given in Chapter 3 as the solution to

$$\frac{d^2\Phi_q(\theta)}{d\theta^2} - b\Phi_q(\theta) + c[J(\theta) - J(\pi - \theta)] = 0 \tag{C.21}$$

Sinusoidal current distribution can be described by the expressions

$$J(\theta) = J_q \cos\theta - J_d \sin\theta. \tag{C.22}$$

Equation C.21 requires and expression for both $J(\theta)$ and $J(\pi - \theta)$.

$$J(\pi - \theta) = -J_q \cos\theta - J_d \sin\theta \tag{C.23}$$

$$J(\theta) - J(\pi - \theta) = 2J_q \cos\theta \tag{C.24}$$

For the given current distribution, equation C.21 is written as

$$\frac{d^2\Phi_q}{d\theta^2} - b\Phi_q + 2cJ_q \cos\theta = 0. \tag{C.25}$$

Equation C.25 is a linear, non-homogeneous differential equation that can be solved by the method of undetermined coefficients. It has a general solution

$$\Phi_q = Ae^{\gamma\theta} + Be^{-\gamma\theta} \tag{C.26}$$

where

$$\gamma = \sqrt{b}. \tag{C.27}$$

A particular solution to equation C.26 can be found by letting $\Phi_q(\theta) = K\cos\theta + L\sin\theta$. i.e.

$$\Phi_q = K\cos\theta + L\sin\theta$$
$$\Phi_q' = -K\sin\theta + L\cos\theta$$
$$\Phi_q'' = -K\cos\theta - L\sin\theta$$

Substituting these expressions into equation C.25 results in

$$-K\cos\theta - L\sin\theta - b(K\cos\theta + L\sin\theta) = -2cJ_q\cos\theta$$
$$-\cos\theta(K + bK) - \sin\theta(L + bL) = -2cJ_q\cos\theta$$

Collecting like terms and equating leads to

$$L = 0$$
$$K = \frac{2cJ_q}{b+1}$$

Therefore the solution to equation C.25 is

$$\Phi_q(\theta) = Ae^{\gamma\theta} + Be^{-\gamma\theta} + \frac{2cJ_q\cos\theta}{b+1} \tag{C.28}$$

The next step in the solution is determining values for the coefficients, A and B in equation C.28. In order to do this, first seek a relationship between these two coefficients. If equation C.22 is substituted in equation (3.17) the result is

$$\frac{R}{p}\int_{\theta}^{\pi-\theta}[J_q\cos\theta - J_d\sin\theta]\,d\theta - \frac{g_e}{\mu_o}[B_g(\theta) + B_g(\pi-\theta)] = 0 \tag{C.29}$$

$$\frac{R}{p}[J_q\sin\theta + J_d\cos\theta]_{\theta}^{\pi-\theta} - \frac{g_e}{\mu_o}[B_g(\theta) + B_g(\pi-\theta)] = 0 \tag{C.30}$$

$$\frac{R}{p}[J_q\sin(\pi-\theta) + J_d\cos(\pi-\theta) - J_q\sin\theta - J_d\cos\theta] - \frac{g_e}{\mu_o}[B_g(\theta) + B_g(\pi-\theta)] = 0 \tag{C.31}$$

$$\frac{2\mu_o R J_d\cos\theta}{pg_e} + B_g(\theta) + B_g(\pi-\theta) = 0 \tag{C.32}$$

Rearrangement of equation (3.16);

$$\frac{p}{RL_R}\frac{d\Phi_q}{d\theta} - B_g(\pi-\theta) + B_g(\theta) = 0 \tag{C.33}$$

With these two equations in hand, expressions for $B_g(\theta)$ and $B_g(\pi-\theta)$ can be obtained. This is done by firstly adding equations C.32 and C.33 and then subtracting the same two equations.

$$B_g(\theta) = -\frac{1}{2}\left[\frac{p}{RL_R}\frac{d\Phi_q}{d\theta} + \frac{2\mu_o R J_d\cos\theta}{pg_e}\right] \tag{C.34}$$

$$B_g(\pi-\theta)=\frac{1}{2}\left[\frac{p}{RL_R}\frac{d\Phi_q}{d\theta}-\frac{2\mu_o RJ_d\cos\theta}{pg_e}\right] \tag{C.35}$$

Now, if at $\theta=0$ we assume that $B_g(\theta)=B_g(\pi-\theta)$ if $J_d=0$. Differentiating equation C.28 and letting $\theta=0$

$$\Phi_q'=\gamma A-\gamma B \tag{C.36}$$

This result is now substituted into C.34 and C.35 to obtain

$$B_g(\theta)=-\frac{1}{2}\left[\frac{p}{RL_R}(\gamma A-\gamma B)+\frac{2\mu_o RJ_d\cos\theta}{pg_e}\right]$$
$$B_g(\pi-\theta)=\frac{1}{2}\left[\frac{p}{RL_R}(\gamma A-\gamma B)-\frac{2\mu_o RJ_d\cos\theta}{pg_e}\right]$$

Equating these two expressions

$$-\frac{1}{2}\left[\frac{p}{RL_R}(\gamma A-\gamma B)\right]=\frac{1}{2}\left[\frac{p}{RL_R}(\gamma A-\gamma B)\right] \tag{C.37}$$

leads to

$$\frac{2p}{RL_R}(\gamma A-\gamma B)=0 \tag{C.38}$$

Equation C.38 is true, if and only if $A=B$. Thus, the solution, equation C.28, becomes

$$\Phi_q(\theta)=A(e^{\gamma\theta}+e^{-\gamma\theta})+\frac{2cJ_q\cos\theta}{b+1} \tag{C.39}$$

At this stage, the next requirement is to find an expression for the constant A. There are two methods of approaching this problem. In the first instance the assumption that at $\theta=\frac{\theta_p}{2}$ $\Phi_q=0$. This is the extremity of the pole. Ideally, the entire pole flux is contained wholly within the pole face. However, practically,

this is not the case. Within the analysis provided here, the two cases are differentiated by the expressions, "Including Pole Side Flux" and "Neglecting Pole Side Flux".

Neglecting Pole Side Flux

In the case where $\Phi_q = 0$ at $\theta = \frac{\theta_p}{2}$, firstly rewrite C.39

$$A(e^{\gamma\frac{\theta_p}{2}} + e^{-\gamma\frac{\theta_p}{2}}) + \frac{2cJ_q \cos\frac{\theta_p}{2}}{b+1} = 0 \tag{C.40}$$

This leads to the value of A to be

$$A = \frac{-2cJ_q \cos\frac{\theta_p}{2}}{(b+1)(e^{\gamma\frac{\theta_p}{2}} + e^{-\gamma\frac{\theta_p}{2}})} \tag{C.41}$$

Including Pole Side Flux

Referring to Figure 3.11 in the main body of the text, the total MMF enclosed by the loop which passes all the way along the q-axis and returns via the yoke, is given by the expression

$$MMF = \int_{\frac{-\theta_p}{2}}^{\frac{\theta_p}{2}} H_q R\frac{d\theta}{p} + 2\Phi_q\left(\frac{\theta_p}{2}\right)\Re_{side} \tag{C.42}$$

The reluctance equations relevant to this model are;

$$\begin{aligned} F &= \Phi\Re \\ H_q R\frac{d\theta}{p} &= dF_q \\ dF_q &= \Phi_q\Re_q R\frac{d\theta}{p} \\ H_q &= \Phi_q\Re_q \end{aligned} \tag{C.43}$$

Thus, equation C.42 becomes;

$$MMF = \int_{\frac{-\theta_p}{2}}^{\frac{\theta_p}{2}} \Phi_q \Re_q R \frac{d\theta}{p} + 2\Phi_q \left(\frac{\theta_p}{2}\right) \Re_{side} \tag{C.44}$$

Equation C.44 states that the total MMF enclosed by the loop defined in Figure 3.11 is made of two contributing components; the 0 and pole side contributions. The pole side contribution assumes a constant Φ_q across the pole side region.

Now, over the entire path ($\frac{\pi}{2}$ to $\frac{-\pi}{2}$), for sinusoidal current distribution,

$$\begin{aligned}
MMF &= \int_{\frac{-\pi}{2}}^{\frac{\pi}{2}} (J_q \cos\theta - J_d \sin\theta) \frac{Rd\theta}{p} \\
MMF &= \frac{R}{p} [J_q \sin\theta + J_d \cos\theta]_{\frac{-\pi}{2}}^{\frac{\pi}{2}} \\
MMF &= \frac{R}{p} \left[J_q \sin\frac{\pi}{2} + J_d \cos\frac{\pi}{2} - J_q \sin\frac{-\pi}{2} - J_d \cos\frac{-\pi}{2} \right] \\
MMF &= \frac{2RJ_q}{p}
\end{aligned} \tag{C.45}$$

Thus, we can now write the expression;

$$\frac{2RJ_q}{p} = \int_{\frac{-\theta_p}{2}}^{\frac{\theta_p}{2}} \Phi_q \Re_q R \frac{d\theta}{p} + 2\Phi_q \left(\frac{\theta_p}{2}\right) \Re_{side} \tag{C.46}$$

There already exists an expression for Φ_q, equation C.39. This equation is substituted into the expression C.46.

$$\begin{aligned}
2RJ_q = \int_{\frac{-\theta_p}{2}}^{\frac{\theta_p}{2}} \left[A(e^{\gamma\theta} + e^{-\gamma\theta}) + \frac{2cJ_q \cos\theta}{b+1} \right] \Re_q R d\theta + \\
2p\Re_{side} \left[A(e^{\gamma\frac{\theta_p}{2}} + e^{-\gamma\frac{\theta_p}{2}}) + \frac{2cJ_q \cos\frac{\theta_p}{2}}{b+1} \right]
\end{aligned} \tag{C.47}$$

$$2RJ_q = \Re_q R \left[\frac{A}{\gamma}(e^{\gamma\theta} - e^{-\gamma\theta}) + \frac{2cJ_q \sin\theta}{b+1} \right]_{\frac{-\theta_p}{2}}^{\frac{\theta_p}{2}} + 2p\Re_{side} \left[A(e^{\gamma\frac{\theta_p}{2}} + e^{-\gamma\frac{\theta_p}{2}}) + \frac{2cJ_q \cos\frac{\theta_p}{2}}{b+1} \right] \quad \text{(C.48)}$$

$$2RJ_q = \Re_q R \left[\frac{A}{\gamma}(e^{\gamma\frac{\theta_p}{2}} - e^{-\gamma\frac{\theta_p}{2}}) + \frac{2cJ_q \sin\frac{\theta_p}{2}}{b+1} \right] - \Re_q R \left[\frac{A}{\gamma}(e^{-\gamma\frac{\theta_p}{2}} - e^{\gamma\frac{\theta_p}{2}}) - \frac{2cJ_q \sin\frac{-\theta_p}{2}}{b+1} \right] + 2p\Re_{side} \left[A(e^{\gamma\frac{\theta_p}{2}} + e^{-\gamma\frac{\theta_p}{2}}) + \frac{2cJ_q \cos\frac{\theta_p}{2}}{b+1} \right] \quad \text{(C.49)}$$

$$2RJ_q = \Re_q R \left[\frac{2A}{\gamma}(e^{\gamma\frac{\theta_p}{2}} - e^{-\gamma\frac{\theta_p}{2}}) + \frac{4cJ_q \sin\frac{\theta_p}{2}}{b+1} \right] + 2p\Re_{side} \left[A(e^{\gamma\frac{\theta_p}{2}} + e^{-\gamma\frac{\theta_p}{2}}) + \frac{2cJ_q \cos\frac{\theta_p}{2}}{b+1} \right] \quad \text{(C.50)}$$

$$2RJ_q = \frac{2A\Re_q R}{\gamma}(e^{\gamma\frac{\theta_p}{2}} - e^{-\gamma\frac{\theta_p}{2}}) + \frac{4c\Re_q RJ_q \sin\frac{\theta_p}{2}}{b+1} + 2pA\Re_{side}(e^{\gamma\frac{\theta_p}{2}} + e^{-\gamma\frac{\theta_p}{2}}) + \frac{4p\Re_{side}cJ_q \cos\frac{\theta_p}{2}}{b+1} \quad \text{(C.51)}$$

$$2RJ_q = 2A \left[\frac{\Re_q R}{\gamma}(e^{\gamma\frac{\theta_p}{2}} - e^{-\gamma\frac{\theta_p}{2}}) + p\Re_{side}(e^{\gamma\frac{\theta_p}{2}} + e^{-\gamma\frac{\theta_p}{2}}) \right] + \frac{4cJ_q}{b+1} \left[\Re_q R \sin\frac{\theta_p}{2} + p\Re_{side} \cos\frac{\theta_p}{2} \right] \quad \text{(C.52)}$$

Simplifying,

$$A = \frac{RJ_q - \frac{2cJ_q}{b+1}\left[\Re_q R \sin\frac{\theta_p}{2} + p\Re_{side}\cos\frac{\theta_p}{2}\right]}{\frac{\Re_q R}{\gamma}(e^{\gamma\frac{\theta_p}{2}} - e^{-\gamma\frac{\theta_p}{2}}) + p\Re_{side}(e^{\gamma\frac{\theta_p}{2}} + e^{-\gamma\frac{\theta_p}{2}})} \tag{C.53}$$

Further simplification leads to the final result,

$$A = \frac{\gamma}{b+1}\frac{RJ_q(b+1) - 2cJ_q\left[\Re_q R \sin\frac{\theta_p}{2} + p\Re_{side}\cos\frac{\theta_p}{2}\right]}{\Re_q R(e^{\gamma\frac{\theta_p}{2}} - e^{-\gamma\frac{\theta_p}{2}}) + p\gamma\Re_{side}(e^{\gamma\frac{\theta_p}{2}} + e^{-\gamma\frac{\theta_p}{2}})} \tag{C.54}$$

If in equation C.54, $\Re_{side} \to \infty$, then the expression for A becomes the same as that previously derived and given by equation C.41

C.4.2 Tooth and Yoke Flux Density

If the expression for current distribution, equation (3.30), is substituted into equation (3.25),

$$\Phi_l = \frac{J_q \cos\theta - J_d \sin\theta}{\Re_l} \tag{C.55}$$

Differentiating this result leads to

$$\frac{d\Phi_l}{d\theta} = \frac{1}{\Re_l}(-J_q \sin\theta + J_d \cos\theta) \tag{C.56}$$

Also, from equation (3.27)

$$\frac{d\Phi_l}{d\theta} = \frac{RL_s}{p}(B_g - B_t) \tag{C.57}$$

Thus,

$$\frac{1}{\Re_l}(-J_d \sin\theta + J_d \cos\theta) = \frac{RL_s}{p}(B_g - B_t) \tag{C.58}$$

Such that,

$$B_t(\theta) = B_g(\theta) + \frac{p(J_q \sin\theta - J_d \cos\theta)}{\Re_l R L_s} \tag{C.59}$$

The complete expression for $B_t(\theta)$ becomes

$$B_t(\theta) = -\frac{1}{2}\left[\frac{p}{RL_R}\left(\gamma A\left(e^{\gamma\theta} - e^{-\gamma\theta}\right) - \frac{2cJ_q \sin\theta}{b+1}\right) + \frac{2\mu_o R J_d \cos\theta}{p g_e}\right] + \frac{p(J_q \sin\theta - J_d \cos\theta)}{\Re_l R L_s} \tag{C.60}$$

The reader should return to Section 3.8 in Chapter 3.

C.5 Rectangular Current Distribution

This section should be read in conjunction with Section 3.9 in Chapter 3. The aim of this section is to derive expressions for q-axis flux, airgap flux density, tooth and yoke flux densities for a rectangular distribution of stator current.

C.5.1 The Q-Axis Flux

In this case, $J_q(\theta) = J_q$, a constant. Since the interest lies primarily in the q-axis flux, J_d can be assumed to be 0. Since J_q is no longer a function of θ, but rather a constant, then equation (3.20) can be re-written as

$$\frac{d^2\Phi_q(\theta)}{d\theta^2} - b\Phi_q(\theta) + 2cJ_q = 0 \tag{C.61}$$

In this case, J_q is simply some constant value with the units amperes/metre.

Once again, as was for the sinusoidal case, this equation can be solved using the method of undetermined coefficients. The solution is given by

$$\Phi_q(\theta) = Ae^{\gamma\theta} + Be^{-\gamma\theta} + \frac{2cJ_q}{b} \tag{C.62}$$

The next step requires the values for the constants A and B to be determined. This cannot be performed directly. Firstly, the relationship between these constants must be examined. In order to do so, the expressions for airgap flux density need to be investigated. Consider a modified version of the d-axis MMF loop equation, equation (3.17) previously presented.

$$\int_{\theta}^{\frac{\theta_p}{2}} J_q(\theta)R\frac{d\theta}{p} + \int_{\pi-\frac{\theta_p}{2}}^{\pi-\theta} -J_q(\theta)R\frac{d\theta}{p} + \int_{\frac{\theta_p}{2}}^{\pi-\frac{\theta_p}{2}} J_d(\theta)R\frac{d\theta}{p} - \frac{g_e}{\mu_o}[B_g(\theta) + B_g(\pi-\theta)] = 0 \tag{C.63}$$

Since J_q is a constant, equation C.63 becomes;

$$\frac{RJ_q}{p}\int_{\theta}^{\frac{\theta_p}{2}} d\theta - \frac{RJ_q}{p}\int_{\pi-\frac{\theta_p}{2}}^{\pi-\theta} d\theta + \frac{RJ_d}{p}\int_{\frac{\theta_p}{2}}^{\pi-\frac{\theta_p}{2}} d\theta - \frac{g_e}{\mu_o}[B_g(\theta) + B_g(\pi-\theta)] = 0 \tag{C.64}$$

$$\frac{RJ_q}{p}\left[\frac{\theta_p}{2} - \theta\right] - \frac{RJ_q}{p}\left[\pi - \theta - \pi - \frac{\theta_p}{2}\right] + \frac{RJ_d}{p}\left[\pi - \frac{\theta_p}{2} - \frac{\theta_p}{2}\right] - \frac{g_e}{\mu_o}[B_g(\theta) + B_g(\pi-\theta)] = 0 \tag{C.65}$$

$$\frac{RJ_d}{p}[\pi - \theta_p] - B_g(\theta) - B_g(\pi-\theta) = 0 \tag{C.66}$$

Recall equation C.33 from the sinusoidal analysis. This equation is also relevant here;

$$\frac{p}{RL_R}\frac{d\Phi_q}{d\theta} - B_g(\pi - \theta) + B_g(\theta) = 0 \tag{C.67}$$

Using equations C.66 and C.67, expressions for $B_g(\theta)$ and $B_g(\pi - \theta)$ are obtained by firstly adding the two together and then subtracting one from the other. These results are;

$$B_g(\theta) = -\frac{1}{2}\left[\frac{p}{RL_R}\frac{d\Phi_q}{d\theta} - \frac{\mu_o R J_d}{p g_e}(\pi - \theta_p)\right] \tag{C.68}$$

$$B_g(\theta) = \frac{1}{2}\left[\frac{p}{RL_R}\frac{d\Phi_q}{d\theta} + \frac{\mu_o R J_d}{p g_e}(\pi - \theta_p)\right] \tag{C.69}$$

If at $\theta = 0$ it is assumed that $B_g(\theta) = B_g(\pi - \theta)$ if $J_d = 0$, then differentiating equation C.62 and letting $\theta = 0$ leads to;

$$\Phi_q' = \gamma A - \gamma B \tag{C.70}$$

This result is substituted in equations C.68 and C.69 to obtain;

$$\begin{aligned} B_g(\theta) &= -\frac{1}{2}\left[\frac{p}{RL_R}(\gamma A - \gamma B)\right] \\ B_g(\pi - \theta) &= \frac{1}{2}\left[\frac{p}{RL_R}(\gamma A - \gamma B)\right] \end{aligned} \tag{C.71}$$

If the initial conditions are applied, then the following expression is formed;

$$\frac{p}{RL_R}(\gamma A - \gamma B) = 0 \tag{C.72}$$

Equation C.72 is true if and only if $A = B$. Thus the solution, equation C.62, becomes;

$$\Phi_q(\theta) = A\left(e^{\gamma\theta} + e^{-\gamma\theta}\right) + \frac{2cJ_q}{b} \tag{C.73}$$

Just as for the sinusoidal case, there are 2 cases to solve in order to determine the expression for A.

Neglecting Pole Side Flux

Based on the boundary conditions of $\Phi_q = 0$ at $\theta = \frac{\theta_p}{2}$,

$$A\left(e^{\gamma\frac{\theta_p}{2}} + e^{-\gamma\frac{\theta_p}{2}}\right) + \frac{2cJ_q}{b} = 0 \tag{C.74}$$

Solving for A;

$$A = \frac{-2cJ_q}{b\left(e^{\gamma\frac{\theta_p}{2}} + e^{-\gamma\frac{\theta_p}{2}}\right)} \tag{C.75}$$

Including Pole Side Flux

This is the case when it is assumed that not all the flux is contained wholly within the extremes of the pole face. Figure 3.11 is still valid and is the basis for the modelling used. Just as for the sinusoidal case, equation C.44 is still valid. For the rectangular current distribution, however, the total MMF enclosed by the loop described in this figure is given by $\frac{J_q R\theta_p}{p}$. Thus the expression to be dealt with is;

$$\frac{J_q R\theta_p}{p} = \int_{-\frac{\theta_p}{2}}^{\frac{\theta_p}{2}} \Phi_q \Re_q R\frac{d\theta}{p} + 2\Phi_q\left(\frac{\theta_p}{2}\right)\Re_{side} \tag{C.76}$$

There is already an expression for Φ_q. This is now substituted into equation C.76.

$$\frac{J_q R\theta_p}{p} = \int_{-\frac{\theta_p}{2}}^{\frac{\theta_p}{2}} \left[A\left(e^{\gamma\theta} + e^{-\gamma\theta}\right) + \frac{2cJ_q}{b}\right]\Re_q R\frac{d\theta}{p} + 2\Phi_q(\frac{\theta_p}{2})\Re_{side} \tag{C.77}$$

$$J_q R\theta_p = \Re_q R \left[\frac{A}{\gamma}\left(e^{\gamma\theta} - e^{-\gamma\theta}\right) + \frac{2cJ_q\theta}{b}\right]_{-\frac{\theta_p}{2}}^{\frac{\theta_p}{2}} + 2p\left[A\left(e^{\gamma\frac{\theta_p}{2}} + e^{-\gamma\frac{\theta_p}{2}}\right) + \frac{2cJ_q}{b}\right]\Re_{side} \tag{C.78}$$

$$J_q R\theta_p = \Re_q R \left[\frac{A}{\gamma}\left(e^{\gamma\frac{\theta_p}{2}} - e^{-\gamma\frac{\theta_p}{2}}\right) + \frac{cJ_q\theta_p}{b} - \frac{A}{\gamma}\left(e^{-\gamma\frac{\theta_p}{2}} - e^{\gamma\frac{\theta_p}{2}}\right) + \frac{cJ_q\theta_p}{b}\right] + 2Ap\Re_{side}(e^{\gamma\frac{\theta_p}{2}} + e^{-\gamma\frac{\theta_p}{2}}) + \frac{4pcJ_q\Re_{side}}{b} \tag{C.79}$$

$$J_q R\theta_p = 2A\left[\frac{\Re_q R}{\gamma}\left(e^{\gamma\frac{\theta_p}{2}} - e^{-\gamma\frac{\theta_p}{2}}\right) + p\Re_{side}\left(e^{\gamma\frac{\theta_p}{2}} + e^{-\gamma\frac{\theta_p}{2}}\right)\right] + \frac{2cJ_q}{b}\left[\Re_q R\theta_p + 2p\Re_{side}\right] \tag{C.80}$$

Finally, an expression for A can be obtained;

$$A = \frac{\gamma}{2b}\frac{bJ_q R\theta_p - 2cJ_q(\Re_q R\theta_p + 2p\Re_{side})}{\Re_q R\left(e^{\gamma\frac{\theta_p}{2}} - e^{-\gamma\frac{\theta_p}{2}}\right) + p\gamma\Re_{side}\left(e^{\gamma\frac{\theta_p}{2}} + e^{-\gamma\frac{\theta_p}{2}}\right)} \tag{C.81}$$

As an aside, if in equation C.81, $\Re_{side} \to \infty$, the the expression for A reverts to the value previously calculated, equation C.75.

The reader should return to Section 3.8 in Chapter 3.

Appendix D

Space Vector Generator

D.1 Introduction

Space vector generation is the process of selecting the required inverter switching state to generate the required voltages and currents to control the torque of the machine. This process is dependent upon inverter and motor ratings, rotor position and values of motor current.

This Appendix presents the mathematics associated with the main control algorithm. The notion of vector selection is also explained.

D.2 Reference Frames

Vector control involves the control of components of the motor currents, represented by a vector, in a rotating reference frame d, q aligned with the rotor flux. In order to "visualise" motor variables with this frame of reference, the 3 phase stator quantities must be translated into their equivalent d, q counterparts and vice versa. This is achieved by the use of the Clarke and Park transforms (Fitzgerald and Kingsley., 1961).

The Clarke transform uses the three phase currents, i_a, i_b and i_c to calculate currents in the two phase orthogonal stator axis. These two currents in the fixed stator phase are then transformed to the i_d and i_q current components in the d, q frame with the Park transform. Figure D.1 illustrates the relationship between variables.

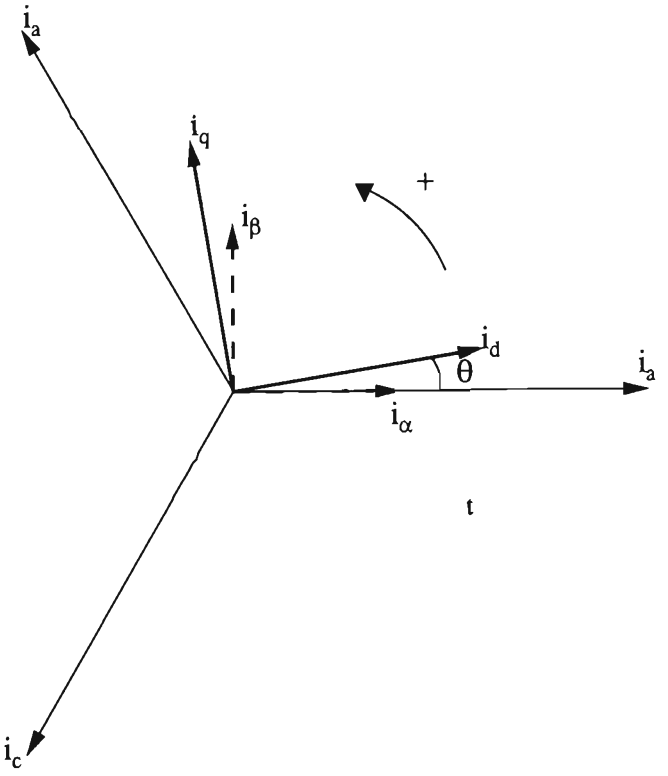

Figure D.1: Reference Frame Relationships

The relationship between the different reference frames can be explained by several mathematical expressions. Using Kirchhoff's current law, Equation D.1 can be written.

$$i_a + i_b + i_c = 0 \tag{D.1}$$

Equation D.1 tells us that once two of the phase currents are known, the third can be calculated. The Clarke transform is given by Equation D.2.

$$\begin{aligned} i_\alpha &= 1.5 i_a \\ i_\beta &= \frac{\sqrt{3}}{2}(i_a + 2 i_b) \end{aligned} \tag{D.2}$$

The transformation into the d, q reference frame is then achieved by the Park transform, Equation D.3.

$$\begin{aligned} i_d &= i_\alpha \cos(\theta) + i_\beta \sin(\theta) \\ i_q &= -i_\alpha \sin(\theta) + i_\beta \cos(\theta) \end{aligned} \tag{D.3}$$

The inverse transforms also exist. In order to transform from the d, q frame to the two phase α, β representation, Equation D.4 is used.

$$\begin{aligned} i_\alpha &= i_d \cos(\theta) - i_q \sin(\theta) \\ i_\beta &= i_d \sin(\theta) + i_q \cos(\theta) \end{aligned} \tag{D.4}$$

D.3 Vector Control

With the notion of different reference frames explained, it is now possible to give a little more detail about how the main control algorithm works. The following sections illustrate the vector control structure of the control algorithms.

1. Convert the phase currents (i_a, i_b and i_c) into their two phase equivalents using Equation D.2.

2. Convert the two phase equivalent into the d and q frame of reference using Equation D.3.

3. Calculate the required change in i_d and i_q to regulate the speed of the motor. The i_d current setpoint is fixed, the output of the speed regulator

is a torque setpoint. The torque setpoint is converted to an i_q value based on the torque equation for the synchronous reluctance motor.

The required change in i_d and i_q is brought about by changing the state of the inverter.

4. Calculate the two phase equivalent of the voltages required to bring about this change in i_d and i_q.

5. Select the appropriate inverter state to affect these voltages.

In order to perform the last step, some further background theory is required. Consider Figure D.2.

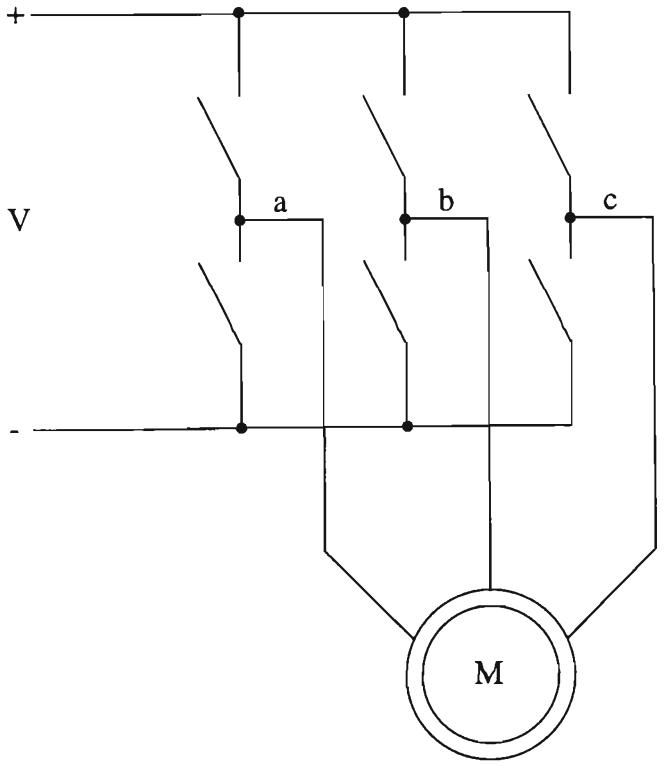

Figure D.2: Three Phase Inverter

The switch elements in each of the three passes of the inverter legs represent the IGBT's of the inverter. Both of the switches in the same leg are controlled by a single signal with appropriate timing logic to prevent "shoot-through".

The signal is defined such that a logic "1" turns the top switch on and a logic "0" turns the bottom one on. With this logic, consider Table D.3.

Vector	a	b	c	V_{ab}	V_{bc}	V_{ca}	V_α	V_β
0	0	0	0	0	0	0	0	0
1	0	0	1	0	$-V$	V	$-\frac{1}{2}V$	$-\frac{\sqrt{3}}{2}V$
2	0	1	0	$-V$	V	0	$-\frac{1}{2}V$	$\frac{\sqrt{3}}{2}V$
3	0	1	1	$-V$	0	V	$-V$	0
4	1	0	0	V	0	$-V$	V	0
5	1	0	1	V	$-V$	0	$\frac{1}{2}V$	$-\frac{\sqrt{3}}{2}V$
6	1	1	0	0	V	$-V$	$\frac{1}{2}V$	$\frac{\sqrt{3}}{2}V$
7	1	1	1	0	0	0	0	0

Table D.1: Inverter States and Voltages

This table represents the different voltages that are applied to the winding of the motor for different voltage vector selections.Figure D.3 is a graphical representation of these states.

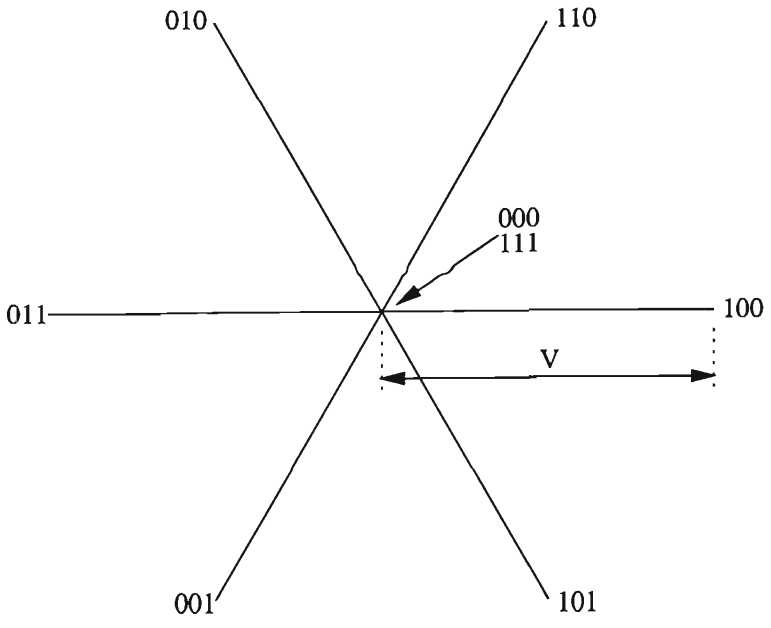

Figure D.3: Inverter Voltage Vectors on Voltage Phasor Plane

The control algorithm produces a value for i_α and i_β. These two values can be used to calculate a vector, with magnitude and angle, that lies somewhere on the voltage phasor plane. Consider Figure D.4.

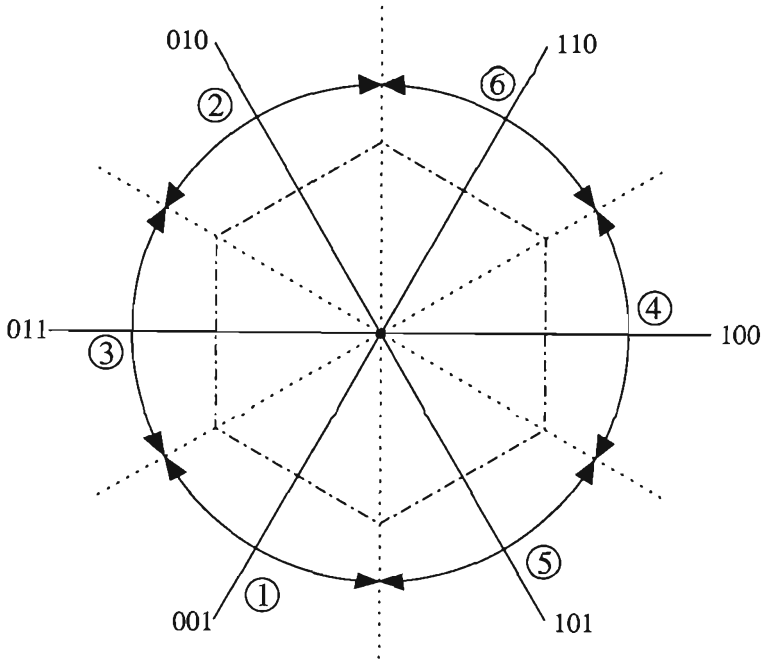

Figure D.4: Inverter Voltage Vectors on Voltage Phasor Plane

If the vector lies inside the hexagonal are, then the zero voltage vector is selected. If the vector lies outside of this hexagon, then depending upon which region it lies in, that region's vector is selected. There are six regions, labelled ① to ⑥. If the required voltage vector was placed outside the hexagon and in region ⑥, for example, then vector six would be applied to the motor during the next control interval.

Appendix E

Experimental Machine Detail

E.1 Introduction

The design of the 22 kW synchronous reluctance motor was never going to be part of this thesis. It was designed and manufactured by the now defunct Energy Efficient Research Centre at the University of Wollongong. The paper written about the testing of this motor, (Platt et al., 1993), should be read for a more complete understand of the abilities of this drive. Its use in this project has been the verification of the sensorless position estimation algorithms.

The complete design of the machine is far too complex to include in this thesis. However, the following drawing is included that the reader may gain some insight into the design of the machine.

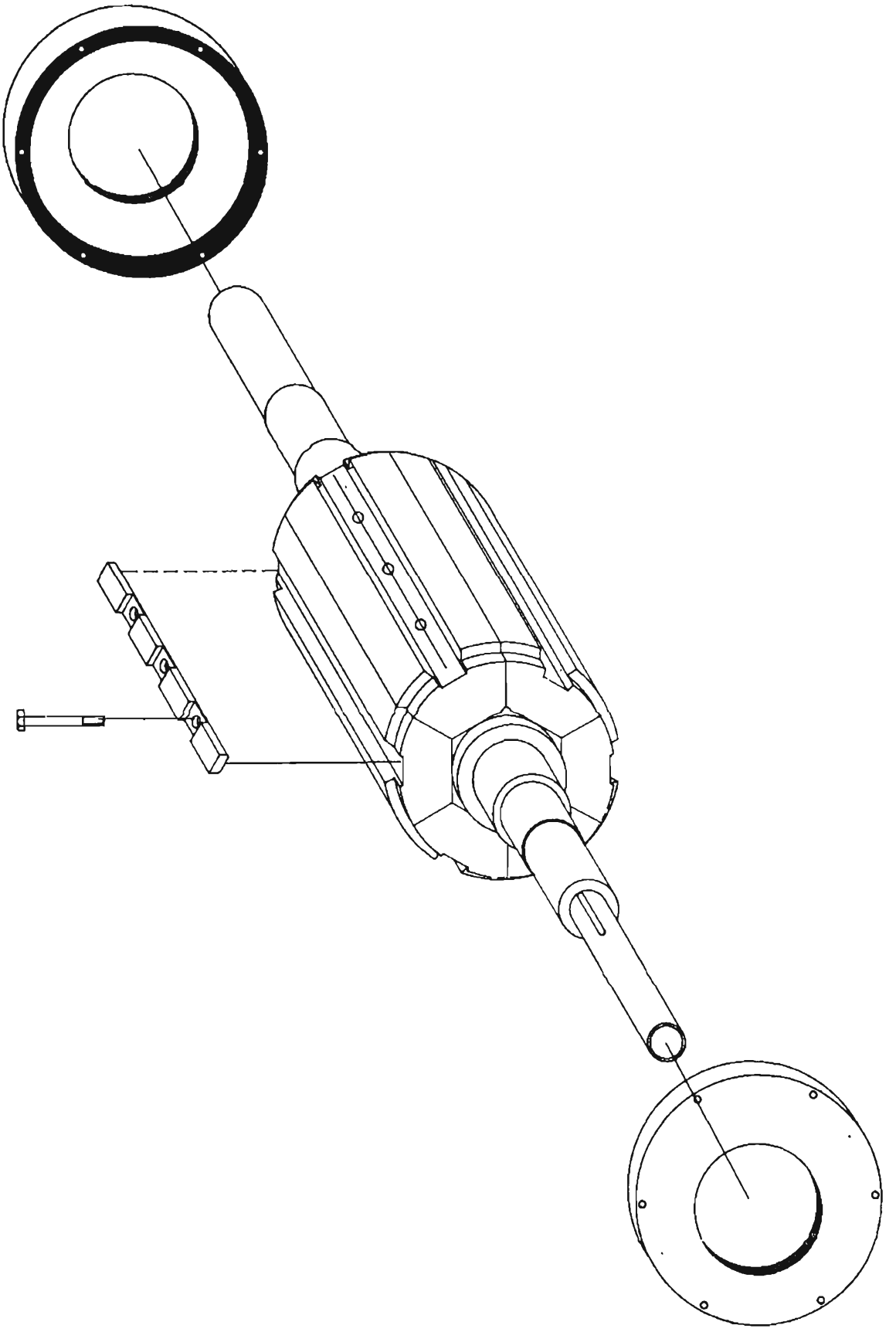

Figure E.1: SyncRM Rotor Expanded View

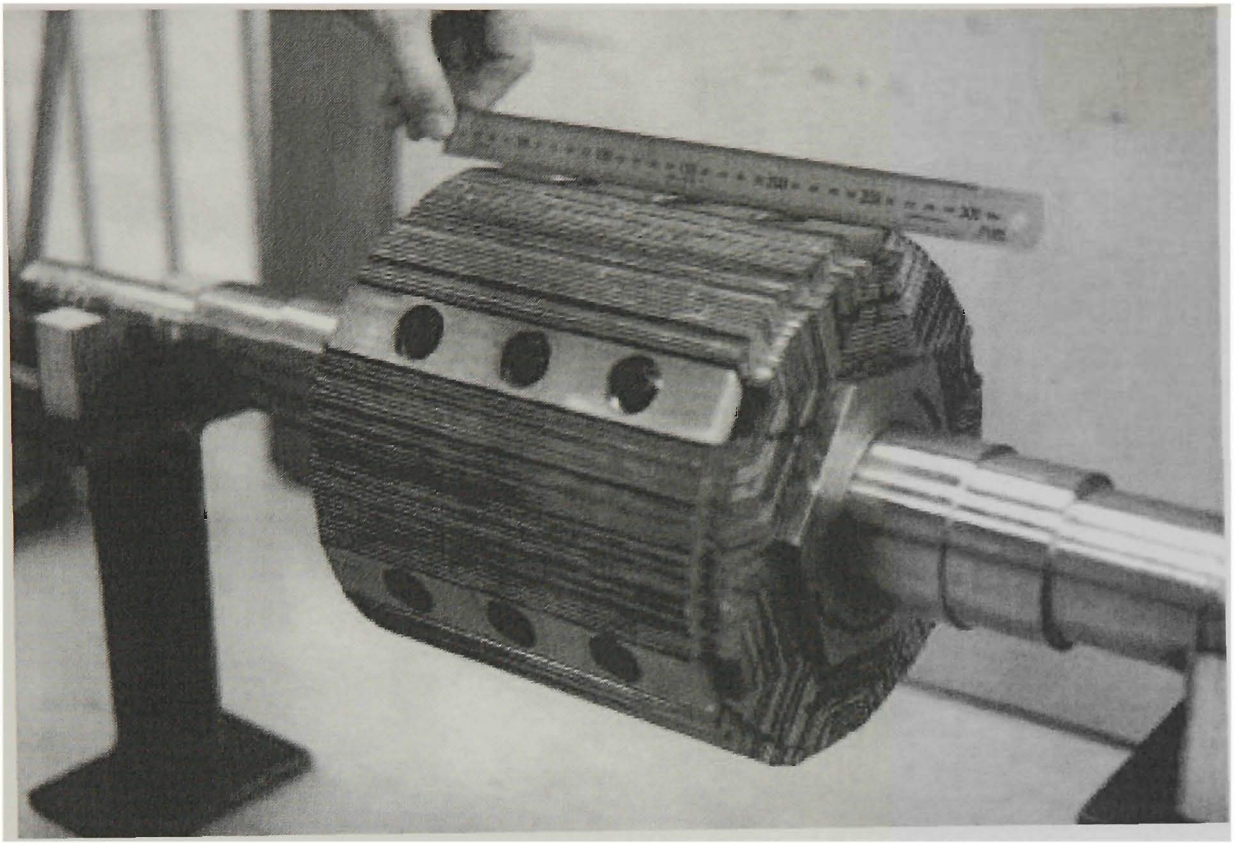

Figure E.2: 22 kW ALA SyncRM Rotor

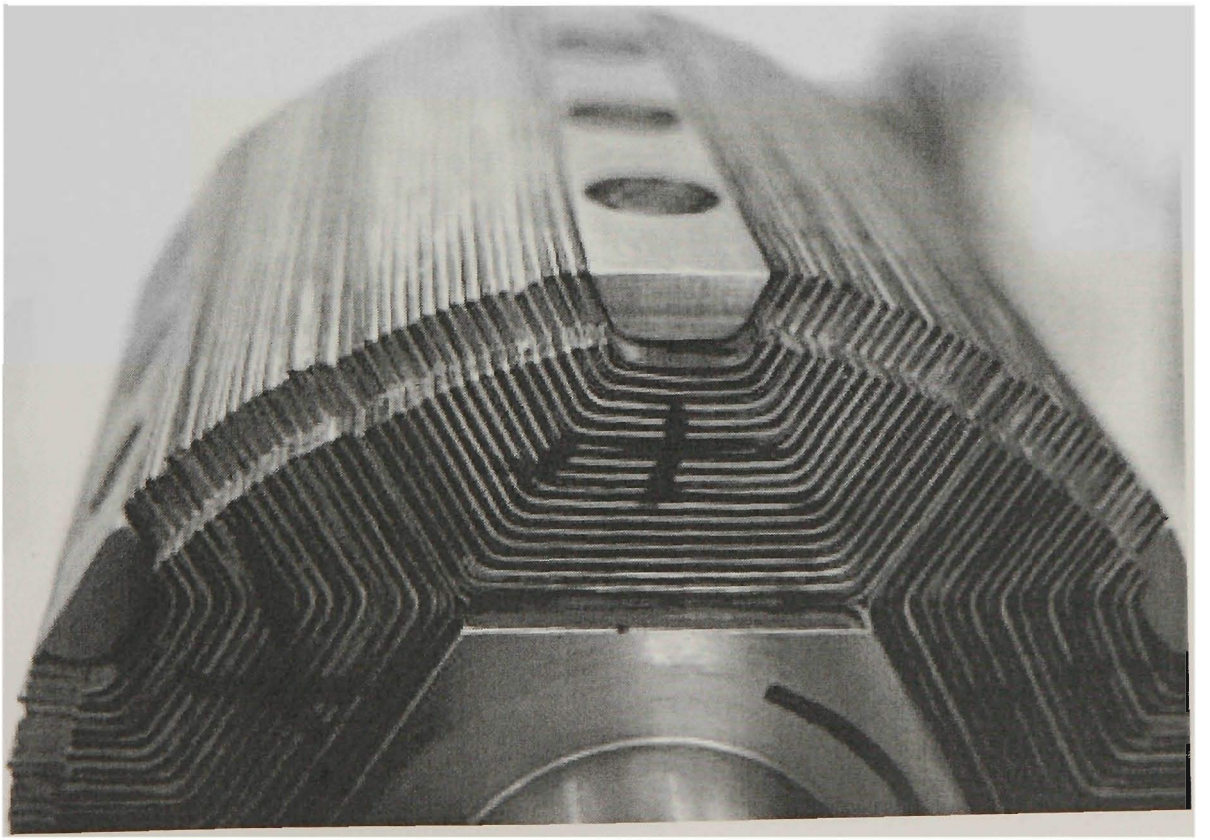

Figure E.3: 22 kW ALA SyncRM Rotor Lamination Details

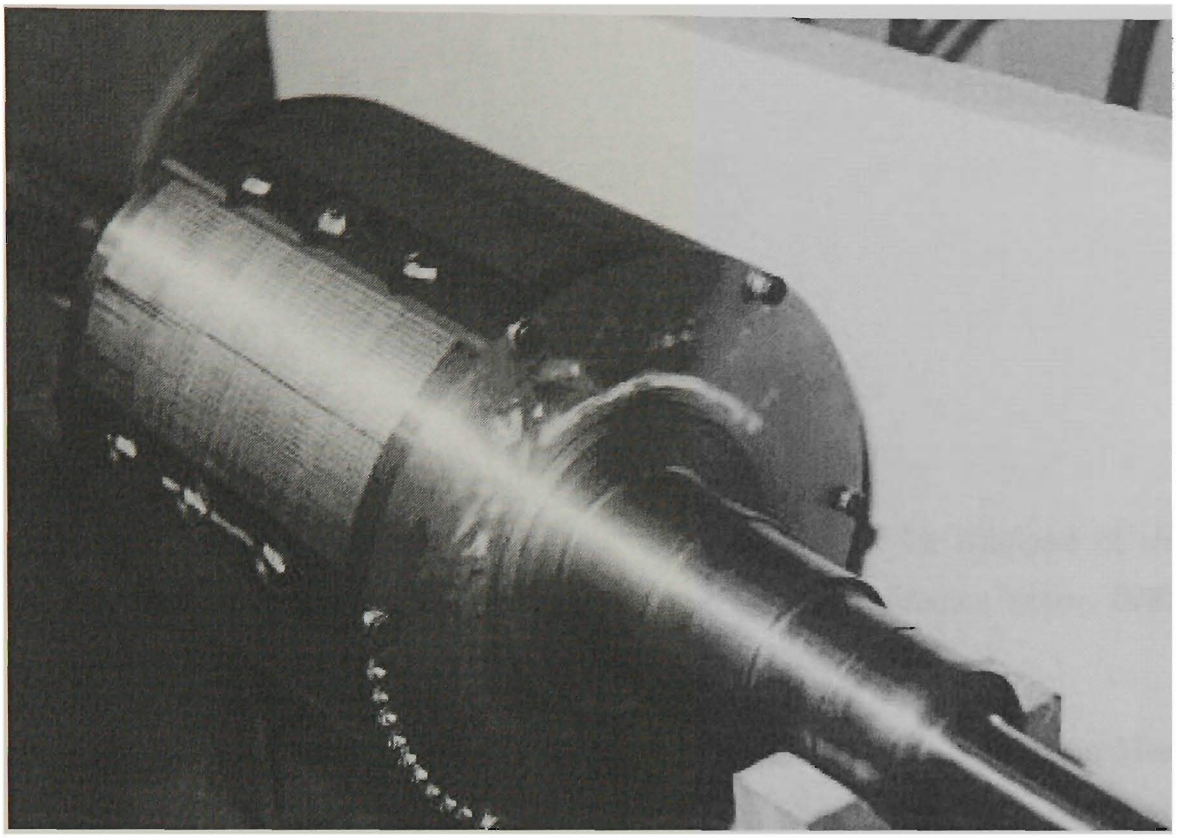

Figure E.4: 22 kW ALA SyncRM Finished Rotor

Bibliography

Arefeen, M. S., Ehsani, M., and Lipo, T. A. (1994a). An Analysis of the Accuracy of Indirect Shaft Sensor for Synchronous Reluctance Motor. *IEEE Transactions on Industry Applications*, 30(5):1202–1208.

Arefeen, M. S., Ehsani, M., and Lipo, T. A. (1994b). Sensorless Position Measurement in Synchronous Reluctance Motor. *IEEE Transactions on Power Electronics*, 9(6):624–630.

Baldor (1993). *Baldor Installation and Service Manual, Control Model 91X-XXX-24XX*. Baldor.

Betz, R. E. (1991). Control of Synchronous Reluctance Machines. In *Proceedings of the IEEE Industry Applications Society Annual Meeting*, pages 456–463.

Boldea, I., Fu, Z. X., and Nasar, S. A. (1991). Torque Vector Control (TVC) of Axially–Laminated Anisotropic (ALA) Rotor Reluctance Synchronous Motors. *Electric Machines and Power Systems*, 19:381–398.

Boldea, I., Fu, Z. X., and Nasar, S. A. (1994). Performance Evaluation of Axially-Laminated Anisotropic (ALA) Rotor Reluctance Synchronous Motors. *IEEE Transaction on Industry Applications*, 30(4):533–554.

Boldea, I. and Nasar, S. A. (1991). Emerging Electric Machines with Axially Laminated Anisotropic Rotors : A Review. *Electric Machines and Power Systems*, 19:673–703.

Bowman, R. and Platt, D. (1993). Estimation of Rotor Position from Terminal Measurements for a Stationary Reluctance Motor. In *Proceedings of the Australian Universities Power Engineering Conference*, pages 45–49.

Brown, R. H., Schneider, S. C., and Mulligan, M. G. (1992). Analysis of Algorithms for Velocity Estimation from Discrete Position Versus Time Data. *IEEE Transactions on Industrial Electronics*, 39(1):11–19.

Ciufo, P. P. and Platt, D. (1996). Sensorless Rotor Position Estimation in a Synchronous Reluctance Motor. In *Proceedings of the Australian Universities Power Engineering Conference*, volume 1, pages 37–42.

Ciufo, P. P., Platt, D., and Perera, B. S. P. (1994). Magnetic Circuit Modelling of a Synchronous Reluctance Motor. In *Proceedings of the Australian Universities Power Engineering Conference*, pages 37–42.

Ciufo, P. P., Platt, D., and Perera, B. S. P. (1999). Magnetic Circuit of a Synchronous Reluctance Motor. *Electric Machines and Power Systems*, 27(3):253–270.

Coates, C. E., Platt, D., and Perera, B. S. P. (1997). Design Optimisation of an Axially Laminated Synchronous Reluctance Motor. In *Proceedings of the IEEE Industry Applications Society Annual Meeting*, pages 279–285.

Consoli, A., Russo, F., Scarcella, G., and Testa, A. (1998). Low- and Zero-Speed Sensorless Control of Synchronous Reluctance Motor Drives. In *Proceedings of the IEEE Industry Applications Society Annual Meeting*, pages 685–692.

Consoli, A., Russo, F., Scarcella, G., and Testa, A. (1999). Low- and Zero-Speed Sensorless Control of Synchronous Reluctance Motor Drives. *IEEE Transactions on Industry Applications*, 35(5):1050–1057.

Cruickshank, A. J. O., Anderson, A. F., and Menzies, R. W. (1966). Axially Laminated Anisotropic Rotors for Reluctance Motors. *Proceedings of the IEE*, 113(12):2058–2060.

Cruickshank, A. J. O., Anderson, A. F., and Menzies, R. W. (1971). Theory and Performance of Reluctance Motors with Axially Laminated Anisotropic Rotors. *Proceedings of the IEE*, 118(7):887–894.

Degner, M. W. and Lorenz, R. D. (1998). Using Multiple Saliencies for the Estimation of Flux, Position, and Velocity in AC Machines. *IEEE Transactions on Industry Applications*, 34(5):1097–1104.

Draper, A. (1967). *Electrical Machines.* Longmans Green and Co Ltd, second edition.

Fitzgerald, A. E. and Kingsley., C. (1961). *Electric Machinery, The Dynamics and Statics of Electromechanical Energy Conversion.* McGraw-Hill Book Company Inc.

Fletcher, J. E., Green, T. C., and Williams, B. W. (1994). Vector Control of a Synchronous Reluctance Motor Utilising an Axially Laminated Rotor. In *IEE Conference Proceedings Power Electronics and Variable-Speed Drives*, pages 18–23.

Fratta, A., Troglia, G. P., Vagati, A., and Villata, F. (1993). Evaluation of Torque Ripple in High Performance Synchronous Reluctance Machines. In *Proceedings of the IEEE Industry Applications Society Annual Meeting*, volume 1, pages 163–170.

Fratta, A., Vagati, A., and Villata, F. (1992). On the Evolution of AC Machines for Spindle Drive Applications. *IEEE Transactions on Industry Applications*, 28(5):1081–1086.

Ha, J.-I., Kang, S.-J., and Sul, S.-K. (1999). Position-Controlled Synchronous Reluctance Motor Without Rotational Transducer. *IEEE Transactions on Industry Applications*, 35(6):1393–1398.

Honsinger, V. B. (1971a). The Inductances L_d and L_q of Reluctance Machines. *IEEE Transactions on Power Applications and Systems*, PAS-90(1):298–304.

Honsinger, V. B. (1971b). Steady State Performance of Reluctance Machines. *IEEE Transactions on Power Applications and Systems*, PAS-90(1):305–317.

Innovative-Integration (1996). *ADC64 Hardware Manual.* Innovative Integration.

Jansen, P. L. and Lorenz, R. D. (1995). Transducerless Position and Velocity Estimation in Induction and Salient AC Machines. *IEEE Transactions on Industry Applications*, 31(2):240–247.

Jovanovic, M., Betz, R. E., and Platt, D. (1995). Position and Speed Estimation of Sensorless Synchronous Reluctance Motor. In *Proceedings of the IEEE International Conference on Power Electronics and Drive Systems*, pages 844–849.

Jovanovic, M., Betz, R. E., and Platt, D. (1998). Sensorless Vector Controller for a Synchronous Reluctance Motor. *IEEE Transactions on Industry Applications*, 34(2):346–354.

Kang, S., Ha, J., and Sul, S. (1998). Position Controlled Synchronous Reluctance Motor Without Rotational Transducer. In *Proceedings of the IEEE Industry Applications Society Annual Meeting*, pages 671–676.

Kostko, J. K. (1923). Polyphase Reaction Synchronous Motors. *Journal of the American Institute of Electrical Engineers*, 42:1162–1168.

Kreindler, L., Testa, A., and Lipo, T. A. (1993). Position Sensorless Synchronous Reluctance Motor Drive using the Stator Phase Voltage Third Harmonic. In *Proceedings of the IEEE Industry Applications Society Annual Meeting*, pages 679–686.

Lagerquist, R., Boldea, I., and Miller, T. J. E. (1994). Sensorless Control of the Synchronous Reluctance Motor. *IEEE Transactions on Industry Applications*, 30(3):673–681.

Law, J. D., Chertok, A., and Lipo, T. A. (1994). Design and Performance of Field Regulated Reluctance Machine. *IEEE Transactions on Industry Applications*, 30(5):1185–1191.

Lawrenson, P. J. and Agu, L. A. (1964a). Low-Inertia Reluctance Machines. *Proceedings of the IEE*, 111(12‘):2017–2025.

Lawrenson, P. J. and Agu, L. A. (1964b). Theory and Performance of Polyphase Reluctance Machines. *Proceedings of the IEE*, 111(8):1435–1445.

Lin, M.-T. and Liu, T.-H. (2000). Sensorless Synchronous Reluctance Drive With Standstill Starting. *IEEE transactions on Aerospace and Electronic Systems*, 36(4):1232–1240.

Lipo, T. A. (1991). Synchronous Reluctance Machines - A Viable Alternative for AC Drives ? *Electric Machines and Power Systems*, 19:659–671.

Lorenz, R. D. and Patten, K. W. V. (1991). High-Resolution Velocity Estimation for All-Digital, ac Servo Drives. *IEEE Transaction on Industry Applications*, 4(27):701–705.

Luo, X., El-Antably, A., and Lipo, T. A. (1994). Multiple Coupled Circuit Modelling of Synchronous Reluctance Machines. In *Proceedings of the IEEE Industry Applications Society Annual Meeting*, volume 1, pages 281–289.

Marongiu, I. and Vagati, A. (1991). Improved Modelling of a Distributed Anisotropy Synchronous Reluctance Machine. In *Proceedings of the IEEE Industry Applications Society Annual Meeting*, pages 238–243.

Matsuo, T. and Lipo, T. A. (1994a). Rotor Design Optimisation of Synchronous Reluctance Machine. *Transactions on Energy Conversion*, 9(2):359–365.

Matsuo, T. and Lipo, T. A. (1994b). Rotor Position Detection Scheme for Synchronous Reluctance Motor Based on Current Measurements. In *Proceedings of the IEEE Industry Applications Society Annual Meeting*, pages 627–634.

Miller, T. J. E., Hutton, A., Cossar, C., and Staton, D. A. (1991). Design of a Synchronous Reluctance Motor Drive. *IEEE Transactions on Industry Applications*, 27(4):873–879.

Platt, D. (1992). Reluctance Motor with Strong Rotor Anisotropy. *IEEE Transactions on Industry Applications*, 28(3):652–658.

Platt, D., Sanders, G., and Kulkarni, S. (1993). Testing of a Synchronous Reluctance Motor in a 22kW Frame. In *Proceedings of the Australian Universities Power Engineering Conference*, pages 45–49.

Saito, K., Kamiyama, K., Ohmae, T., and Matsuda, T. (1988). A Microprocessor-Controlled Speed Regulator with Instantaneous Speed Estimation for Motor Drives. *IEEE Transaction on Industrial Electronics*, 35(1):95–99.

Schroedl, M. and Weinmeier, P. (1994). Sensorless Control of Synchronous Reluctance Machines at Arbitrary Operating Conditions Including Standstill. *IEEE Transaction on Power Electronics*, 9(2):225–231.

Slemon, G. R. and Straughen, A. (1980). *Electric Machines*. Addison-Wesley Publishing Company.

Soong, W. L., Staton, D. A., and Miller, T. J. E. (1993). Validation of Lumped-Circuit and Finite-Element Modelling of Axially Laminated Brushless Motors. In *IEE Conference Proceedings Electrical Machines and Drives*, pages 85–90.

Soong, W. L., Staton, D. A., and Miller, T. J. E. (1995). Design of a New Axially-Laminated Interior Permanent Magnet Motor. *IEEE Transactions on Industry Applications*, 31(2):358–367.

Staton, D. A., Miller, T. J. E., and Wood, S. E. (1993). Maximising the Saliency Ratio of the Synchronous Reluctance Motor. *IEE Proceedings Part B*, 140(4):249–259.

Staton, D. A., Soong, W. L., and Miller, T. J. E. (1995). Unified Theory of Torque Production in Switched Reluctance and Synchronous Reluctance Motors. *IEEE Transactions on Industry Applications*, 31(2):329–336.

Uezato, K., Senjyu, T., and Tomori, Y. (1994). Modelling and Vector Control of Synchronous Reluctance Motors Including Stator Iron Loss. *IEEE Transactions on Industry Applications*, 30(4):971–976.

Xiang, Y. Q. and Nasar, S. A. (1995). Estimation of Rotor Position and Speed of a Synchronous Reluctance Motor for Servodrives. *IEE Proceedings Electric Power Applications*, 142(3):201–205.